Alma Mater Studiorum
Università di Bologna

SCHOOL OF ENGINEERING
Second Cylce Degree in Telecommunications Engineering

CAMERA BASED LOCALIZATION FOR INDOOR OPTICAL WIRELESS NETWORKS

Supervisor:
Prof.
TARTARINI GIOVANNI

External Co-Supervisor:
Prof.
TANGDIONGGA
EDUWARD

Defended by:
BOLDRINI LEONARDO

Graduation Session III
Academic Year 2018/2019

Summary

The main focus of this work is to implement device localization in an indoor communication network which employs short range Optical Wireless Communication (OWC) using pencil beams.
OWC is becoming increasingly important as a solution to the shortage of available radio spectrum. Presently, new wireless services must share the same spectrum with existing services, thus, overcrowding the radio spectrum. This leads to interference among wireless devices, poor wireless link performances and unnecessary high wireless power consumption.
In order to counter this problem, a radical new approach is proposed by performing wireless communication using optical rather than radio techniques, by deploying optical pencil beam technologies to provide users with access to an indoor optical fiber infrastructure. An architecture based on free-space optics has been adopted. The narrow infrared beam is considered a good solution because of its ability to optimally carry all the information which the optical fiber can transport, in an energy-efficient way.
Beam Steered - Infrared Light Communication (BS-ILC) brings the light only where is needed. Multiple beams may independently serve user devices within a room, hence each device can get a non-shared capacity without conflicts with other devices.
Infrared light beams, additionally, are allowed to be operated at a higher power than visible light beams, due to a higher eye safety threshold for infrared light. Together with the directivity of a beam, this implies that the received signal-to-noise ratio with BS-ILC can be substantially higher than with Visible Light Communication (VLC), enabling a higher data rate and longer reach at better power efficiency. Current BS-ILC prototypes allow multiple beams with over 100 Gbit/s per beam [1]. This high performance can only be achieved with small footprints, hence the system needs to know the exact location of user devices.

In this thesis, an accurate and fast localization/tracking technique using a low-cost camera and simple image processing is presented. Furthermore, a localization technique is performed with another, slightly more expensive camera. Results are compared, showing a promising potential for camera-based localization.

Contents

List of Figures

Chapter 1

Optical Wireless Communication

With the evolution of technology towards enabling smart devices, smart buildings and smart cities, people, devices and information are becoming more interconnected than ever.
Wireless communication has become a popular communication method for users because of its obvious mobility advantages, and has been evolving very rapidly.
However, it is facing the challenging reality that the number of wireless devices connected to the network is increasing exponentially. This is magnified by the Internet Of Things (IOT) phenomenon, where a variety of wireless devices such as laptops, tablet computers, smart phones and most importantly wireless sensors, etc. are connected to the Internet to serve us with broadband data communications, reliable monitoring of environmental conditions and health status, etc. everywhere, whenever needed.
In the year 2008 the number of devices connected to the internet was already higher than the number of people on earth. However, according to Cisco, the IoT phenomena will be driving an exponential increase in the number of connected devices: the IoT market has grown for some time and is due to reach 31 billion connected devices by 2020 and 75 billion devices by 2025 [2], as shown in 1.1.

The impact of such a huge scale of increase in connected devices is not subtle. Huge transfers of information are happening at a tremendous capacity every day.

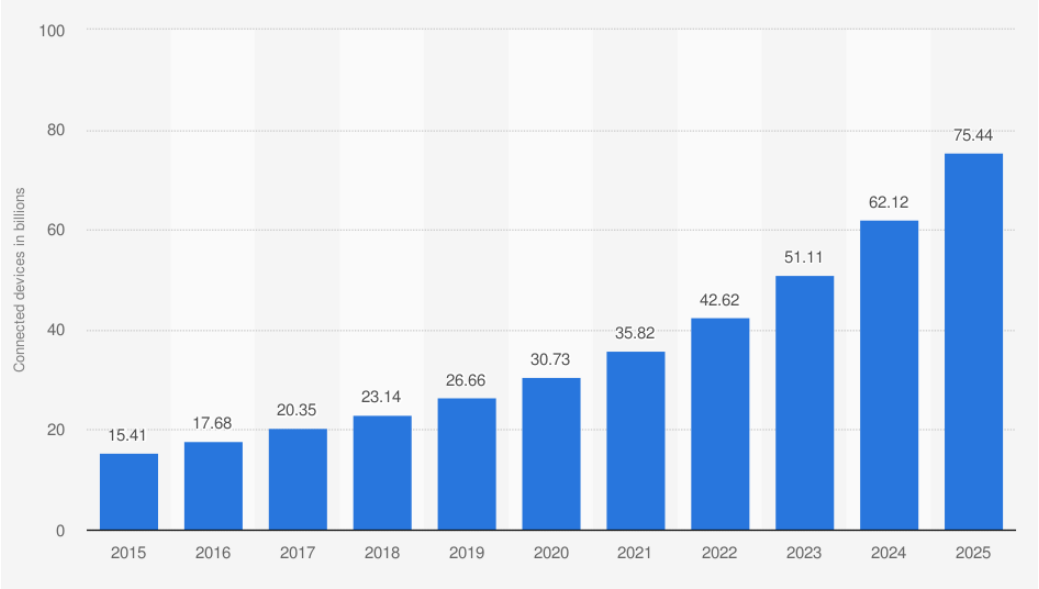

Figure 1.1: Increasing number of connected devices.

In addition, with the increasing amount of consumer products, about 80% of mobile data is generated indoors [3]. Highspeed and on-the-spot communication has been a persistent demand ever since the data over wireless technology was introduced. Subsequently, this has resulted in today's heavy congestion of the Industrial Scientific and Medical (ISM) bands, as shown in Fig. 1.2, which are allocated for unlicensed operation.

According to the Institute of Electrical and Electronics Engineers (IEEE) 802.11ax standard, Wi-Fi 6 promises maximum data rate of 9,6 Gbps, about 37% higher than IEEE 802.11ac. In dense deployments, throughput speeds can be 4 times higher than IEEE 802.11ac, due to a higher efficient use of spectrum, thanks to technologies like Orthogonal Frequency-Division Multiple Access (OFDMA), higher order of modulation 1024-QAM, Multi-User Multiple Input Multiple Output (MU-MIMO), and many others.
However, these speeds are hardly seen in practice as they are offered on a medium shared by multiple users. The Medium Access Control (MAC) protocols partition the speed among multiple users and this requires some overhead to be done properly. Additionally, the IEEE 802.11ad protocol was released in 2012 based on the 60 GHz band and supports a bandwidth of up to 7 GHz (57 to 64 GHz and more) for ultra-high-speed operation within a room.

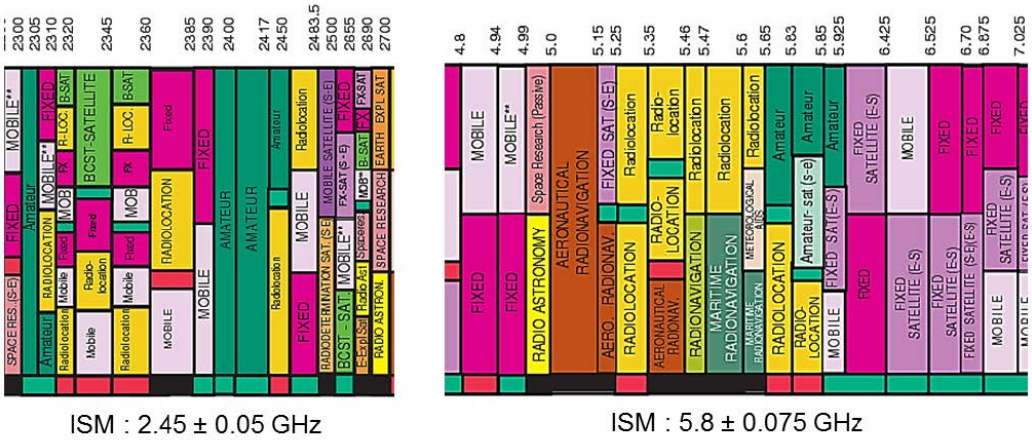

Figure 1.2: Spectrum allocation within the FCC unregulated ISM bands centered at 2.45 GHz and 5.8 GHz. Cropped from [4].

The unregulated 60 GHz ISM band provided by the Federal Communications Commission (FCC) is limited to only 7 GHz of the spectrum [5, 6]. Continuous growth of traffic led by the increase in high bandwidth applications such as Ultra High-Definition Television (UHDTV), high quality video conferencing, 3D videos, online video gaming, peer-to-peer networking, etc. will demand ever more bandwidth.

It is becoming clear that the available radio spectrum is getting exhausted due to bandwidth limitations [7]. Therefore, interference among devices degrades the Quality of Service (QoS), decreases channel throughput, increases wireless power consumption and inevitably results in costly services due to the inability of wireless service providers to provide more capacity.

Counter measures such as the acquisition of underused licensed sub-bands are very costly [8]. Efforts are seen in advocating small cells architectures such as femtocells and picocells in order to support the increase in network capacity for indoor networks [9, 10]. Cellular network operators implement data-offoading from cellular traffc to fixed wireless Local Area Network (LAN) or femtocell networks [11, 12, 13] wherever possible. This is a cost-effective way for mobile operators while at the same time, mobile users also enjoy the higher speed in LAN networks. At the moment, there are still many efforts in trying to squeeze more and more data into the available radio bandwidths at the ISM bands centered at 2.4 GHz, 5 GHz and 60 GHz, to improve spectral efficiency in order to support larger capacity. Inevitably, complex digital

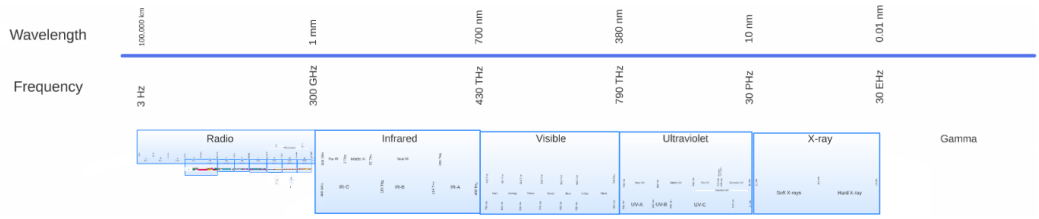

Figure 1.3: Portions of the spectrum, with corresponding wavelengths and frequencies.

signal processing and advanced modulation formats are needed, which will take a toll on the energy consumption of radio communication and result in higher operating cost.
However, the inherent spectrum limit prevents radio wireless bandwidth from approaching the capacity achievable in the optical spectrum, that is, furthermore, unregulated.

In an unlicensed approach, Optical Wireless Communication (OWC) is an area that offers a promising technology in fighting the radio spectrum crisis. The optical spectrum offers bandwidths orders of magnitude higher than that available in the Radio Frequency (RF) spectrum, about 2600 times bigger. OWC solutions are usually proposed in the visible and Infrared (IR) spectrum. The radio spectrum ranges between 3 kHz and 300 GHz while the visible and infrared optical region covers the spectrum from the 200 Terahertz (THz) up to 750 THz.

This very high frequency optical spectrum region literally brings with it a huge amount of bandwidth. In other words, the optical spectrum can easily support high bandwidth channels that can carry ultra-high data rates.
Corresponding to the hundreds of Terahertz frequency band, the wavelengths of the optical spectrum is in the μm range. This very short wavelengths result in a very different wave behavior: optical waves do not penetrate walls. This can be seen, in some cases, as an advantage in terms of security. However, the inability to propagate through opaque surfaces could be a disadvantage due to possible blockage of communication links leading to the risk of a connection drop, which on the other hand, can also be perceived as more secure or sensitive to eavesdropping.
Optical waves are also insensitive to Electromagnetic Interference (EMI) thereby making it ideal for electromagnetic sensitive places such as hospitals and air planes.An important limitation is imposed by regulations on the

transmitted power of the optical beams, that has to be compliant to skin- and eye-safety regulations enforced by the American National Standards Institute (ANSI) Z136 [15] and International Electrotechnical Commission (IEC) 60825 [16] standards for indoor use.

1.1 OWC for indoors

OWC is a form of optical communication in which Ultraviolet (UV), visible and IR light can be used to carry a communication signal [17]. Back in ancient times, the need for communication has been fulfilled by beacon fires and smoke to signal messages from one location to another. Sunlight has been used to signal messages by reflecting the sun using reflective objects. Centuries later, in 1888, Alexander Graham Bell and his assistant, Charles Sumner Tainter, came up with an ingenious invention which is known as the "photophone". It is an apparatus for the production of sounds by means of light [18, 19]. With the advantage of its inability to be intercepted by war enemies, the application of the photophone was mostly limited to military and space communication.

The idea of optical wireless communication became interesting again with the invention of the laser [20], IR Light Emitting Diode (LED) [21, 22], and fiber optics in 1960's. In the 90's, the idea of using ground-to-satellite and satellite-to-ground communication using red and green laser became popular [23]. After year 2000, Free-Space Optics (FSO) technologies gained interests in civil and military applications ranging from standard telecommunication [24, 25] to undersea [26] and inter-satellite or space [27] communication employing wavelengths from 1 up to 10 μm [23, 28]. Besides communication, FSO technologies are also popular in optical metrology for "no-contact" measurement systems [29].

More recently, due to its prominent bandwidth advantage, OWC is seen as an access technology, complementary to radio for high-speed short-range communication links in the and Fifth Generation (5G) networks [3, 30, 31].

Fig. 1.4 shows an overview of the basic types of architectures for indoor optical wireless systems [14, 32]. Each type of architecture, i.e. the direct, the non-direct and the hybrid types, can be implemented using Line-of-Sight (LoS) or Non-Line-Of-Sight (NLoS) methods. In general, the direct architecture provides a point-to-point configuration and requires good alignment while the non-direct architecture enables point-to-multipoint configuration

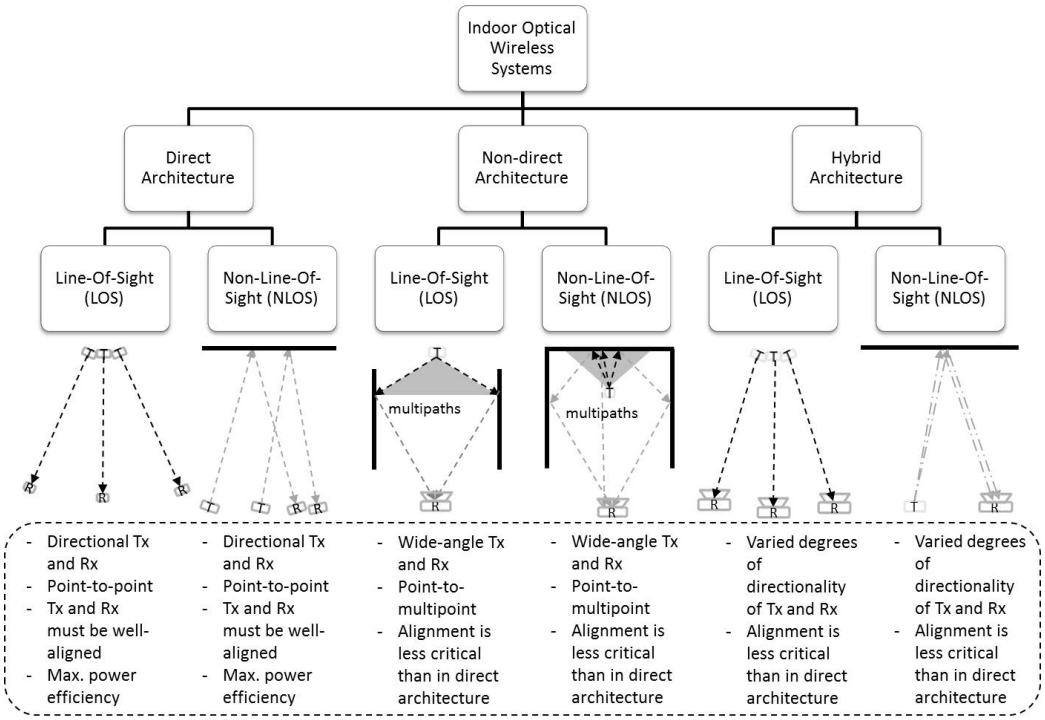

Figure 1.4: Types of indoor optical wireless architectures [14, 32].

and a less critical alignment is needed. The direct architecture is able to provide a higher link power budget in a particular direction, which means that mobility is possible only if both the transmitter and the receiver know their relative positions. Localization and continuous tracking functionalities are necessary to maintain connections in order to provide mobility to users [33, 34, 35, 36]. On the other hand, LoS links are susceptible to severe shadowing or blockage. In hybrid systems, a combination of transmitters and receivers of varying degrees of directionality can be employed.

1.2 Visible and Infrared Light Communication

OWC can be divided in visible and infrared light spectrum: in the visible light spectrum, OWC spans over a range between 400 nm (750 THz)

and 700 nm (430 THz). It is also known as VLC. Typically, LEDs are used as the transmission source. Laser diodes can also be used, but they are normally deployed with a diffuser for eye-safety reasons. White LEDs are now a popular source of lighting as an alternative to tungsten and fluorescent lamps due to their long lifetime and low power consumption. LEDs nowadays have competitive efficacy (lumen/Watt), cost (lumen/dollar) and lifetime. Thus, LED lighting platforms are considered interesting for communication purposes [39, 40, 41]. White LEDs are commonly constructed using two combinations. The first is a combination of a blue LED with phosphor and the other is a combination of red, blue and green LEDs. The blue LED chip typically has a -3 dB frequency response of approximately 15-20 MHz while its performance can be limited by the phosphor layer which has a -3 dB bandwidth of approximately 2 MHz. The tricolor RGB white LED has a frequency response of approximately 10-20 MHz for each LED chip. The limited bandwidth is due to the carrier recombination lifetime in the semiconductor material of the LED. These LEDs can only support communication with speeds of Mbps. However, the current μLED and RC-LED, have a bandwidth of approximately 100 MHz. In terms of backbone network infrastructure, LED lighting can be integrated with the Universal Serial Bus (USB), Power over Ethernet (PoE) or Power Line Carrier (PLC) technologies depending on the distances needed.
They can provide power and data on the same medium and transport them to the lamps. In 2015, Y. Wang et al. have proposed a Single Mode Fiber (SMF) based network architecture for VLC using OFDM modulation format with a total bi-directional throughput of 8 Gbps at a BER of $< 3.8 \times 10^{-3}$, over 65 cm free space propagation distance [42].
Recently, the term Light Fidelity (LiFi) is introduced to describe a complete VLC networking system [43, 44]. Early VLC standardization in the IEEE 802.15.7, which focused on point-to-point communication and dimming support, is being revised to include LiFi, which supports bi-directional multiuser communication and user mobility [45, 46].

On the other hand, OWC operating in the infrared spectrum is commonly centered at 850 nm (353 THz), 1310 nm (229 THz) and 1550 nm (193 THz), in a Point-to-Point (PtP) configuration, and is widely known as IR FSO communication. As typically IR lasers are employed, the source has a narrow beam compared to an LED, thus, a very high bandwidth transmission can be achieved. For this reason, the bandwidth of the system is usually only

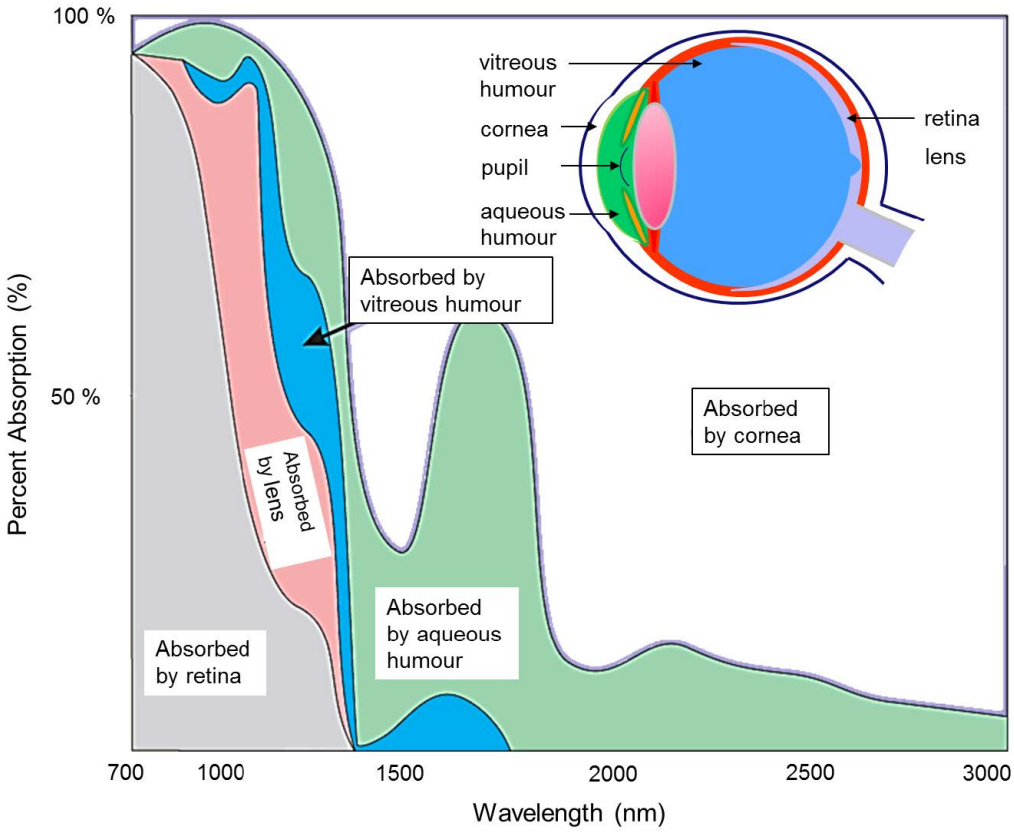

Figure 1.5: Absorption of infrared radiation by various ocular structures as a function of wavelength [47]. An eye model is provided at the top right as a reference to the corresponding absorption layers of the eye.

limited by practical implementation constraints such as eye-safety compliant power, transceiver bandwidth, filter and photoreceiver bandwidths, and switching and modulation speeds.

Because IR radiation is non-visible, it is subjected to eye-safety regulations by the IEC 60825 [16] and ANSI Z136 [15]. In fact, the eye-safety limits are related to the absorption of light at different wavelengths in the eye (see Fig. 1.5). The cornea and the lens absorb a small but significant amount of near-IR wavelengths of 780 nm to 1400 nm [47]. A small amount is absorbed by the aqueous and vitreous humours, while the remaining goes to the retina. Wavelengths $>$ 1400 nm are largely absorbed in the cornea, followed by the aqueous and a small amount in the vitreous humours, thus, preventing its reach to the retina. As a result, the threshold damage is higher in the IR

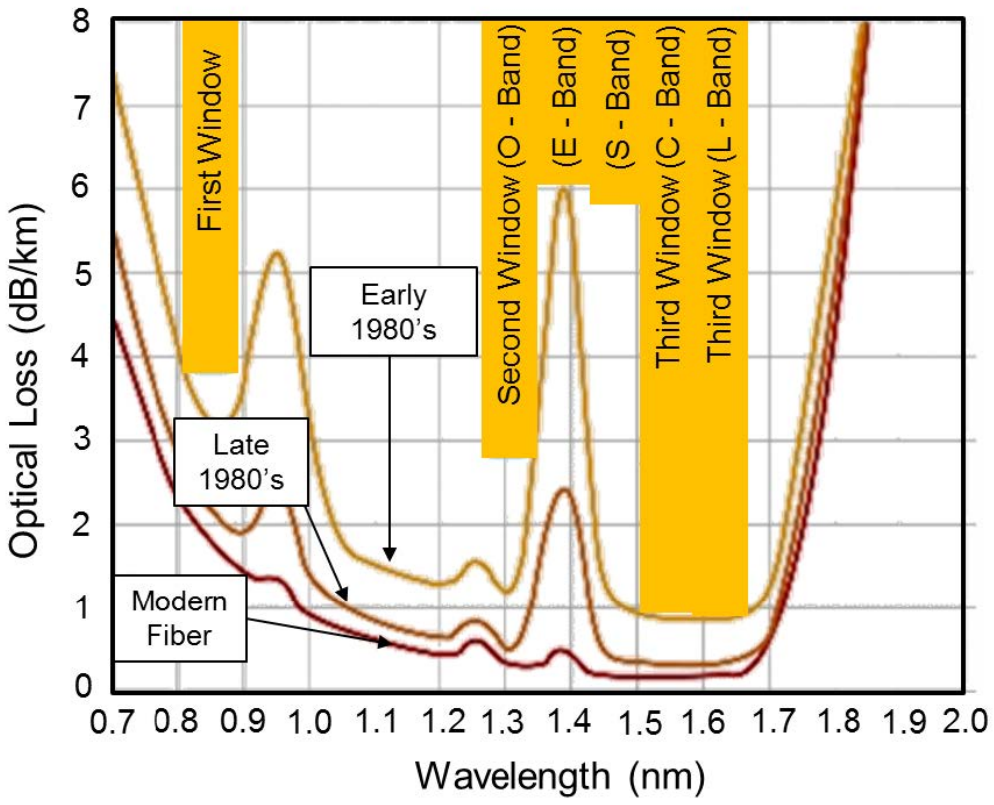

Figure 1.6: Fiber attenuation versus wavelength and the transmission windows with different telecom bands indicated. Modified from [50].

regime for $\lambda > 1400$ nm compared to visible light regime. This leads to a more relaxed constraint on the permissible transmission power and beam width from the visible to IR wavelengths > 1400 nm [37, 38, 48, 49]. Please refer to the next Section for eye-safety calculations.

In practical system implementation, IR systems operating in the O-to-L bands (1260 nm to 1625 nm) could benefit from the existing telecom facilities [50]. The low-loss optical fiber technology in the telecoms bands, as shown in Fig. 1.6, facilitates an infrastructure that carries a huge bandwidth covering not only over intercontinental distances but also within our homes.

This is exemplified in the quickly expanding Fiber-To-The-Home (FTTH) and Fiber-To-The-Building (FTTB) network with Europe reaching more than 35.9 (59.6!!) million subscribers in 2015 while the total FTTH sub-

scribers in the United States (US) has surpassed 100 million in 2014 [51, 52].

In fact, this huge bandwidth can be harvested also for wireless short reach by tapping off the light signal propagating in the fiber, and redirecting it to free space for communication. The system implementation can be potentially low-cost by reusing fiber communication devices which are available commercially. Also, it can benefit from the possibility of direct-feeding of high-speed signal from the access networks. Besides, the backbone indoor network can be implemented by an optical fiber (e.g. SMF, Multimode Fiber (MMF)) distribution network for high-speed information transfer.

1.3 Regulations and light effects

As the optical beams will be propagating in free space, it is a must that skin- and eye-safety limits are taken into account. However, since the optical power limit for eye-safety is lower (more stringent) than the limit for skin-safety, the maximum permissible exposure (MPE) required for eye-safety is used in this thesis. The Accessible Emission Limit (AEL) can be calculated as follows:

$$AEL = MPE \cdot \pi r^2 \tag{1.1}$$

where Maximum Permissible Exposure (MPE) [16] is the reference power density limit that a person can be exposed to without risk of injury, πr^2 is the beam area in which the beam radius, r, is commonly calculated at 63% or 87% power level, i.e. at $1/e$ or $1/e^2$, respectively [53]. Fig. 1.7 shows the different MPE values for different wavelength for several exposure duration. Much higher MPE value is given for wavelengths above 1400 nm. This means a more relaxed optical power constraint is attainable for infrared beams of wavelengths above 1400 nm compared to shorter wavelengths in visible light communication.

Regarding eye-safety, the Maximum Permissible Exposure (MPE) is expressed in W/m^2 and is typically defined for full human pupil opening of 0.39 cm^2 [54]. Infrared light with a wavelength longer than about 1400 nm is absorbed by the transparent parts of the eye before it reaches the retina, which means the MPE is higher than for visible light [54]. This is a major reason for which our system opted for 1.5 μm wavelength region.

Another aspect to be considered, is that VLC and IR FSO systems are prone to ambient lighting, which contributes shot noise in the photoreceivers. The

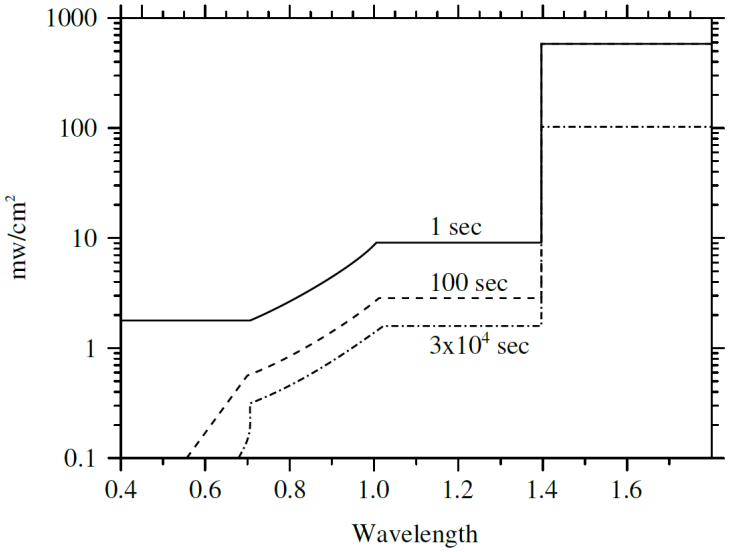

Figure 1.7: The maximum permissible exposure versus wavelength for several exposure duration [37].

effects are more severe in a VLC system since it shares the same spectrum as lighting sources such as LED, sunlight, fluorescent lamps and to some extent, the incandescent lamp [37]. An incandescent lamp, which has a high spectral content in the IR spectrum does more harm to the IR system but incandescent lamps are now being gradually replaced by fluorescent and LED lamps.

1.4 The BROWSE project

The work reported in this thesis is following the Beam-steered Reconfigurable Optical-Wireless System for Energy-efficient communication (BROWSE) Advanced Grant project, funded by the European Research Council within the Seventh Framework Program (FP7). Because of the shortage of available radio spectrum, the BROWSE project's mission was to take a radical approach by performing wireless communication using the optical rather than the radio spectrum.
A brief description of the BROWSE project will follow, then a deeper look into the theory behind optical wireless communication will be given. Finally, this thesis will focus on devices localization and tracking techniques.

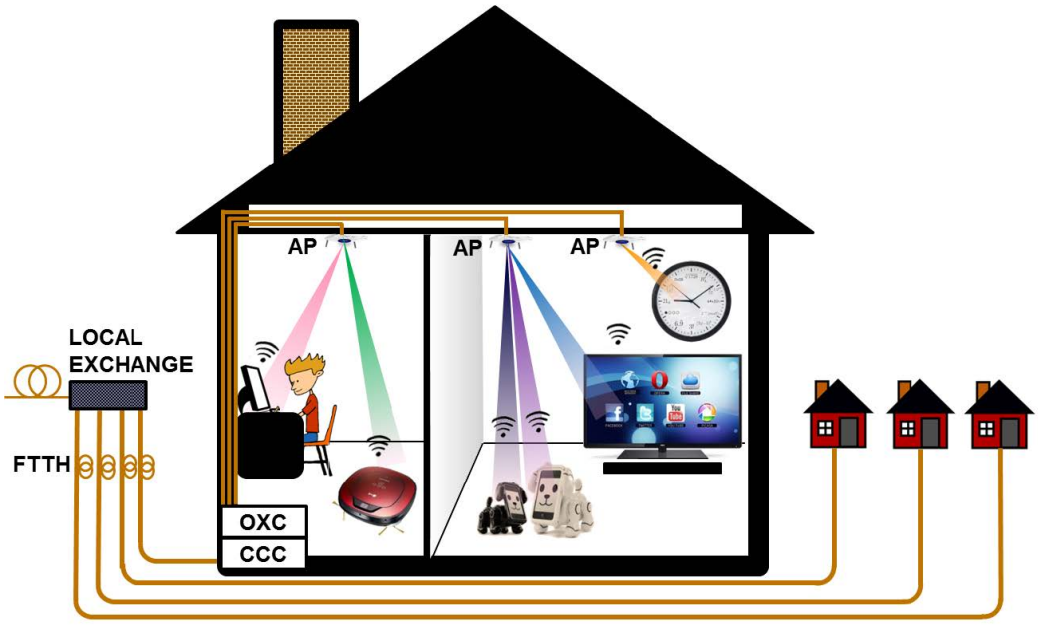

Figure 1.8: Architecture of BROWSE project's hybrid optical-radio wireless smart building. AP: Access Point, OXC: Optical Cross-Connect, CCC: Central Communication Controller.

The BROWSE project proposed to deploy narrowly confined optical pencil beams aided by fast beam steering for ultra-high capacity interference-free communication.

The proposed architecture of the in-building hybrid optical-radio wireless equipped home with optical beams is shown in Fig. 1.8. The model can be divided into three major sections, being the Central Communication Controller (CCC), the wireless communication medium and the receiving end. The fiber backbone network routes data signals in a point-to-point manner from the CCC to each AP. Multiple APs, with each containing a 2D optical beam-steering device, can be employed to increase the coverage area, to act as a backup link in the case where the beam from a certain direction is blocked, and to aid in user localization and tracking.

1.4.1 Central Communication Controller

At the transmitter side, the CCC manages the interfacing between the indoor and outdoor networks. The indoor network is totally independent from the access network. In the case in Fig. 1.8, data signals from the access network are transported to the smart home using the FTTH technology while the in-building network uses Fiber-In-The-Home (FITH) technologies. Network interfacing protocols, routing logics and autonomous resource management are installed at the CCC. Data signals are routed by the Optical Cross-Connect (OXC) to the corresponding APs through the optical fiber distribution network. SMF or MMF fibers can transport a large amount of data to the APs. The fundamental intention of the system is to provide a single beam to each individual device. In order to provide multiple beams simultaneously, multiple tunable lasers will be required in the CCC.The selection of the source to be installed will depend on the timely progress and costs of these sources. In order to reduce the cost of the CCC, a time-slotted system can be possible, sharing resources between multiple devices over time. The capacity per device will decrease, but so will the cost of the CCC.

1.4.2 Wireless communication medium

In the wireless communication medium, free-space LoS pencil beam techniques are used for the downlink. For the uplink, early studies with 60 GHz radio and radio over fiber have been proven promising. An all-optical duplex communication will be later presented.In each individual room one or more APs, each equipped with a beam-steering module termed as Pencil Radiating Antenna (PRA), and eventually a Radio Access Point (RAP), are implemented depending on the size of the coverage area. As LoS is necessary for optical pencil beams, beam steering is necessary in order to direct the LoS beams from the AP toward multiple users. Important considerations for selecting a steering method include the ease of installation, enabling plug-and-play, without any local processing and without local powering.The beam-steering module has to be accurate, reliable, has to support scalability, has to require little or no maintenance, has to have high response speed and a good coverage area, and its beam steering should be easily controllable from a remote location (i.e. the CCC). Taking into account these key requirements, the use of passive diffraction gratings for beam steering in cooperation with remote wavelength-tuned source in the CCC has been used.

The passive nature of the beam-steering module renders it independent from moving parts or electronically-controlled elements, which may be prone to failure.In support for mobility, it is important that users are quickly localized and also tracked in order to minimize connection latency or failure, and this is where this work is mainly focused in. For this purpose, radio and optical localization techniques can be employed to locate and track the positions of the mobile devices. Radio techniques can be used to implement coarse localization.

The camera based localization is the one proposed in this thesis, and will be therefore accurately discussed.

1.4.3 Receiving End

At the receiver side, the mobile device is equipped with a simple optical receiver, and eventually a radio transmitter, in order to receive the downlink optical signal, and to transmit a radio signal for the uplink. To improve reliability, the system can be backed up at the WiFi bands for bi-directional communication in case the optical link fails due to loss of the LoS condition. Finally, to benefit from the already existing facilities used in the core, metro and access networks, the system is proposed to operate in the 1500 to 1600 nm telecom band.In the case of LoS blocking, with the use of multiple APs, another AP can establish an LoS path.

Chapter 2

Beam Steering

An overview of related work in optical beam deflection or steering techniques is discussed in this chapter. The first part of this chapter gives a brief introduction to these techniques, their principle of operation, and the related work from former and recent years, which employed such techniques. Then, the state-of-the-art free-space communication systems for indoors which employ optical beam steering techniques are detailed. There are various types of optical beam steering methods each with its specific benefits and drawbacks in terms of power consumption, mechanical motion, steering angle, speed of response, fabrication complexities, maintenance and control requirements, etc. Refractive and diffractive optical elements and optical phased arrays are popular techniques to implement devices of which the fundamental functionality is to direct or sense optical beams to/from a particular target(s) or position(s). As such, it is not uncommon that many areas of work share the same techniques for different applications. These techniques can be used for sensing, scanning, pointing, tracking, switching and steering. They are used in various applications such as bar code scanning, Light Detection and Ranging (LIDAR), spectroscopy, projectors, 3D imaging, and confocal microscopy. In general, steering elements can be divided into two large categories, i.e. active and passive elements.

2.1 Active Beam steering techniques

Active beam steering modules require electrical powering to the steering element, in order to direct beams where needed. This can happen by creating heat, electro-magnetic fields or mechanical movements to enable a change of state, as required by the particular steering element. Here, we explore discrete element techniques and optical phased array techniques for optical beam steering. Optical Phased Arrays (OPAs) enable optical beam steering without moving parts and are capable of creating phase profiles which steer, focus, fan out or correct phase aberrations on a beam [55]. The most common active beam steering techniques will now be presented.

Steering Mirror

An effective and simple choice of steering is by simply reflecting a beam using a moving reflective surface, e.g. a mirror, in combination with rotation platforms. The movements of these mounts can be controlled using motors and galvanometers [56] or actuators, such as piezo actuators or voice coils. Light weight and fast tuning mechanical mirror-based gimbals are commonly used in space-based (satellite communication) applications for scanning and tracking [57]. The main drawback is that mechanical moving parts are prone to mechanical wear, vibrations, and thermal expansion. Therefore, it does not support random pointing, but only continuously addressable scanning due to the change in the movement of the mirror until it achieves the desired position. Also, due to inertia, they are limited in steering speed [58]. Devices which support random pointing could save latency time needed for the mechanical tuning of the mirror.

Micro-electro-mechanical system optical phased arrays

One variant of OPA implementation is by using Micro-Electro-Mechanical System (MEMS) mirrors. Such mirrors are small and they are lightweight, and therefore, are more power-efficient and have faster response time (up to kHz range) compared to a single macroscopic mirror. However, they usually don't allow wide angle steering. Also, as the size of the mirrors is typically in the 100's of micrometers to millimeters range, the aperture sizes are limited to a few millimeters [59]. In terms of speed, in comparison to electromagnetic and electro thermal actuation, electrostatic actuation has negligible power

consumption and could operate at a higher speeds of up to $\sim$ 10 kHz [60]. MEMS phased arrays can also be achieved using Variable Blaze Gratings (VBGs) [61] or microlens phased array.

Liquid crystal optical phased arrays

Liquid Crystal (LC) based phased arrays require very low power consumption (low electrical drive voltages) and can support large apertures ($10 - 50$ cm) [55, 62, 63]. For example, a 10 cm device has a typical dissipation of approximately 1 W [62]. LC devices can achieve up to 20° deflection with a large number of precisely controlled beams ($10^4 - 10^5$). LC devices are known to be insensitive to accelerations.With only < 10 V applied on the electrodes, suffcient refractive index change can be achieved to enable full-wave differential phase shifts. LC techniques, however, are limited in speeds to < 10 kHz [64].When a voltage is applied, the LC molecules rotate. Consequently, an incident beam will see a refractive index change due to the birefringent behavior of the LC molecules. This effectively causes a changed optical path length or phase shift.

Photonic integrated circuits optical phased arrays

OPAs based on waveguide phased array allow independent control in the array of uncoupled channel waveguides to achieve the wanted steering characteristics. The working principle of such an OPA is based on the interference of individual radiating optical waves with their neighboring waves forming the desired wavefront in a particular direction.Even if the electro-optic steering is fast, in the order on nanoseconds, larger steering angles are difficult to achieve, as well as higher effciencies, larger apertures and the extension to two-dimension [55]. Work in recent years has shown tremendous progress in Photonic Integrated Circuit (PIC) OPAs.

Electro-optic deflectors

In electro-optic deflectors, the refraction index of a material is induced by an applied electric field, which results in a change in the direction of propagation. Electro-optic materials, such as Lithium Niobate, exhibit a refractive index change when an external electric field is applied. This beam deflector was reported in [65]. A deflection angle of 14.3° was observed by apply-

ing ±250 V with approximately 5 μA current to the Potassium Tantalate Niobate crystal. The voltages needed to induce phase changes are normally high at a few hundred of Volts. In this case, the effciency is independent of the angular steer range. Furthermore, this approach provides a continuous angular coverage with high pointing accuracy with $>$ 10 Gigahertz (GHz) bandwidths.

Acousto optic deflectors

Acousto-optics is based on the interaction between sound and light. Acousto-optic devices have been made possible from the discovery of materials having excellent acoustical and optical properties with large photoelastic constants. Materials having a large refractive index give an added advantage [66, 67, 68]. The principle of acousto-optic deflectors is to deflect a beam to different angular positions by an accompanying acoustic wave, by varying the acoustic frequency. By applying a Radio Frequency (RF) signal on an acoustic transducer to generate an acoustic wave through a crystal, a periodic modulation on the refractive index is induced via the elasto-optical effect [69], thus, the device behaves like a grating. In this way, an incident coherent optical beam will be diffracted. This is also known as the acousto-optic diffraction. The speed of these devices can be in a few microseconds range [56]. However, acousto-optic deflectors are limited in their total angular range and may suffer from shift in optical frequency as sound waves spread as they propagate.

Electrowetting

Electrowetting Microprisms (EMPs) use the electrowetting modulation of liquid contact angle to realize the refraction characteristics of prisms [70]. Contact angle of several tens of degrees are achievable while switching speeds are limited to several milliseconds due to hydrodynamic response of the droplet. In 2006, N.R. Smith et al. demonstrated continuous beam steering of 14° with a liquid index of 1.359. Switching speeds of milliseconds and a high effciency that is independent of deflection angle is possible [71]. Fig. 2.1 illustrates the EMP device.

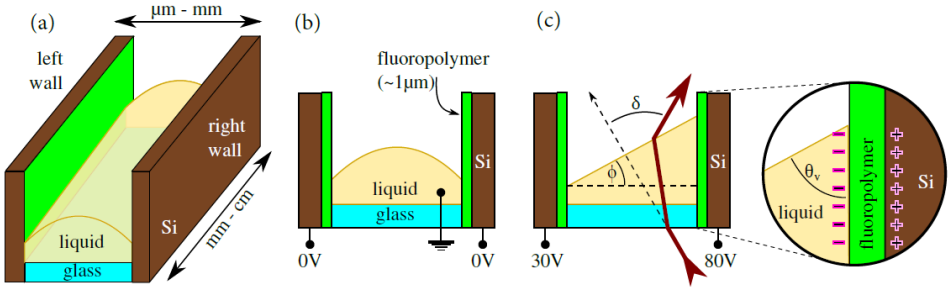

Figure 2.1: EMP structure [71]: (a) Angle view of the channel geometry, (b) and (c) EMP materials, voltage connections, prism apex angle (ϕ), deflection angle (δ), and liquid-fluoropolymer contact (θ_v).

2.2 Passive Beam steering techniques

This section gives an overview of the available passive beam-steering techniques which do not require any powering or movement. These passive devices are usually wavelength or frequency dependent.These methods are widely used in spectrometry and interferometry.

Holographic deflectors

Holography is also known as wavefront reconstruction photography [72] and was first demonstrated by Dennis Gabor [73]. It is a technique that enables the reproduction of three-dimensional (3D) images by using coherent radiation of a monochromatic beam or laser which has both temporal and spatial coherence. Holograms can be constructed, as shown in Fig. 2.2, by illuminating part of a coherent monochromatic wave, known as the reference beam, on a photosensitive material or photographic plate. The other part of the beam, known as the object beam, is then illuminated on the object to be recorded. The beam that reflects from the object has amplitude and phase variations which represent the surface of the object. This reflected beam then interferes with the reference beam forming a complex interference pattern with magnitude and phase information at the photographic plate. The interference pattern is recorded on a fine grain holographic or photographic film. The developed piece of film is known as a hologram.

In 1976, J.P. Huignard et al. patented an electro-optical deflection apparatus invention using holographic gratings together with a primary beam

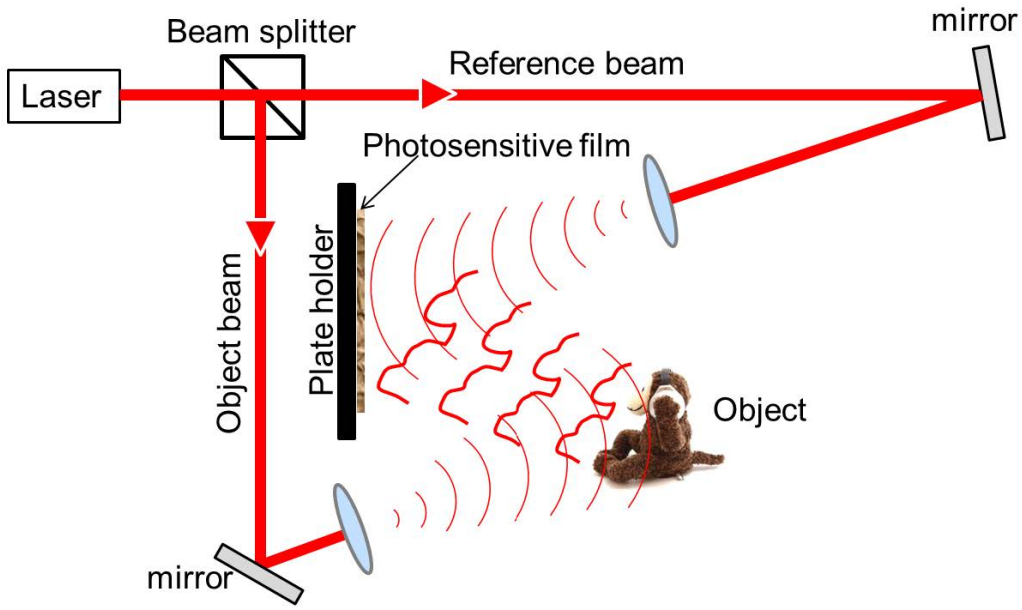

Figure 2.2: A holographic recording setup. Object image is captured by the interference of the reference beam and the object beam. The 3D image is recorded on a photosensitive film placed on the plate holder.

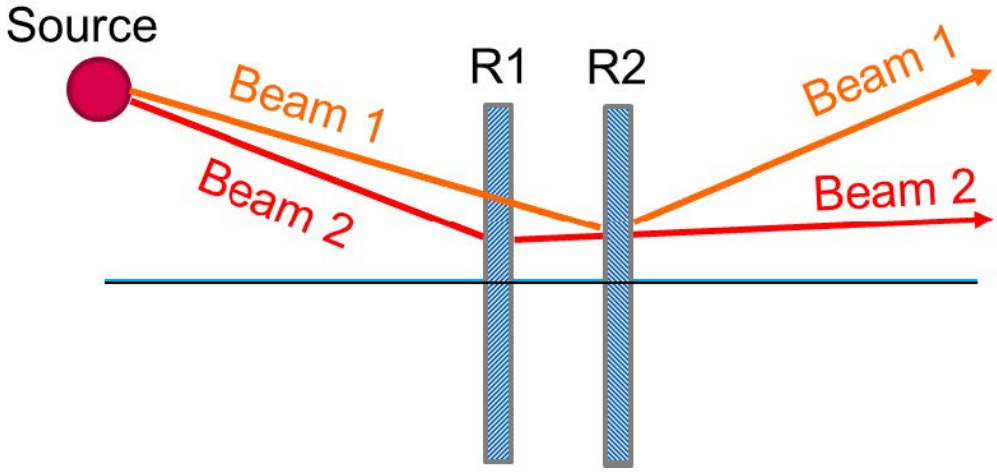

Figure 2.3: The use of holographic gratings, each for the deflection of one wavelength, in the invention of electro-optical deflection apparatus by J.P. Huignard et al. [74].

deflector capable of deviating the incident beams into a multiple directions at the source [74], see Fig. 2.3. The invention provides a deflection system which was attained by providing N holographic diffraction gratings, in which each of the gratings diffracts into only one of the N-directions. The gratings are positioned consecutively next to each other with each grating diffracting at least one incident beam. Each of the incident beams arrive at a slightly different incident angle. The output beams are then diffracted at an angle substantially larger than the incident angle.Other important experiments have been performed based on holographic delflectors, showing promising results in terms of steering techniques.

Arrayed Waveguide Grating

An Arrayed Waveguide Grating (AWGr) consists of an input waveguide, a free propagation zone where the beam diverges, a zone with many waveguides having slight length difference, a second free propagation region where the beam converges with equal amplitude and phase distribution [75], and an array of output waveguides. It is designed such that the field of an incoming beam is split into an array of output beams such that the different wavelengths which enter the input waveguide are directed to different output waveguides [76].
Physically, the linearly increasing length of the array waveguides will cause the phase change, to vary linearly along the output aperture [75]. AWGrs are also known as phased arrays (PHASARs) or Waveguide Grating Router (WGR).In this thesis, the acronym AWGr is used instead of AWG in order to avoid confusion with the acronym AWG to abbreviate arbitrary waveform generator.

The principle of operation can be explained by a simple Mach-Zehnder Interferometer (MZI) with unequal path lengths, as shown in Fig. 2.4. A MZI is a device which splits a beam into two paths by which one path introduces a relative phase shift which can be varied by changing the length of one path or by introducing a change of refractive index in one path. Passive couplers, which are made by changing the length of one arm, are commonly used in fiber optic communication. With a change of path length difference, ΔL, in one path, the phase difference, $\Delta\phi$, is given by:

$$\Delta\phi = kn_{eff}\Delta L \tag{2.1}$$

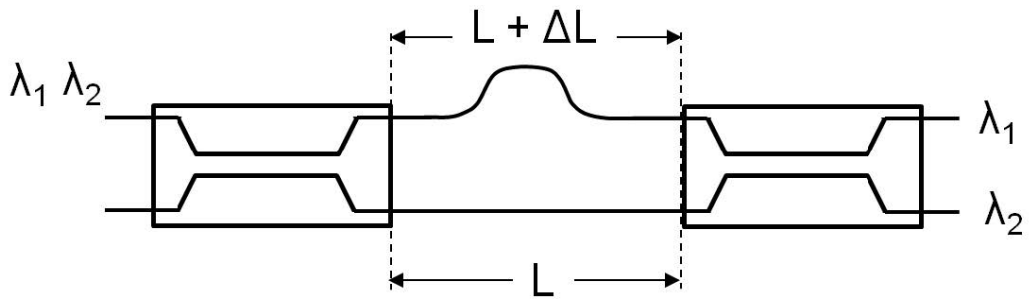

Figure 2.4: MZI structure illustrating the path length change to induce a phase change in one path.

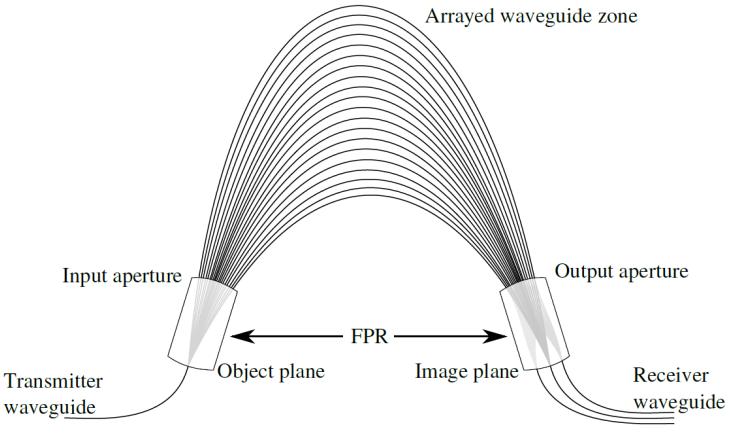

Figure 2.5: AWGr layout with linearly increasing length in the arrayed waveguides. FPR: Free Propagation Region [76].

where k is the wave vector $2\pi/\lambda$ and n_{eff} is the effective refractive index of the waveguide.

AWGr can be seen as an extension to the MZI principle, in which it consists of multiple waveguides of linearly increasing constant path lengths thereby creating a linear phase shift in each waveguide, see Fig. 2.5. The length difference can be calculated using [76]:

$$\Delta L = m\frac{\lambda_c}{n_{eff}} \tag{2.2}$$

where m is the order of the array, λ_c is the central wavelength and n_{eff} is the effective refractive index of the guided mode.

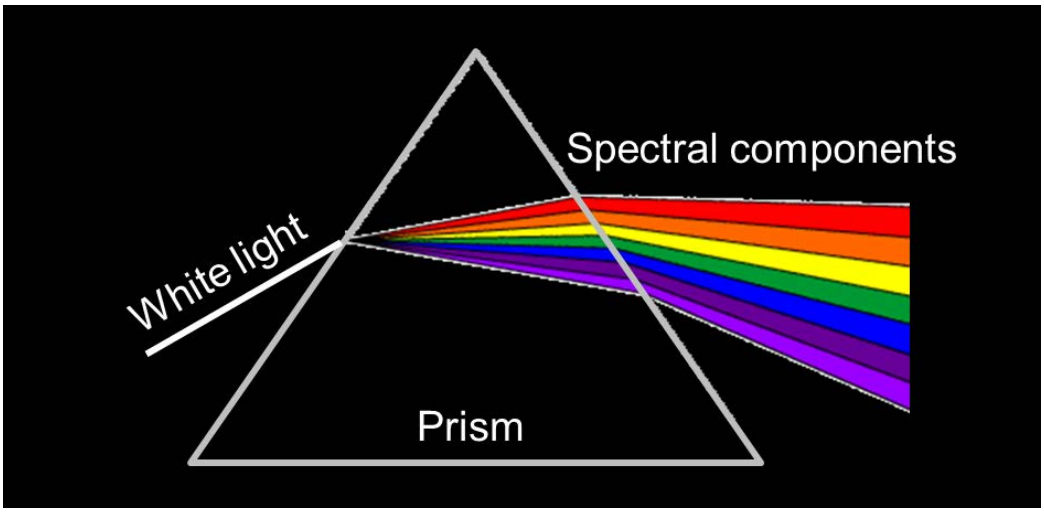

Figure 2.6: Prism and the spectral components of white light.

An interleaved multiplexer can be constructed using a higher order AWGr at the first stage, where each output waveguide directs an output with a specific Free Spectral Range (FSR). By cascading a second stage AWGr, the output corresponding to one diffraction order is further separated into individual channels.

Prisms

Dispersive optical prisms usually have a triangular geometry. Triangular prisms are used to disperse light by changing the angle of refraction which is dependent on the prism's refractive index, the geometry (the apex angle), the outer refractive index, and the optical incidence angle at the interface. The refractive index which an optical ray wavelength sees, is also dependent on its wavelength or frequency. Therefore, each different wavelength is refracted to a different angle, as can be calculated using Snell's Law. Consequently, light is dispersed into its spectral components. This is known as angular dispersion. The effective refractive index increases as wavelength decreases. However, the angular dispersion of a prism is typically smaller than diffraction gratings. The light path deviation, δ (see Fig. 2.7), from its original path, can be derived using the Snell's law of diffraction and trigonometry, with the following basic equations:

$$n(\lambda)_{ambience} \cdot \sin(\theta_1) = n(\lambda)_{prism} \cdot \sin(\theta_2) \tag{2.3}$$

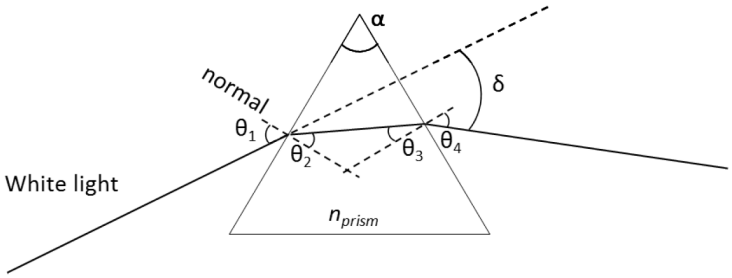

Figure 2.7: Refraction through a prism.

$$n(\lambda)_{prism} \cdot \sin(\theta_3) = n(\lambda)_{ambience} \cdot \sin(\theta_4) \tag{2.4}$$

$$\theta_2 + \theta_3 = \alpha \tag{2.5}$$

where θ_1 is the incidence angle on the first surface, θ_2 is the refracted angle of the first surface, θ_3 is the incidence angle on the second surface, θ_4 is the refracted angle at the second surface, $n(\lambda)_{ambience}$ is the refractive index outside the prism, $\lambda)_{prism}$ is the wavelength-dependent refractive index of the prism, and α is the apex angle of the prism.

Finally, the wavelength-dependent deviation angle, $\delta(\lambda)$, is derived to be the following:

$$\delta(\lambda) = \theta_1 - \theta_2 + \theta_4 - \theta_3 \tag{2.6}$$

$$\delta(\lambda) = \theta_1 - \alpha + \arcsin\left\{ n(\lambda)_{prism} \cdot \sin\left[\alpha - \arcsin\left(\frac{\sin\theta_1}{n(\lambda)_{prism}} \right) \right] \right\} \tag{2.7}$$

where the third term in represents the wavelength-dependent deviation angle. The change in the refractive index with wavelength is known as dispersion and it varies according to material.

Diffraction Gratings

Beam steering based on diffractive optics is studied in detail as this is the core technique used in this thesis. Diffraction gratings, like prisms, are one of the earliest forms of passive dispersive media used for beam steering. Fig. 2.8 shows the different types of gratings. The first grating was invented in 1785 to observe light spectra. Gratings are wavelength-dependent and operates by diffracting light beams. The principle of diffraction stems from the ability of waves to bend, leading to a divergent profile as it propagates away from its

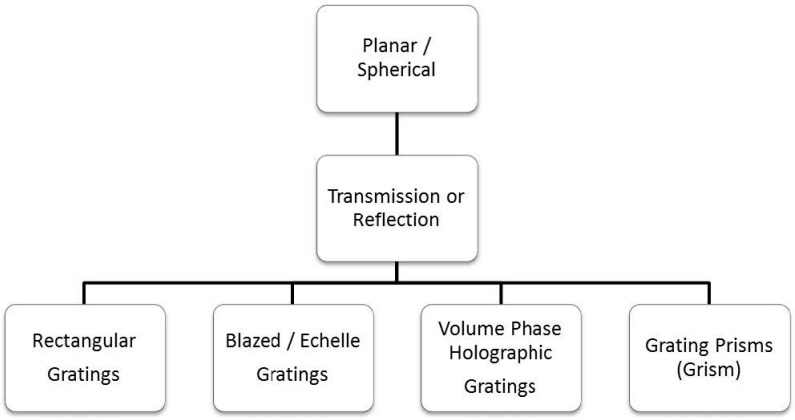

Figure 2.8: Overview of types of gratings.

source. At the same time, waves coincide constructively and destructively with neighboring waves to give rise to interference. This phenomenon can be seen in the propagation of light through a single slit, thus, forming an array of bright and dark intensity patterns on the resulting screen. These bright patterns are the spots where diffracted light beams are constructively interfering. Physically speaking, according to the Huygens-Fresnel's principle, any unobstructed point of a wavefront, at a given instant of time, serves as a source of spherical secondary waves (wavelets), with the same frequency as that of the primary wave. The amplitude of the optical field at any point beyond the new source plane is the superposition of all these wavelets. This leads to the forming of a new wavefront which envelopes the wavefronts of the secondary waves [77]. The corresponding positions of the bright spots can be calculated using the famous grating equation for both transmission and reflection gratings, as shown in Fig. 2.9:

$$m\lambda = d(n_1 \sin\theta_i \pm n_2 \sin\theta_m) \tag{2.8}$$

where m is the diffraction order, λ is the wavelength of interest, d is the period of the grating or distance between two neighboring grooves, θ_i is the incidence angle measured from the grating normal, θ_m is the diffraction angle measured from the grating normal, and n_1 and n_2 are the refractive index of the medium of incident beam and diffracted beam, respectively. Furthermore, in case of reflection grating placed in air, the following equation holds:

$$n_1 = n_2 = 1 \tag{2.9}$$

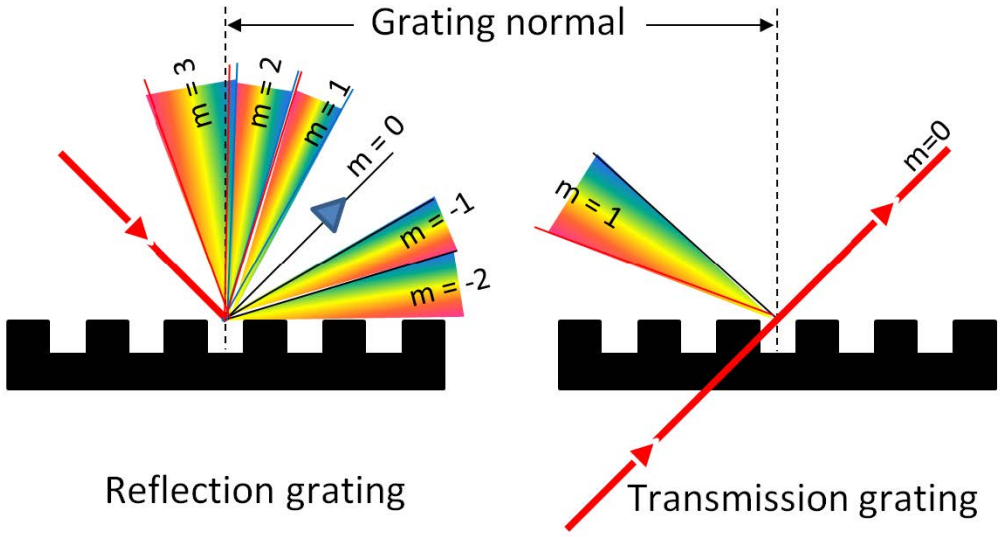

Figure 2.9: Diffraction spectra at different orders for transmission and reflection gratings.

The $\pm$ operation is dependent on the angle with reference to the optical axis. The zero-th order mode always exists giving rise to a non diffracted transmission or specular reflection beam. The zeroth order mode occurs when $\theta_i = \theta_m$, where most of the optical power is confined in. In order to optimize for maximum optical power in a desired diffraction order or angle, a blazed grating is used. Blazed gratings are designed for maximum efficiency at an order other than the zero-th order, with minimized residual power in all other orders. Blazed gratings which have a large blaze angle are known as echelle gratings. Notice from the grating equation also that only spectral orders where $|m\lambda/d| < 2$ can exist.

The angular dispersion can be derived from the derivative (where θ_i is kept constant):

$$\frac{d\theta}{d\lambda} = \frac{m}{d\cos\theta_m} \tag{2.10}$$

By substituting m/d from (2.8) into Equation (2.10), we obtain the general dispersion equation:

$$\frac{d\theta}{d\lambda} = \frac{\sin\theta_i + \sin\theta_m}{\lambda\cos\theta_m} \tag{2.11}$$

In a retroreflective or Littrow configuration, the incidence angle, θ_i, is equal

to the diffracted angle, θ_m, reducing the grating equation (2.8) to:

$$m\lambda = 2d\sin\theta_m \tag{2.12}$$

and the angular dispersion in Littrow configuration can be further reduced to:

$$\frac{d\theta}{d\lambda} = \frac{2\tan\theta_m}{\lambda} \tag{2.13}$$

which is only valid when the angle of incidence is fixed [78]. In addition, when the angle of incidence is changing (for e.g. for the consecutive grating placed after the first), by differentiating the grating equation (2.8), we have [78]:

$$md\lambda = d\left(\cos\theta_i d\theta_i + \cos\theta_m d\theta_m\right) \tag{2.14}$$

Since in Littrow configuration, $\theta_i = \theta_m$ and $d\theta_i = d\theta_m$:

$$\frac{d\theta_m}{d\lambda} = \frac{m}{2d\cos\theta_m} \tag{2.15}$$

Interestingly, by substituting m/d from Equation (2.13), we see that the angular dispersion is only half that of the angle obtained using fixed angle of incidence [78]:

$$\frac{d\theta_m}{d\lambda} = \frac{\tan\theta_m}{\lambda} \tag{2.16}$$

As shown in Fig. 2.10, the wavelengths are repeated in different orders. Also, at order $m > 1$, several ranges of wavelengths from different orders exists. This leads to overlapping wavelengths when they are diffracted into the same direction. When $\lambda/d \ll 1$, a large number of diffraction orders exists. High order gratings have a design wavelength which is much longer as can be seen in the following relation: From Equation (2.13),

$$m\lambda = 2d\sin\theta_m \tag{2.17}$$

$$\frac{m}{2}(2\lambda) = 2d\sin\theta_m \tag{2.18}$$

$$\frac{m}{n}(n\lambda) = 2d\sin\theta_m \tag{2.19}$$

where n is an integer and $n \neq 0$. The resolution of gratings is taken from the minimum wavelength difference which the grating is able to resolve between two wavelengths. Generally, the higher the number of grooves, so the smaller d, the higher the resolution will be. Another important parameter, especially in bandwidth sensitive applications, is the spectral bandpass of a grating [81] in an optical system. The spectral bandwidth consists of the range of wavelengths that successfully falls onto the detector area or exit slit.

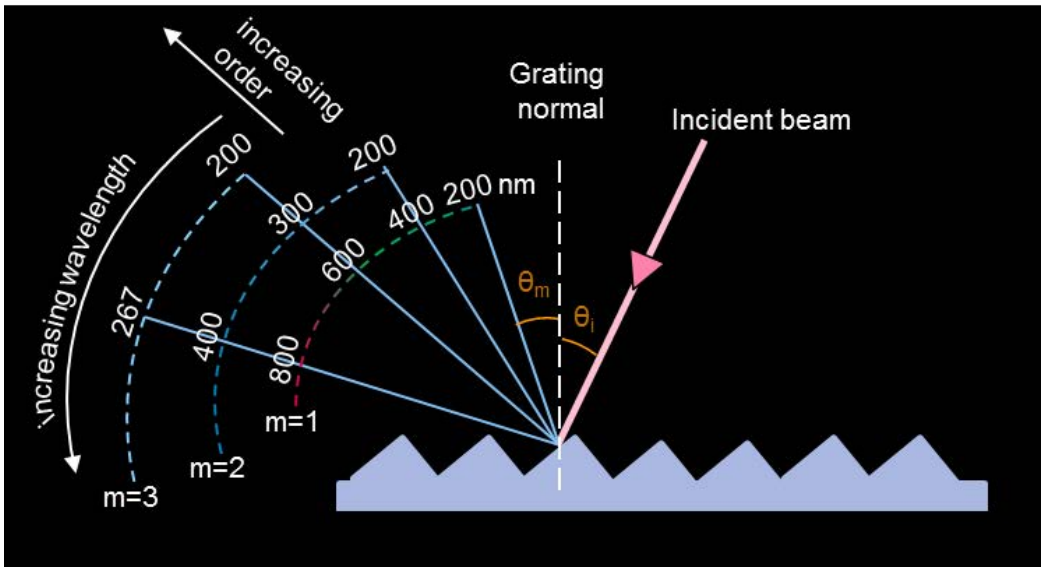

Figure 2.10: A comprehensive description of the basic diffraction orders with the overlapping spectra, which is valid for both transmission and reflection gratings operation. The basics of this illustration can be found in [79, 80].

Virtually imaged phased array

A Virtually Imaged Phased Array (VIPA) is a wavelength-dependent device capable of providing large angular dispersion; it has a simple structure, has low cost, and has low polarization dependence [82]. The structure of a VIPA, as shown in Fig. 2.11, is made of a thin plate of glass with a high-reflection film coating on one side and a 100% reflection film on the other side. There is an antireflection-coated window for the input beam. In the first pass, for e.g., 5% of the input light passes through and diverges after the beam waist. 95% of the light is reflected. This 95% of light hits the second surface but at a point which is displaced by an amount, d, from the first point. Another 5% of the 95% beam passes through. In consecutive reflections, there will be many beams each separated by a distance of d. A virtual image of the beam waist is formed with constant spacing of 2t along the normal of the input side of the plate. Similar to a grating, the output light waves interfere and form a beam which propagates in a direction similar to the Bragg angle of diffraction. On the contrary, as the reflectivity has no phase difference nor angle difference, the beam profiles in all light paths are the same. When the field magnitude in a beam is constant at the output

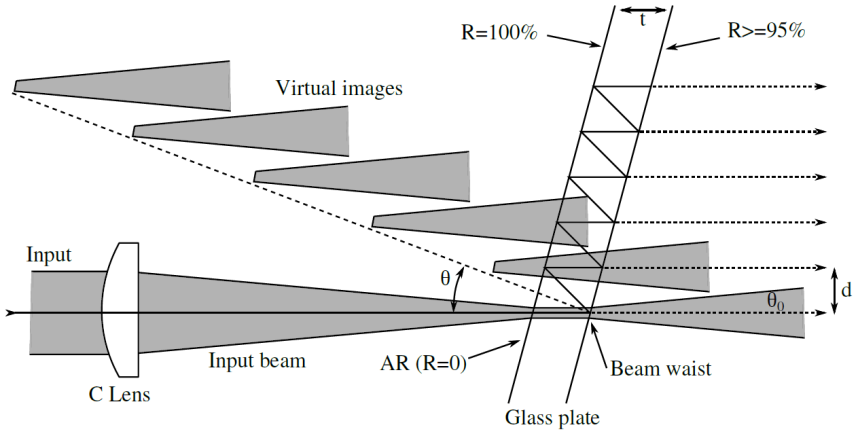

Figure 2.11: VIPA structure with a glass plate of approximately 100 μm thick [82]. t: Thickness of the plate, R: Reflectivity, C: Cylindrical, d: spacing of light paths, θ: incident angle in side the glass plate.

peak direction, the far field of the output beam is Lorentzian. The spacing between the light paths can de determined using:

$$d = 2t \sin\theta \tag{2.20}$$

The difference in path lengths, P_L, between adjacent beams:

$$P_L = 2t \cos\theta \tag{2.21}$$

The angular dispersion can then be determined approximately using $n \cot\theta$ factor. The corresponding factor for a diffraction grating is $2 \tan\theta_m$ [83]. The VIPA equation is given in [84] as:

$$m\lambda = 2n_v t \cos(\theta - \theta_o) \tag{2.22}$$

where θ_o is the output angle and n_v is the refractive index of the plate material. The angular tuning range, $\Delta\theta_o$, when tuning over one FSR from λ to $\lambda + \Delta\lambda_{FSR}$ is [84]:

$$\Delta\theta_o = \theta_{o,2} - \theta_{o,1} = \arccos\left(\frac{\lambda}{2n_v t} m\right) - \arccos\left(\frac{\lambda}{2n_v t} \frac{m^2}{m-1}\right) \tag{2.23}$$

Koonen et al. also showed that the maximum $\Delta\theta_o$ is achieved when $m^2\lambda = 2n_v t(m-1)$, i.e. when, $\theta_{o,2} = \theta$, and is $\Delta\theta_{max} = \arccos(1 - 1/m)$.

2.3 Beam steering technique in BROWSE

As discussed in the last sections, active steering techniques featured devices which require mechanical control or power for activating tuning mechanisms such as electrooptic heaters and micro-mechanical actuators. These methods also typically provide steering response in the order of milliseconds. On the contrary, the passive steering mechanisms do not require any mechanical movement or power, but are wavelength-dependent in diffractive and refractive propagation. The beam steering technique used in the BROWSE will now be presented.

2.4 Pencil Radiating Antenna

The Pencil Radiating Antenna is structured as shown in Fig. 2.12 [85, 86, 87, 88, 89]. It is constructed using two gratings to provide two-dimensional (2D) angular beam steering depending on the wavelength of the beam arriving at the PRA via the installed fiber. The beam out of the feeder fiber is collimated into a narrow beam. The first grating steers the beam in ϕ-direction and the second grating steers it in ψ-direction. The first grating has a small Free Spectral Range (FSR). The wavelengths are scanned a multiple times over ϕ-direction in the range of the FSR. The second grating has a large FSR and the beam will be scanned across the orthogonal ψ-direction. In this way, the (ϕ, ψ) plane can be covered by spots of different wavelengths.

The PRA, which functions as an area scanner, needs to be able to scan an area by scanning with beams of different wavelengths line-by-line. The range of the total angular scan and the density of scan lines are important parameters. In order to realize the scanning using cascaded blazed diffraction gratings, a basic requirement is that the first grating have a small FSR whereby a range of wavelengths of different orders are overlapped in a 1D angular direction. A second grating, placed orthogonally to the first grating will further diffract the wavelengths in an orthogonal direction to the first, hence, creating a 2D raster scan. In order to avoid overlapping beams, the large FSR of the second grating should accommodate at least the full range of wavelengths accommodated by the first grating. The range of spectrum in which it does not overlap the same spectrum in another order, m, is known as the FSR. Let us consider a spectrum between λ_L and λ_U. We denote the lower wavelength as λ_L and the upper wavelength as λ_U. We can derive the

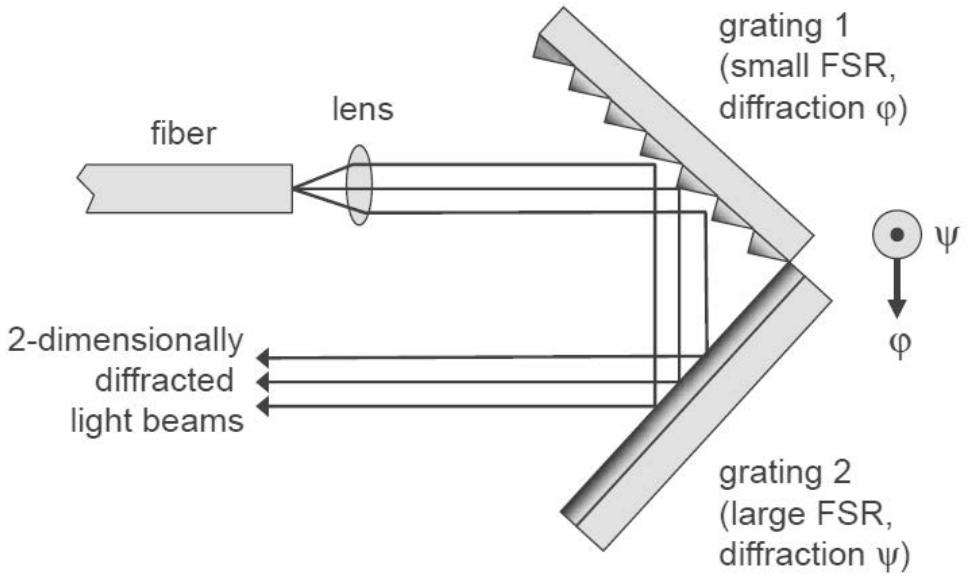

Figure 2.12: Crossed gratings for 2D beam steering by Ton Koonen et al. [84, 85].

appropriate FSR by using the lower or the higher wavelength as below:

$$m\left(\lambda_L + \mathrm{FSR}\right) = (m+1)\lambda_L \tag{2.24}$$

$$FSR = \frac{\lambda_L}{m} \tag{2.25}$$

or as below:

$$m\lambda_U = (m+1)\left(\lambda_U - FSR\right) \tag{2.26}$$

$$FSR = \frac{\lambda_U}{m+1} \tag{2.27}$$

The FSR equation can also be derived by considering that λ_1 of order m and λ_2 of order $m-1$ are diffracted to the same angle, θ_m. Therefore, the FSR can also be derived as:

$$m\lambda_1 = d\left(\sin\theta_i + \sin\theta_m\right) \tag{2.28}$$

$$(m+1)\lambda_2 = \lambda_1 - \lambda_2 = d\left(\sin\theta_i + \sin\theta_m\right)\left(\frac{1}{m(m+1)}\right) \tag{2.29}$$

where θ_i is the incidence angle and θ_m is the diffraction angle. By using Equation (2.27), assuming a wavelength range between 1500 nm to 1600

nm, for the first, small FSR grating, an FSR of 10 nm will give an order of $m = (1600/10) - 1 = 159$. For the second grating, an FSR with a minimum of 100 nm, will give the order, $m \leq (1600/100) - 1 = 15$. Note that for grating 1, many orders m are passed when tuning from λ_L to λ_U (1500 nm to 1600 nm), and that the FSRs of these orders will be slightly different [84]. After determining the order of operation, in order to have a large angular dispersion, the blaze angle of the grating should be as high as possible or the period should be as small as possible as can be deduced from the dispersion equation shown in Equation (2.10). The required groove spacing and blaze angle can be determined using the Littrow configuration equation, i.e. Equation (2.12) $m\lambda = 2d \sin\theta_m$. Note that Equation (2.12) only hold for a λ where $\theta_i = \theta_m$, so, in Littrow mount where $\lambda = \lambda_{Littrow} = \frac{2d}{m} \sin\theta_m$. Correspondingly, the diffraction angle can be derived from the grating equation (2.8) for a constant incidence angle as:

$$\theta_m = \arcsin\left(\sin\theta_i - \frac{m\lambda}{d}\right) \tag{2.30}$$

By using Equation (2.30) we can determine the largest scan range in a particular order. Fig. 2.13 illustrates this relation in which the scanning range (delta diffraction angle between the largest and smallest wavelengths) increases as the blaze angle increases and groove spacing decreases. As the blaze angle increases, the scanning angle range also increases. The figure is computed for an FSR of 10 nm with $\lambda = 1600$ nm, therefore, $m = 159$ with steered wavelengths between 1590 nm and 1599 nm. The computed maximum angle that can be achieved at a blaze angle of 89° (7.86 grooves/mm) with wavelength tuning between 1590 nm and 1599 nm is approximately $\theta_{m_max} = 6°$. Using the same method to determine the limit of steering on the low dispersive grating, using an FSR = 100 nm, with $\lambda = 1600$ nm, therefore, m = 15 with steered wavelengths between 1500 nm and 1599 nm. The computed maximum angle that can be achieved at a blaze angle of 89° (83.33 grooves/mm) with wavelength tuning between 1500 nm and 1599 nm is approximately $\theta_{m_max} = 26°$. If we do a sweep across the gratings using a wavelength range between 1499 nm to 1631 nm, we see that for the highly dispersive grating, the wavelengths will sweep across orders 155 to 169, and for the low dispersive grating from orders 14 to 16. The corresponding tabulation of diffracted spots is shown in Fig. 2.14 and Fig. 2.15, respectively. Do note that as the wavelengths are swept across different orders, the angular

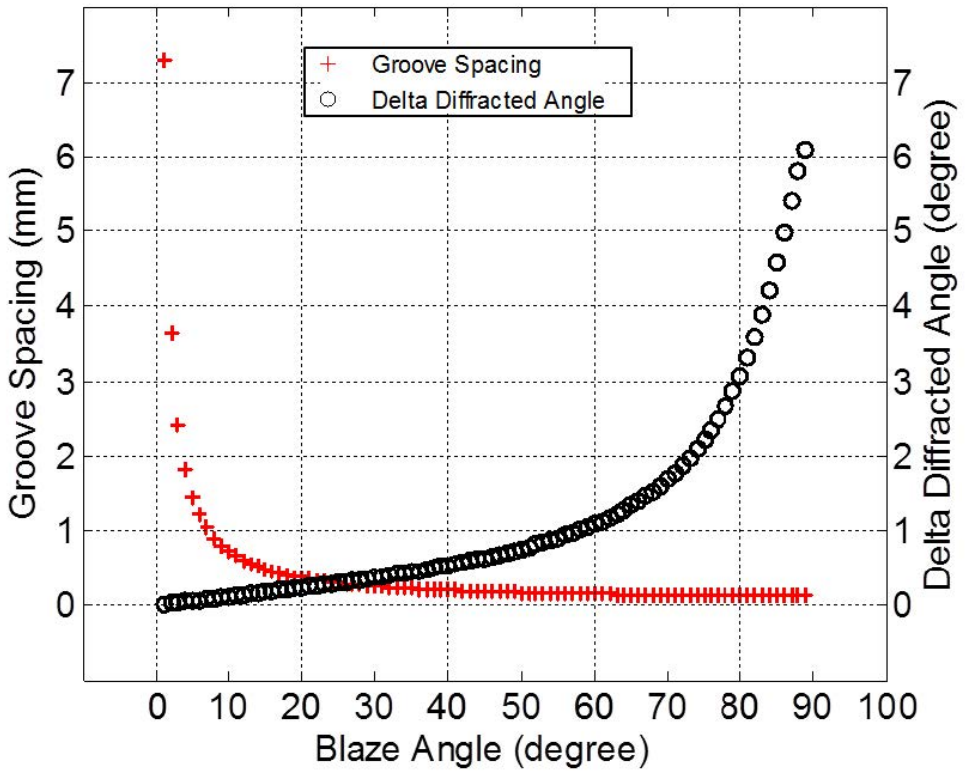

Figure 2.13: Dependency of scanning angle on groove spacing and blaze angle in a theoretical design using $\lambda_U = 1600$ nm.

tuning range differs slightly. Blazed gratings which have a large blaze angle are known as echelle gratings. In practice, echelle gratings provide more than one diffraction order for each wavelength. For beam steering purpose, in order to avoid interference from the next diffraction order of the same wavelength, only one diffraction order of the second grating is used.

2.5 Chapter conclusion

This chapter presented many scanning techniques for active and passive beam-steering, and gave a general overview of the vast variety of techniques for steering, underlying the steering capabilities and complexities for each technique. Then, a deeper look on the PRA of the BROWSE has been given. In the following chapters, a deeper look on the equipment used in the

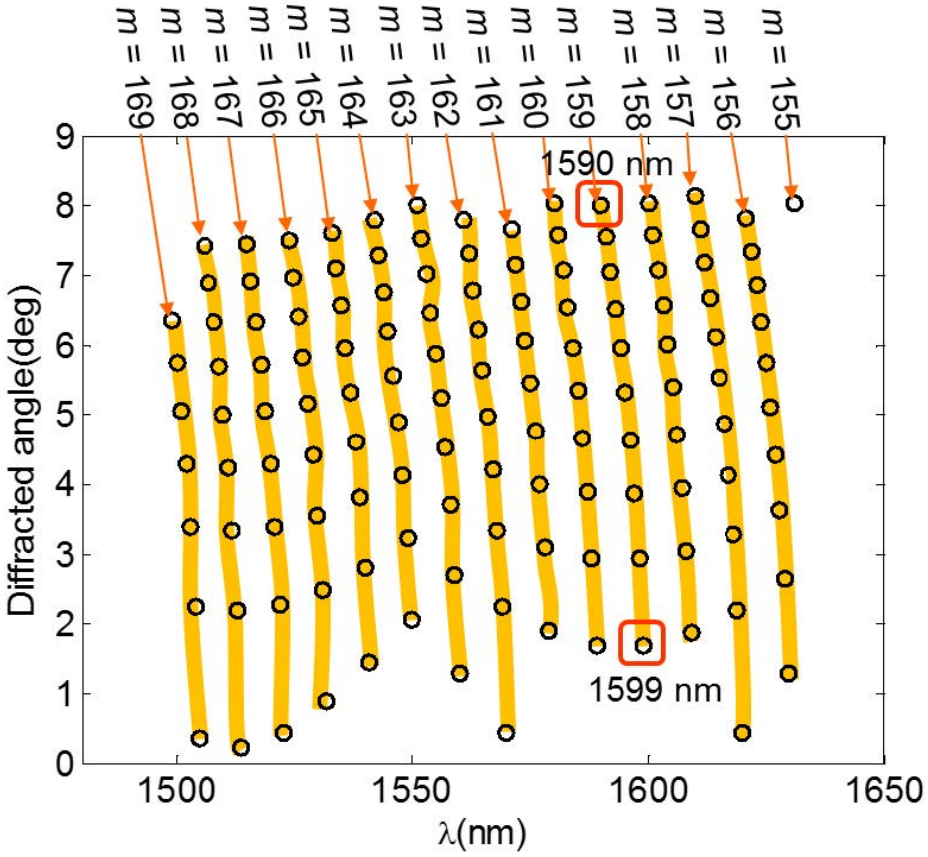

Figure 2.14: Diffraction angle versus wavelength tabulation for high dispersive grating.

setup will be given.

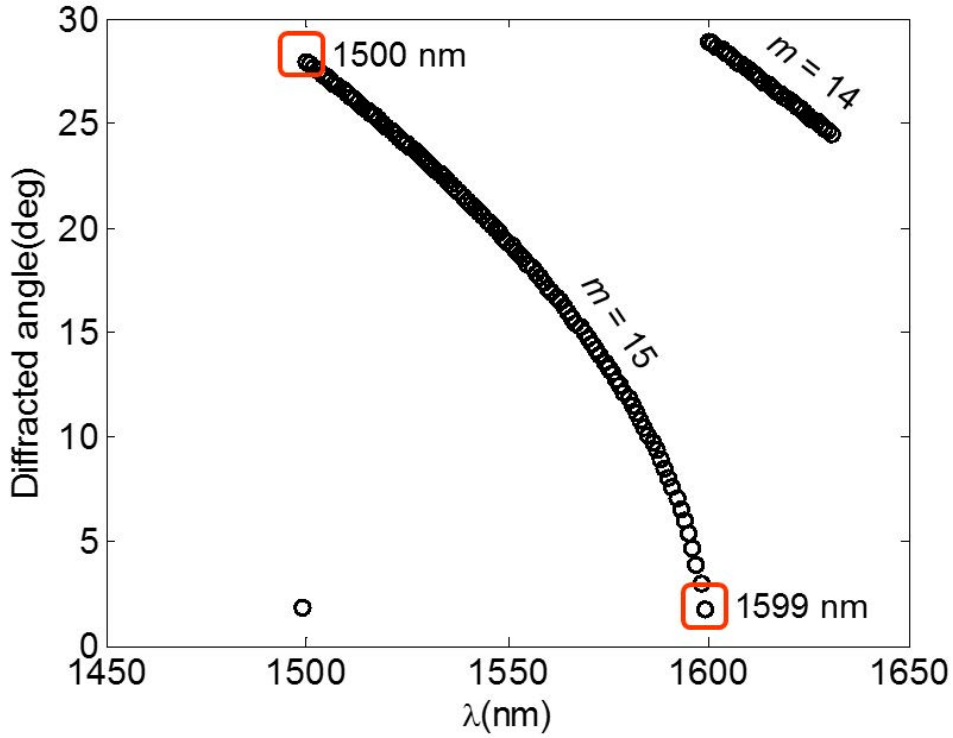

Figure 2.15: Diffraction angle versus wavelength tabulation for low dispersive grating.

Chapter 3

Setup description

In this chapter, a description of the freespace optical transmission system will be given. In general, the construction of a free-space optical system is similar to the construction of an optical fiber communication system, except for the transmission medium, which is free space. Fig. 3.1(b) shows a basic optical fiber communication system and Fig. 3.1(b) shows the basic optical free-space communication system.The fiber channel is affected by both attenuation and dispersion effects. On the other hand, indoor free-space channels also have losses but dispersion is negligible. The active components that make up the transmitter and receiver are essentially the same. The main components that are employed in the experimental testbed for this thesis include light sources, modulators, electrical and optical amplifiers and photodetectors. Data generation and data processing are carried out by instruments such as Arbitrary Waveform Generator (AWG), Pseudo Random Binary Sequence (PRBS) generator, Digital Phosphor Oscilloscope (DPO) and Bit Error Rate Tester (BERT).

3.1 Components for free-space transmission

The main components for an optical free space communication are a light source, electrical and optical amplifiers, modulators, gratings, collimators, and photodetectors. For a detailed setup description please refer to [90]. As a light source, a tunable laser with wavelength tuning range from 1505 nm to 1630 nm has been used. Mach-Zehnder modulators are mainly used for

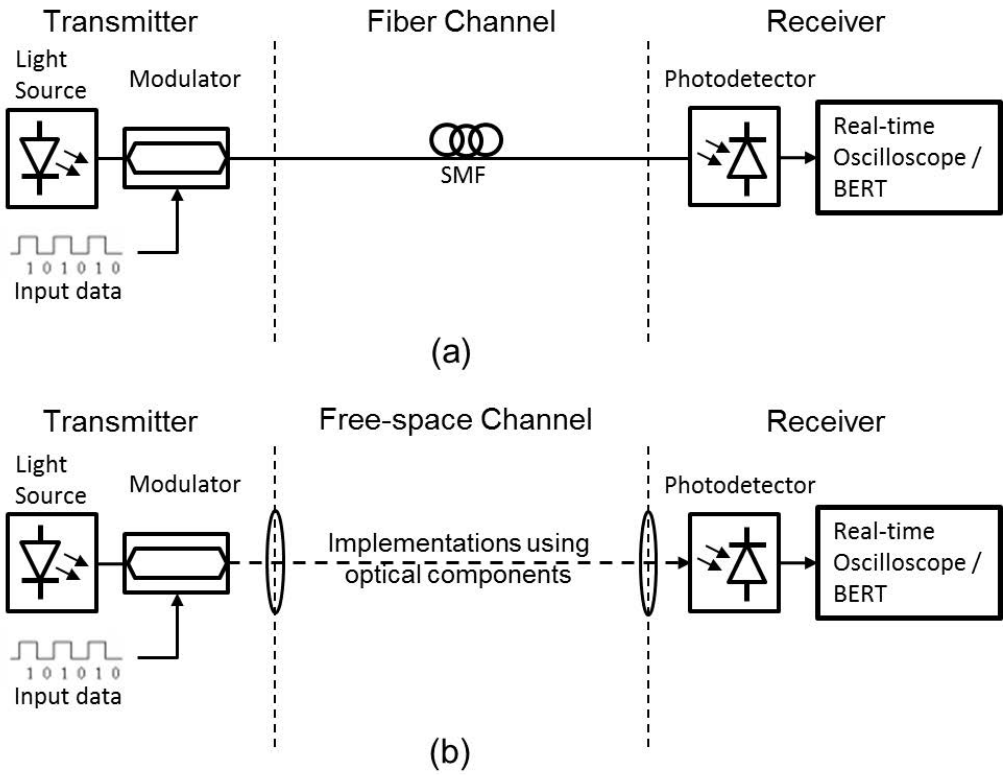

Figure 3.1: Optical fiber communication system versus free-space communication system.

this setup. The main problem for practical implementations is surely the collimator Full-Field of View (FFoV), because the one used in this setup is $FFoV = 0.034°$. For this reason, automatic receiver alignement robot have been used, and where that was not possible, hours of work were required to align the collimators. The photo diode used for receiving only power, hoever, has a much wider FFoV, in the order of few degrees. It is still not enough for real life applications, but it's enough to know where there is received power, especially for the sake of localization only.

3.2 Modulation formats

The modulation format used for most experiments is the On-Off-Keying (OOK)-Non-Return-to-Zero (NRZ), which is a binary non-return-to-zero modulation. NRZ differs from Return-to-Zero (RZ) which transitions to the '0'

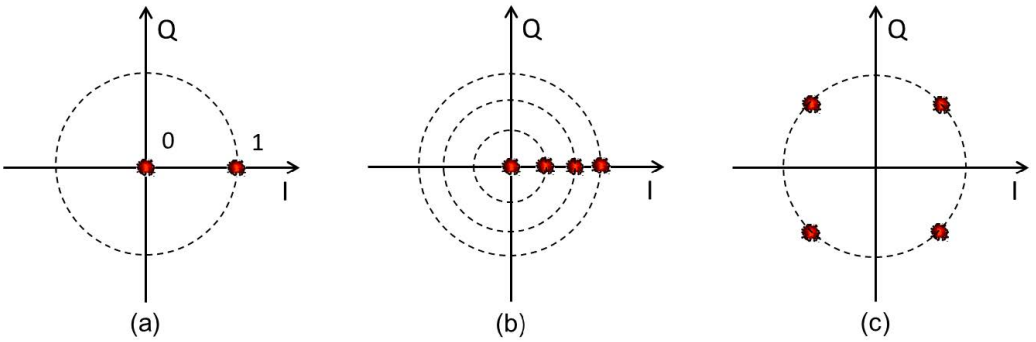

Figure 3.2: Example of constellation diagrams with I (in-phase or real) axis and Q (quadrature or imaginary) axis for (a) OOK, (b) 4-PAM and (c) 4-QAM.

level for each bit by which it provides self-clocking but at the expense of double the bandwidth. An on-off signal or unipolar signal in optical transmission is known as on-off-keying. We see that there are two levels, that is the 'on' (when there is light) and the 'off' (when there is no light) levels. When we transmit more than 1 bit/symbol, say 'n' bits, using amplitude modulation, we have 2^n-level modulation. N-PAM modulation is a multilevel signal, for e.g., a 4-level Pulse Amplitude Modulation (PAM) would mean a transmission of 2 bits/symbol. In fact, OOK is a 2-PAM system. OOK and PAM systems do not carry phase information, only amplitude information. Another coding method is the Quadrature Amplitude Modulation (QAM) modulation format which has two dimensional modulation. The optical carriers of the same frequency have a phase difference of 90° with each other (see Fig. 3.2).

The next modulation format is the Discrete Multitone (DMT) modulation, which is a variant of the Orthogonal Frequency Division Multiplexing (OFDM) technique and is widely used, for e.g., in copper-based Digital Subscriber Line (DSL) user access networks for high speed transmission. DMT is a baseband multicarrier and multiplexing modulation technique that by its so-called bit-loading function can allocate the number of bits per subcarrier while adapting to the Signal-to-Noise Ratio (SNR) in order to optimize channel capacity in a transmission link. A rate-adaptive bit-loading algorithm is utilized to maximize the data rate over the available system bandwidth while staying below the threshold of Forward Error Correction (FEC) at a Bit Er-

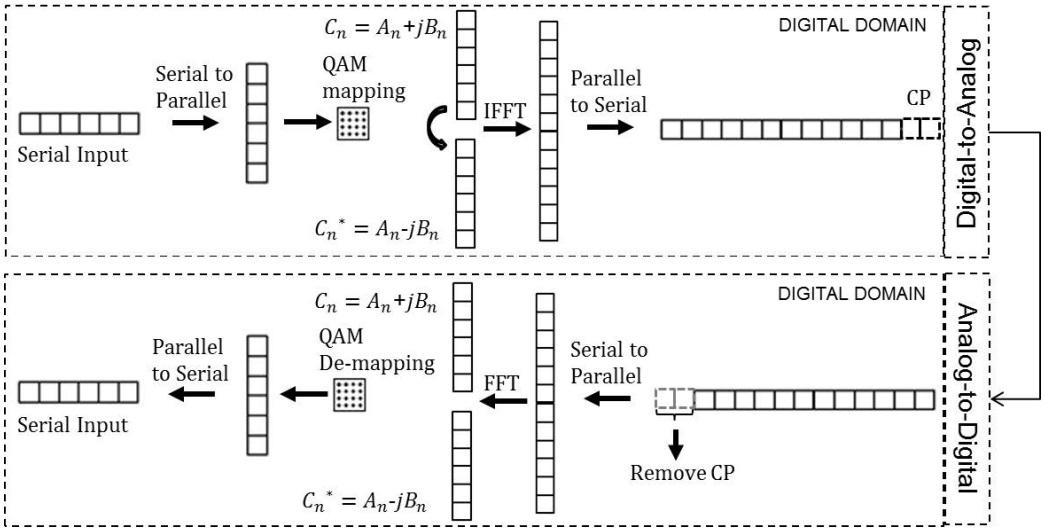

Figure 3.3: Discrete multitone modulation (DMT) operation blocks for transmitting and receiving DMT signals. Quadrature Amplitude Modulation (QAM), Cyclic Prefix (CP) [91].

ror Rate (BER) $\leqslant 2 \times 10^{-3}$. The operation of DMT transmit (modulation) and receive (demodulation) blocks in the digital domain is shown in Fig. 3.3. From the transmitting end, a stream of serial input data is subdivided into parallel streams and modulated with QAM mapping. The complex signal is then multiplied with its conjugate satisfying the Hermitian symmetry for real-valued Inverse Fast Fourier Transform (IFFT) output. IFFT is performed to place the complex values and their conjugates on different sub-carrier frequencies. The signal is then converted from parallel streams to a single serial high-speed stream for transmission. At the receiving end, Fast Fourier Transform (FFT) is performed to demodulate the signal and the BER is calculated. For a more extensive treatment on DMT modulation techniques, please refer to [91, 92].

3.3 Beam diameter

Since laser sources are used in this thesis we shall analyze the free-space beam using the well known Gaussian beam equations with the important parameters as shown in Fig. 3.4.

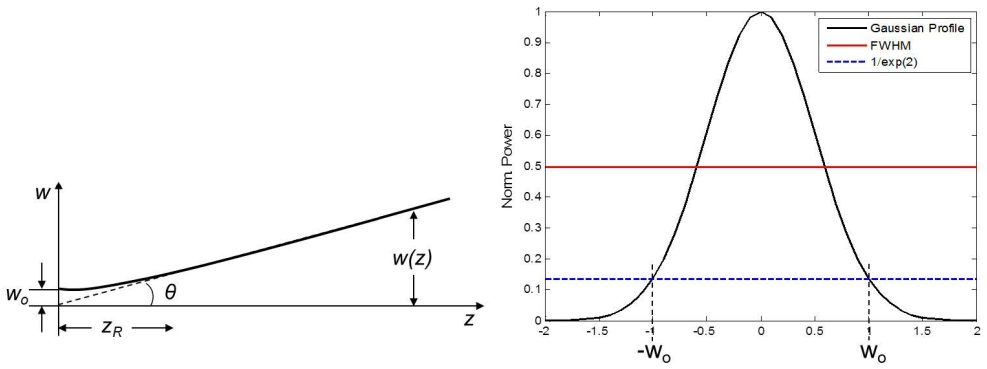

Figure 3.4: Profile of Gaussian beam which can be described using the parameters explained in the text. (a) Longitudinal and (b) Transversal power profile of the Gaussian beam amplitude, with a solid line indicating the full width at half maximum position and a dashed line indicating the $1/e^2$ position.

Laser beams are similar to plane waves but their intensity distributions are concentrated near the axis of propagation with a slightly curved phase fronts [93]. A field component, u, of the coherent light satisfies the wave equation:

$$\Delta^2 u + k^2 u = 0 \tag{3.1}$$

where $k = 2\pi/\lambda$ is the propagation constant in the medium, and

$$u = \Psi(x, y, z) \exp(-jkz) \tag{3.2}$$

where Ψ is a slowly varying complex function which represents characteristics such as non-uniform intensity distribution, expansion of the beam width with propagation distance, curvature of the phase front, etc. The fundamental Gaussian beam is given by H. Kogelnik and T. Li as [93]:

$$u(r, z) = \frac{w_o}{w} \exp\left[-j(kz - \Phi) - r^2\left(\frac{1}{w^2} + \frac{jk}{2R}\right)\right] \tag{3.3}$$

where $\Phi = \arctan(\lambda z/\pi w_o^2)$ and is known as the Guoy phase shift (See [93, 94] for the full derivation). The expression describes the behavior of the laser beam amplitude as a function of transversal coordinate, r, and axial coordinate, z. A commonly accepted definition is that the Gaussian beam waist is the smallest radius of the beam and is denoted as, w_o, (see Fig. 3.4)

where the beam intensity or power has fallen to $1/e^2$ of the peak. Sometimes the position at half peak is used and this is known as the Full Width Half Maximum (FWHM) width. It is impossible to have a perfectly collimated beam due to diffraction of light waves. The beam radius at z-position is given by:

$$w(z) = w_o\sqrt{1 + \left(\frac{z}{Z_R}\right)^2} \tag{3.4}$$

The radius of curvature at z-position is given by:

$$R(z) = z\left[1 + \left(\frac{Z_R}{z}\right)^2\right] \tag{3.5}$$

where Z_R, which is known as the Rayleigh range, is where the beam waist has increased by a factor of $\sqrt{2}$. The Rayleigh range can be calculated using:

$$Z_R = \frac{\pi w_o^2}{\lambda} \tag{3.6}$$

At far field ($z \gg Z_R$), the half-divergence angle, can be calculated using:

$$\theta = \sqrt{\frac{2\lambda}{\pi b}} = \frac{\lambda}{\pi Z_o} \tag{3.7}$$

where $b = 2Z_R$ which is the depth of focus.

3.4 Beam steering control and localization

The beam steering control of the system is incorporated in the Central Communication Controller (CCC). The Keysight tunable laser 81960A, which is able to tune up to 200 nm/s and with a wavelength tuning range from 1505 nm to 1630 nm, is employed. A lot of different techniques have been implemented for localization in the BROWSE project. The first idea was to make the user transmit a 60 GHz signal to the phased-array antenna at the Radio Access Point (RAP). Low-latency identification of the position and tracking of the movements of mobile devices is important. Results based on this technique were not satisfying, so a camera-based localization has been chosen. In Chapter 7 it will be carefully analyzed.

3.5 Chapter conclusion

In order to provide a smooth transition from the previous theoretical chapters, the practical issues regarding the implementation of optical free-space communication system are introduced in this chapter. The communication components which are used in the experimental demonstrations in the subsequent chapters are described. Important system design considerations such as the determination of the beam diameter, grating dispersion, and angular magnification are described. In this chapter, the important problem of the wide angle receiver has been encountered and showed its consequences. For this reason, in the next chapter a wide angle receiver will be presented and discussed.

Chapter 4

Wide Angle Receivers

We have presented measurements made with a fiber pigtailed collimator, Thorlabs TC18FC-1550 model, with a focal length of 18.36 mm and a full-angle divergence of 0.034°. The $1/e^2$ beam diameter is 3.33 mm at the focal plane. The collimator has a very limited Field of View (FoV), i.e. 0.034° theoretically. The transmitter's narrow FoV results in very precise measurement with reduced path loss as narrow beams could better concentrate the optical power within a small area compared to a wide beam. The narrow FoV at the receiver would mean less background light is captured since the FoV is very small and accepts only near parallel beam. This also avoids multipath distortion from beams coming from angles larger than the ones that can be received in the small FoV of the receiver. These results in less noise being captured, and thus, improve the Signal-to-Noise Ratio (SNR) of the signal. However, the alignment of such narrow FoV collimators is a tedious process and is definitely not feasible for practical implementation in a nomadic or mobile system due to the inherent long latency for alignment and user detection. Therefore, besides having a high coupling efficiency optical system, a wide angle optical receiver is desired.

4.1 Wide Angle properties

An important factor in light coupling, which we should take into consideration, is the acceptance, or étendue, $\acute{\varepsilon}$, of the optical system [95]. Étendue denotes the geometrical extent or spread of light. It is a product of the effective emitting or receiving area (A_{eff}), and the solid angle (Ω). The

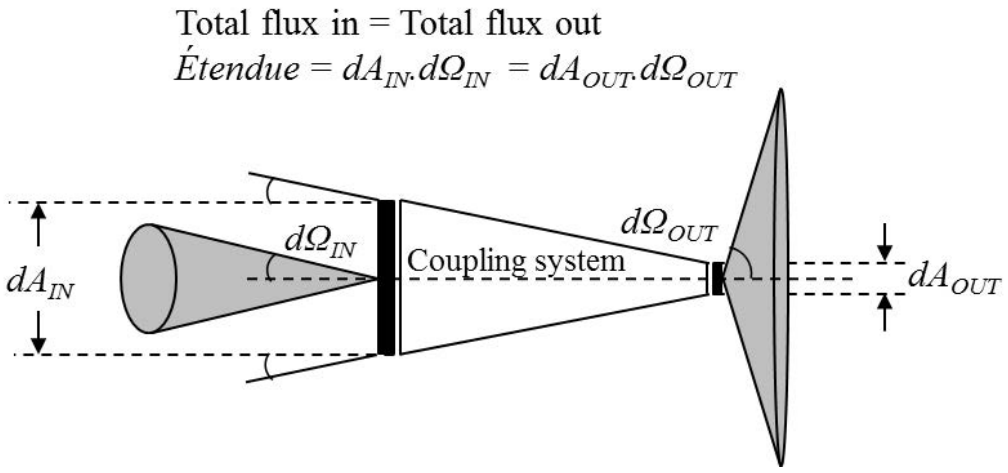

Figure 4.1: Conservation of étendue.

fundamental principal of étendue is the conservation of energy, or the conservation of the number of rays, in an optical system [96], as shown in Fig. 4.1. étendue is conserved as light travels through optical systems where it undergoes perfect reflections or refractions. The étendue of light can only increase due to scattering, but can never decrease. The étendue factor sets the fundamental limit for effective light coupling of the system. In order to get perfect coupling, the étendue of the emitter and receiver has to match. In an optical system, the component which has the lowest étendue sets the limit of the entire system. For example, light coming from a larger étendue source will only be partially accepted by the limiting component of the lowest étendue in the receiving optical system [97]. In the opposite case where the receiving optical system has a larger étendue than the source, almost all the light can be coupled into the optical system. The collected power or the radiant flux, F, is related to the étendue, $\acute{\varepsilon}$, and radiance, L^e, as the following:

$$L^e = \frac{dF}{dA_{eff} \cdot d\Omega} \tag{4.1}$$

$$dF = L^e \cdot dA_{eff} \cdot d\Omega = L^e \cdot d^2\varepsilon \tag{4.2}$$

where $dA_{eff} \cdot d\Omega$ determines the étendue, $dA_{eff} = dA\cos\theta$ and $d\Omega = \sin\theta d\theta d\phi$. Radiance is the radiant flux of a given infinitesimal surface in an infinitesimal solid angle around a given direction, divided by the product of effective area and solid angle [98]. We see that, at a constant radiance,

by having a larger étendue at the receiving optical system, more power can be collected. In a free-space optical transmission system which employs a fiber coupling sub-system at the receiver, the sub-system is limited by the étendue of the fiber. The small diameter and numerical aperture of the optical fiber determines the étendue factor. The étendue factor for a fiber can be determined as follows [97, 99]:

$$d^2\xi = dA_{eff} \cdot d\Omega \tag{4.3}$$

$$\xi = A \iint \cos\theta \sin\theta d\theta d\phi \tag{4.4}$$

$$= \pi A \sin^2\theta \tag{4.5}$$

where $\sin\theta$ is the angle corresponding to the numerical aperture of the fiber.

Whereas in a system which employs a photodetector together with an optical coupling sub-system with lenses and / or concentrators, the étendue is determined by the effective aperture (taking into consideration the aperture stop and field stop [98]) and the solid angle from which the light is accepted. The θ is then the angle corresponding to the angle of the half-field of view of the system.

Table 4.1: Table 8.1: Comparison of étendue limits for SMF [100], MMF [101, 102, 103], and photodetector based receiver [103]. θ_{half}: Half-field of view angle, Ω: Solid angle, d: diameter, A_{eff}: Effective detection area, $\acute{\varepsilon}$: étendue, SI: Stepindex, GI: Graded-index, SMF: Single mode fiber, MMF: Multimode fiber, PD: photodetector

Component	$\theta_{half}[^\circ]$	$\Omega[sr]$	$d[\mu m]$	$A_{eff}[mm^2]$	$\acute{\varepsilon}[mm^2 \cdot sr]$
SMF 1060XP	8.05	6.19×10^{-2}	9.5 ± 0.5	7.09×10^{-5}	4.4×10^{-6}
SMF 980HP	11.54	0.13	6.8 ± 0.5	3.63×10^{-5}	4.6×10^{-6}
GI-MMF GIF625	15.96	0.24	62.5 ± 2.5	3.07×10^{-3}	7.3×10^{-4}
SI-MMF FP1000ERT	30	0.84	1000 ± 15	7.85×10^{-1}	6.2×10^{-1}
New Focus 12 Ghz	80	5.19	25	4.91×10^{-4}	1.5×10^{-3}

Table 8.1 compares the étendue limit of two Single Mode Fibers (SMFs), two Multimode Fibers (MMFs) and a 12 GHz photodetector from New-

port/New Focus. The fibers are selected such that they have a large numerical aperture and / or large effective detection area. We observe that a reasonably large étendue can be achieved by using a step-index MMF. The half-field of view is modest and can be improved using an optical subsystem to increase the field of view of the free-space receiver. However, the effective detection area will have to be compromised due to the conservation of étendue. Another interesting component is the Newport/New Focus 12 GHz photodetector. The detection area is much smaller than that of the step-index MMF but it has the advantage of an inherently large field of view. Consider also that for a photodetector of a higher bandwidth, BW, the junction capacitance, C_j [104] has to be decreased as in the following relation:

$$BW = \frac{1}{2\pi R_{Load} C_j} \tag{4.6}$$

where R_{Load} is the load resistance. In a transmission system, the load resistance is typically 50 Ω. Correspondingly, the area of the photodetector has to decrease to provide a lower capacitance as in the following relation:

$$C_j = \frac{\varepsilon_s A}{w} \tag{4.7}$$

where ε_s is the permittivity of the semiconductor material, A is the diffusion layer area / detection area and w is the depletion layer width which depends on the carrier transit time and the carrier drift velocity [104].

As seen in the relations explained above, a challenge in employing high speed receivers is the small photodetector area. We can increase the effective area and field of view, and consequently the effective étendue, for example by employing an array of photodetectors.

The following are some techniques used to improve the receiving angles of the optical receivers. The techniques using (1) Compound parabolic concentrator [109] and (2) Angular magnifier in combination with an SLM [110], as shown in Fig. 4.2 and Fig. 4.3, respectively, are not inherently wide angle as they are limited by the étendue of the fiber which limits the product of aperture and field of view. Both systems require tracking and alignment to achieve wide angle operation. In (1), the coupling system has to be adjusted to align the beam to the fiber and in (2), the Spatial Light Modulator (SLM) is used as the alignment adjustment. Techniques (3) Angle diversity receiver [105] and (4) Hemispherical lens [106], as shown in Fig. 4.4 and Fig. 4.5, respectively, show photodetector based receivers which have a much larger

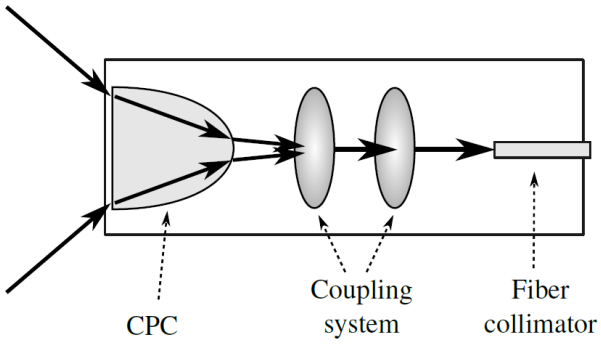

Figure 4.2: Free-space receiver using compound parabolic concentrator (CPC) with an FFoV of 90°, used together with coupling lenses [109].

field of view as their detection areas tend to be larger and their field of view is at least 90° theoretically. Technique (5) Fiber bundle arrays is another way of increasing the effective étendue of the system by using a lens array and fiber bundle, together with an alignment process. Each bundle is placed at the focal distance behind each microlens in the array and each bundle is composed of multimode fibers. The microlens array is controlled using piezoelectric transducer to translate the lens array as a whole. The reported FFoV is approximately 20° [108]. The design of such a receiver is shown in Fig. 4.6.

In this thesis a commercial ultra-wide angle lens, also known as the fish eye lens, of 180° meant for mobile phones is proposed. This is an existing clip-on lens which is commercially available in the market for mobile phones. Users can deploy it for communication in addition to the primary function of taking wide angle pictures.

The advantage of using such a wide angle lens is its ability to provide a wide field of view by bending light into a small area, as shown in Fig. 4.7. The figure shows the ability to achieve an FFoV of 200°. This lens model is an existing wide angle lens model provided by Zemax, which can be found in the 'samples' folder provided by Zemax OpticStudio 16 software (Default directory ../MyDocuments/Zemax/Sample/Sequential/Objectives). It is not in scale with the lens used in the experimental demonstration. The purpose the model is used is to show how the rays travel through a wide angle lens.

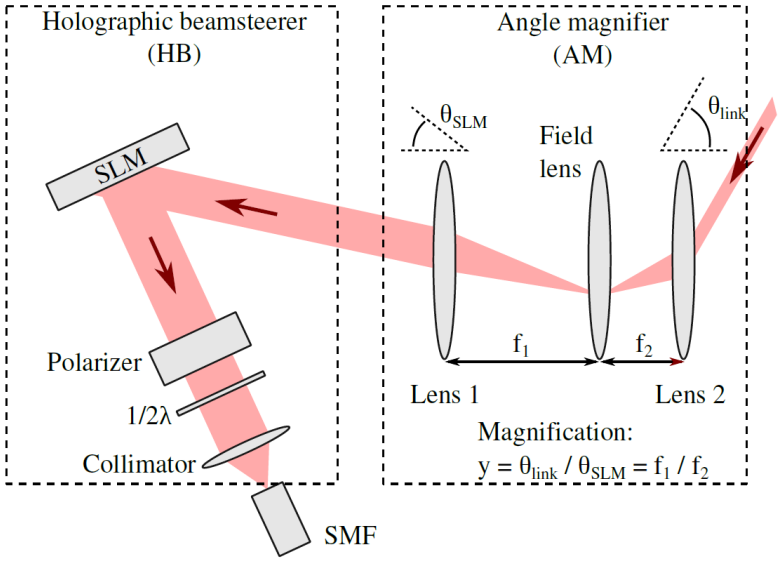

Figure 4.3: Receiver module which employed an angular magnifier in combination with a spatial light modulator to achieve up to 60° FFoV. The 'red arrow' shows the incoming beam from the access point. The beam then travels in the direction pointed by the red arrow towards the receiver through a lens collimating system and single mode fiber (SMF) [110].

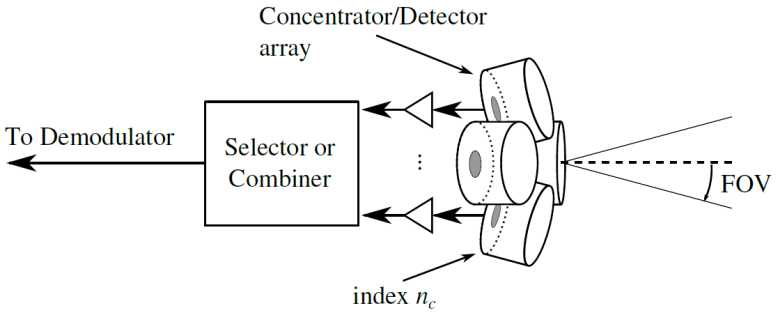

Figure 4.4: Angle diversity receiver with an array of four receiver elements ($8 \times 20°$ and $8 \times 31°$ configurations), in which each receiver optics consists of an optical filter, a concentrator and a photodetector [105].

From Fig. 4.7, we observe that a su°ciently large photodetector area, which can include an array of photodetectors, at the focal plane of the wide angle

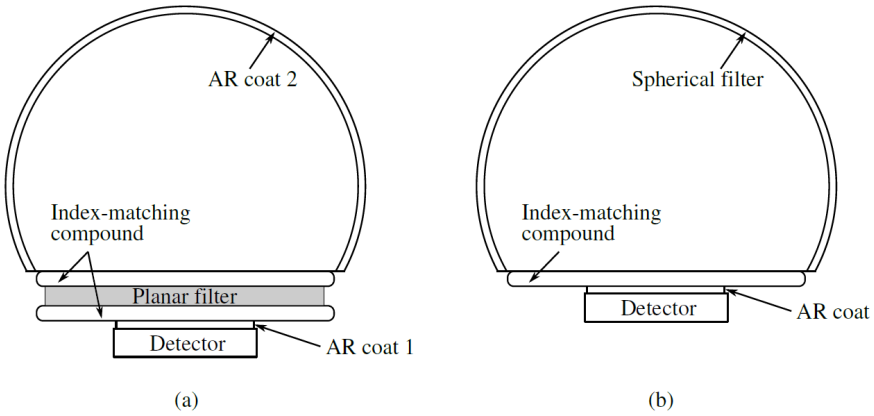

Figure 4.5: Receiver with hemispherical lens with: (a) a planar fillter and (b) a spherical filter, to reject ambient light [107]. This method has demonstrated an FFoV of up to 156° besides providing optical gain on a 1 cm2 detection area [106].

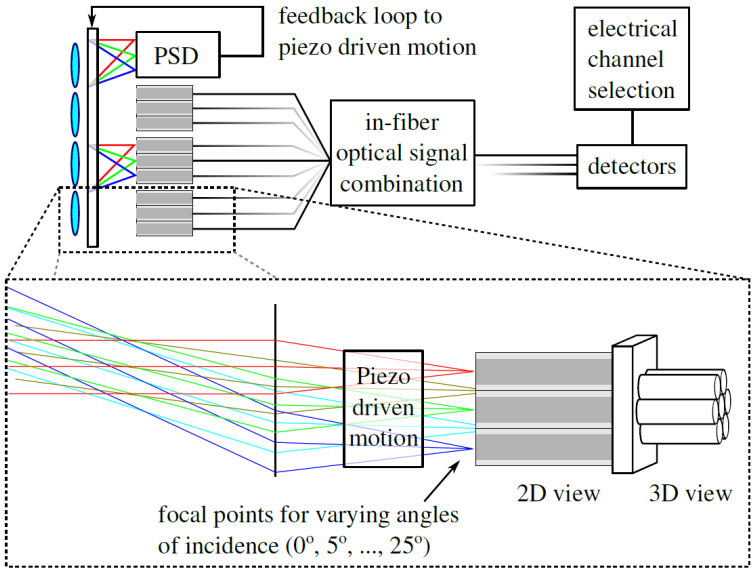

Figure 4.6: Conceptual design of lens array/fiber bundle wide field of view free-space receiver. A position sensing detector (PSD) provides a feedback to control the position of a microlens array such that an incident beam is always coupled into one fiber of a bundle behind the microlens array [108].

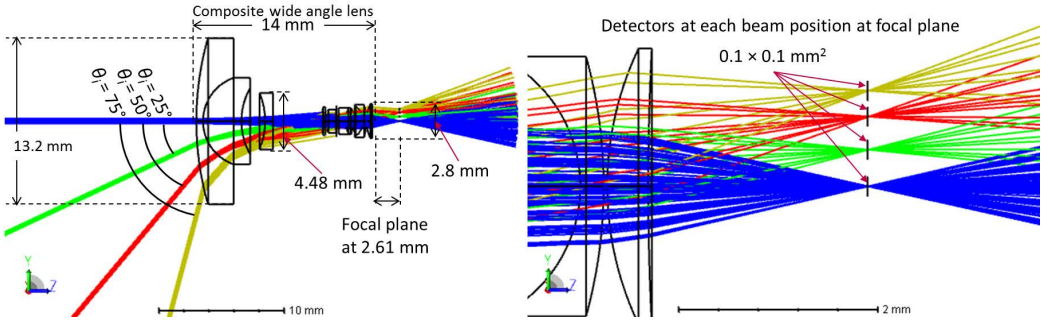

Figure 4.7: Principle of a wide angle lens. Simulation using a 200° ultra-wide angle lens / fisheye lens model from Zemax.

lens will be required. The figure shows that the lens, with dimensions shown in the picture, is able to couple light up to a half angle of 75° with a full photodetector diameter of about 2 mm. Assuming a 12 GHz photodetector [103] which has a diameter of 25 μm will be used, we will need 2 mm/25 μm $<$ 80 arrayed phtotodetectors (spacing between photodetectors are not included). This method could potentially allow a simple and low form-factor construction of receivers for mobile devices. Additionally, the arrayed photodetectors may allow simultaneous localization and tracking of a device by getting the information of the direction of the beam through the light intensity falling on the photodetector array. Another method of using the wide angle lens is by using an alignment system to align a fiber to the focused beam at the focal plane. This technique would be similar to the techniques shown in Fig. 4.6.

4.2 Results and discussion

Fig. 4.8 shows the measurement results as the angle of incidence of the beam is increasing. Observe that the Full Width Half Maximum (FWHM) of the curve is at approximately 40°, which corresponds to a FFoV of 80°. This FFoV is limited by the effective area of the collimator aperture.

In summary, this is a very simple idea and technique using an existing commercially available lens. Other lenses which are available commercially for mobile phones can also be potential solutions for wide angle light coupling. The required effective photoreceiver aperture area and the appropriate beam size are interdependent. A large beam size will require a larger effective

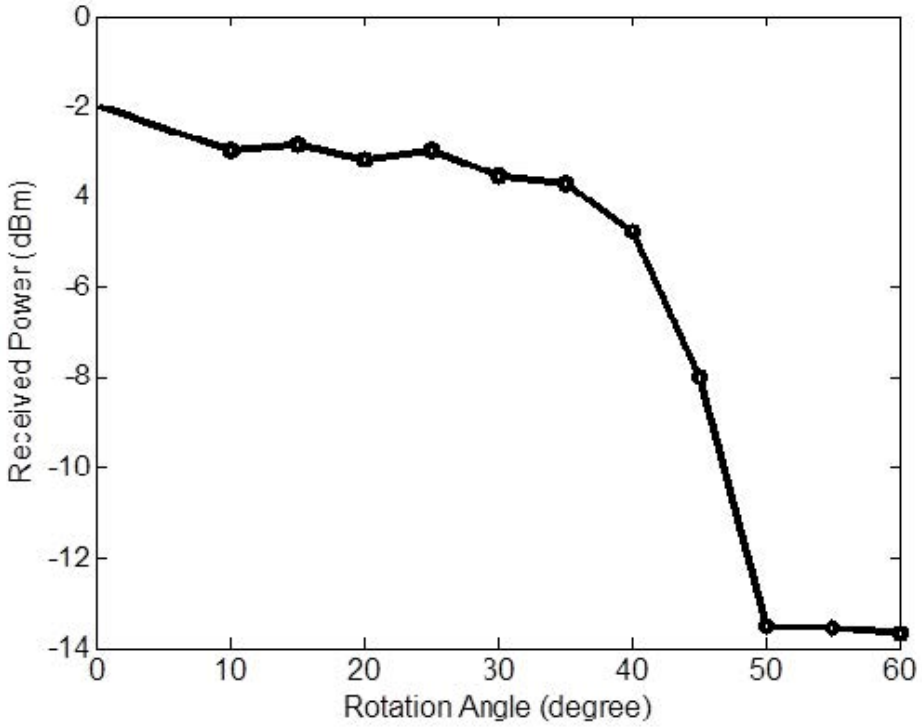

Figure 4.8: Measured coupled light at different incidence angle.

photoreceiver aperture area in order to guarantee adequate received optical power for data transmission. In a more advanced approach, receivers can be made from an array of photodetectors. Another alternative could be to use an array of micro mirrors to focus the beams into an array of fibers but this may result in a bulky construction [108].

A guide for the relation between the effective detector size needed versus the beam size has been reported in A.M.J. Koonen at al. [84]. The assumption was that the Pencil Radiating Antenna (PRA) covers an area of $L \times L$ with a 2D tabulation of spots with a beam diameter of D_{beam}, as shown in Fig. 4.9.

The number of scanning steps needed is, $N = (L/D_{beam})^2$. With a tuning range of $\Delta\lambda$, the tuning step size will be $\delta\lambda = \Delta\lambda/N = \Delta\lambda \times (D_{beam}/L)^2$. The lower bound for the beam diameter is given by $D_{beam} > L\sqrt{\delta\lambda_{min}/\Delta\lambda}$. The receiver aperture has a diameter of D_{rx} and the PRA is fixed in the middle of the ceiling of height, H. We assume that the intensity of the beam falling across the receiver diameter is uniform, and the minimum power received in

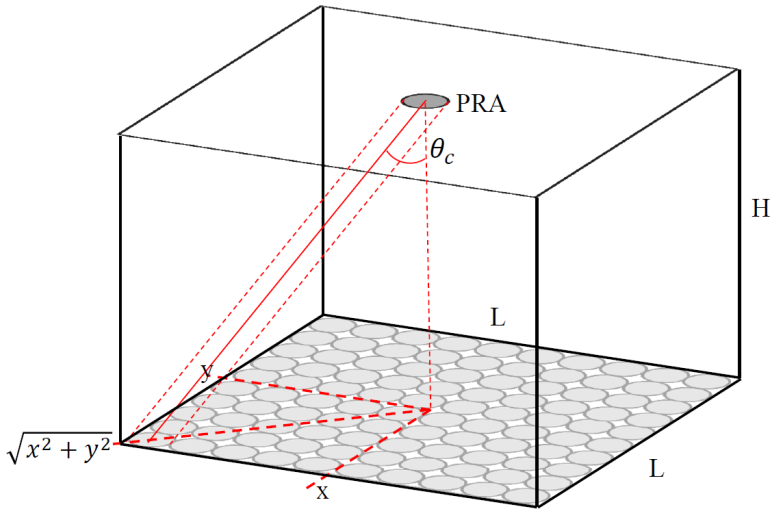

Figure 4.9: Scanning of a room with optical beams.

the elliptical spot in the corner of the room is given by:

$$P_{rx_{min}} = P_{beam} \cos\theta_c \frac{A_{rx}}{A_{spot}} \tag{4.8}$$

$$= \frac{P_{\text{beam}} \left(\frac{D_{rx}}{D_{\text{beam}}}\right)^2}{1 + \frac{L^2}{2H^2}} \tag{4.9}$$

which implicitly sets the upper bound to the beam diameter in order to guarantee an adequate minimum received power level. It is assumed here that the received power is not restricted by the field of view of the receiver. This approximation holds when the received light is incident directly on the active area of the photodetector. Intermediate optics such as a Compound Parabolic Concentrator (CPC) or condensor lens may yield a larger effective detection area, D_{rx} but due to the conservation of étendue, also restrict the field of view.

Fig. 4.10 shows how D_{beam} can be determined with the corresponding tuning step size and minimum receiver sensitivity. The calculation was made for a coverage area of 1.5×1.5 m^2, a height 2.5 m between the access point and the user terminal, a free-space beam power Pbeam of 10 mW (10 dBm) and an effective receiver aperture diameter, D_{rx} of 1 mm or D_{rx} of 10 mm [84]. As we can see from Fig. 4.10, a photoreceiver aperture area of 10 mm

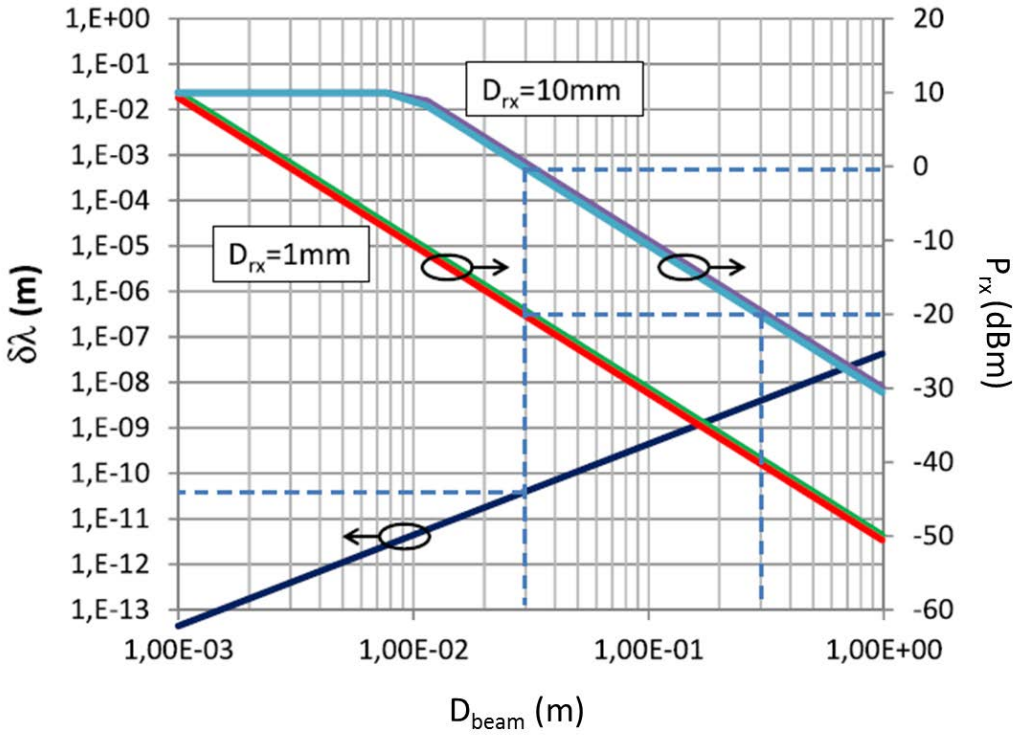

Figure 4.10: Corresponding beam diameter, D_{beam}, due to tuning step,$\delta\lambda$ and effective photoreceiver aperture diameter, D_{rx}, to yield the corresponding received optical power, P_{rx} [84].

can couple adequate received optical power of -20 dBm for data transmission of near error-free 10 Gbps On-Off-Keying (OOK)-Non-Return-to-Zero (NRZ) signal from a beam with a diameter of 30 cm. In our line-by-line 2D scanning techniques, $M = L/D_{beam}$ lines need to be scanned to completely cover an area of $L \times L$. Each line corresponds to passing through one Free Spectral Range (FSR) of the highly dispersive grating.

Chapter 5

Beam steering - System design and experiments

A discussion on the theoretical principles of gratings for optical free-space transmission will be made. It will start from basic principles in the 1 dimensional case, later expanded to the more general 2D case. A 2D beam steering with arrayed waveguide grating will be discussed in the end, as this is the technique used in the setup.

5.1 Beam diffraction for 1D beam steering

The echelle grating that has been employed in this experiment is a Thorlabs GE2550-0875 model. The grating has 79 grooves/mm, a blaze angle, θ_B of 75° at a blaze wavelength of 25 μm and a linear dispersion of 3.25 nm/mrad. The size of the grating is 25 mm × 50 mm × 9.5 mm. The grooves are parallel to the shorter dimension.

The map of the diffracted beam of $\lambda = 1558.98$ nm, at different grating diffraction orders, is shown in Fig. 5.1 for a free-space distance of 2.5 m (assuming the height of the Pencil Radiating Antenna (PRA) is 2.5 m from the plane of interest). These positions can be calculated using the grating equation (2.8):

$$m\lambda = d\left(n_1 \sin\theta_i + n_2 \sin\theta_m\right) \tag{5.1}$$

By rearranging the grating equation, we have:

$$\theta_m = \arcsin\left[\frac{1}{n_2}\left(\frac{m\lambda}{d} - n_1 \sin\theta_i\right)\right] \tag{5.2}$$

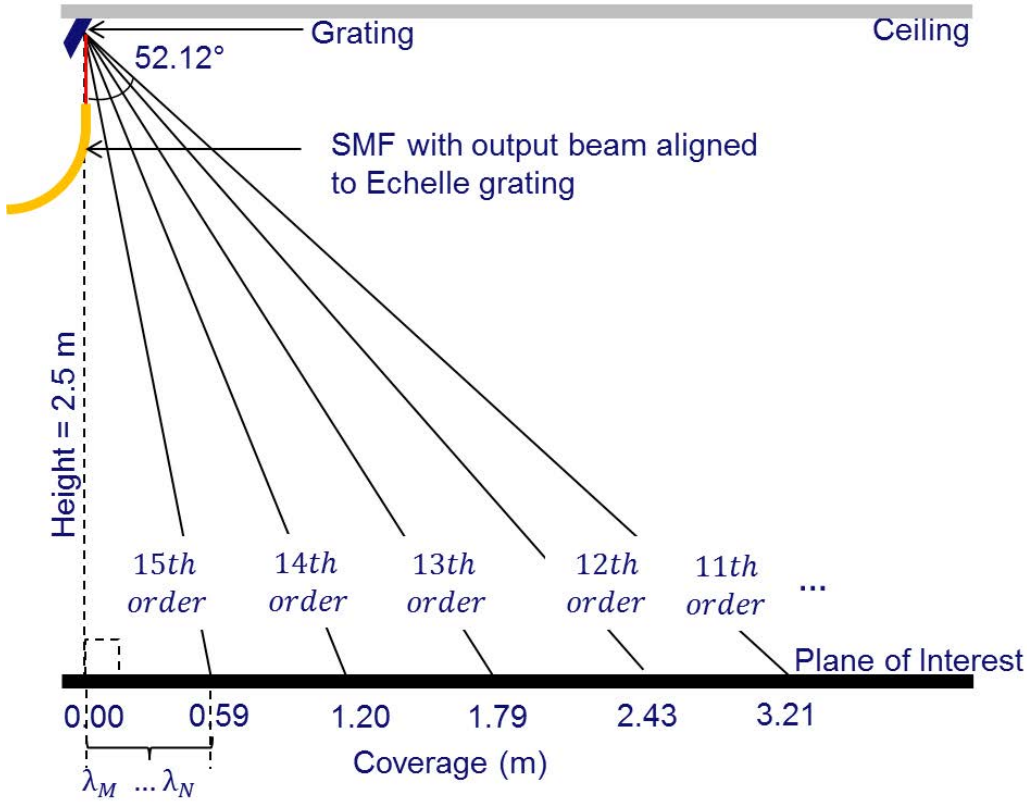

Figure 5.1: Map of diffracted beams at several grating orders for 1D beam steering. The wavelength employed is 1558.98 nm. The distance between the grating module to the plane of interest (where the devices are assumed to be) is taken to be 2.5 m [111].

Since a reflection blazed grating is used, the refractive indices $n1$ and $n2$ are equal to 1.

$$\theta_m = \arcsin\left[\left(\frac{m\lambda}{d} - \sin\theta_i\right)\right] \tag{5.3}$$

In a Littrow configuration, the incidence angle, θ_i is equal to θ_B, so, θ_i is constant at 75°, d is the period of the grating, which is equal to 1 mm/79 grooves, therefore 12.6582 μm, and with λ = 1558:98 nm, the order can be calculated using the Littrow equation (2.12):

$$m = \frac{2d\sin\theta_m}{\lambda} \tag{5.4}$$

$$m = \frac{2\left(12.6582\times10^{-6}\right)\sin 75^\circ}{1558.98\times10^{-9}} = 15.69 \approx 15 \tag{5.5}$$

We can finally calculate the position of each beam by using:

$$\theta_m = \arcsin\left[\left(\frac{m\lambda}{d} - \sin\theta_i\right)\right] \tag{5.6}$$

The Littrow angle of 75° is set to be the normal to the plane of interest, in this case, the plane is at distance of 2.5 m away. The first angular position of the diffracted beam of wavelength, $\lambda = 1558.98$ nm is:

$$\theta_{m1} = \arcsin\left[\left(\frac{15\,(1558.98\times10^{-9})}{12.6582\times10^{-6}} - \sin 75^\circ\right)\right] = 61.82^\circ \tag{5.7}$$

The delta angle between the normal at 75° and θ_{m1} is then $75^\circ - 61.82^\circ = 13.18^\circ$. The position of the beam at θ_{m1} at 2.5 m distance away from the normal is 2.5 m$\times \tan 13.18^\circ$ =0.59 m.

Only spectral orders where $|m\lambda/d| < 2$ can exist. Therefore, with a constant λ and d, only the orders lower than $m = 15$ can exist. Therefore, we calculate the next position for order, $m = 14$. Correspondingly, the next angular position of the diffracted beam of wavelength, $\lambda = 1558.98$ nm is:

$$\theta_{m2} = \arcsin\left[\left(\frac{14\,(1558.98\times10^{-9})}{12.6582\times10^{-6}} - \sin 75^\circ\right)\right] = 49.32^\circ \tag{5.8}$$

The delta angle between the normal at 75° and θ_{m2} is then $75^\circ - 49.32^\circ = 25.68^\circ$. The position of the beam at θ_{m2} at 2.5 m distance away from the normal is 2.5 m$\times \tan 25.68^\circ = 1.20$ m.

The next angular position of the diffracted beam of wavelength, $\lambda = 1558.98$ nm, at m=13, is:

$$\theta_{m2} = \arcsin\left[\left(\frac{13\,(1558.98\times10^{-9})}{12.6582\times10^{-6}} - \sin 75^\circ\right)\right] = 39.43^\circ \tag{5.9}$$

The delta angle between the normal at 75° and θ_{m1} is then $75^\circ - 39.43^\circ = 35.57^\circ$. The position of the beam at θ_{m3} at 2.5 m distance away from the beam normal to the plane of interest is 2.5 m $\times \tan 35.57^\circ$ =1.79 m.

Similarly, for the 4th and 5th orders, the angular positions are at 30.80° and 22.88° away from the normal and at a distance of 2.5 m away, the beams are directed to positions, 2.43 m and 3.21 m, respectively.

To further illustrate 1D beam steering using different wavelengths, the beam position versus wavelength map is calculated, as shown in Fig. 5.2.

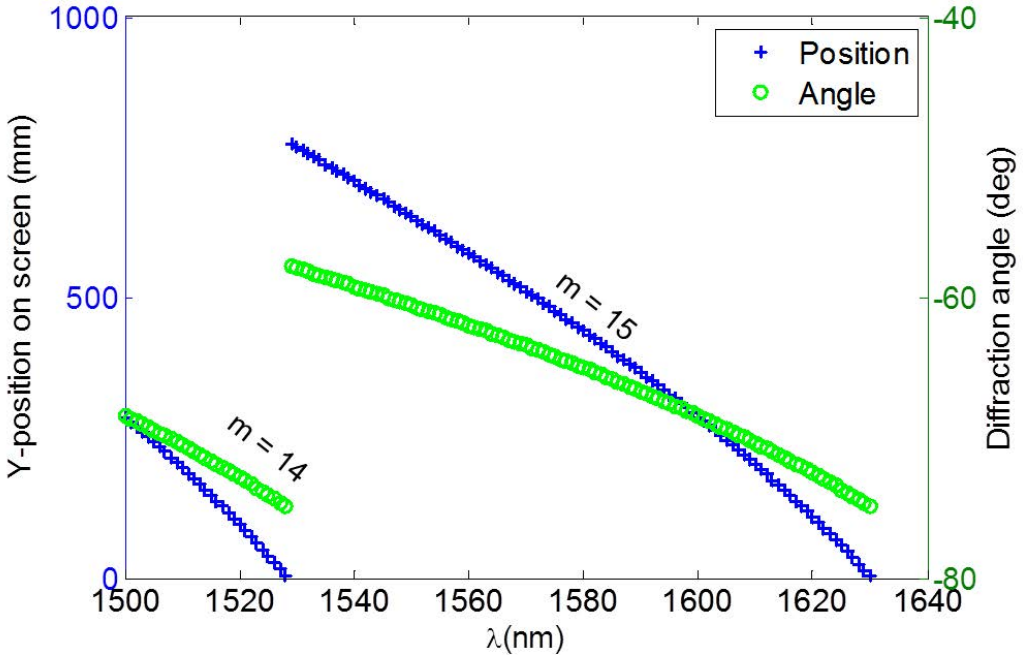

Figure 5.2: Diffraction angle and spatial distribution for a transmission distance of 2.5 m between the grating and the screen, with corresponding maximum steering angle of 17.16° by using diffraction order m = 15 for 1D beamsteering [112]. By steering the wavelength from 1529 nm to 1630 nm, we achieve a steered distance of 772 mm.

First, we look for the diffraction order of the corresponding wavelength by rearranging the Littrow equation (2.12) to:

$$m = \frac{2d \sin \theta_m}{\lambda} \tag{5.10}$$

Afterwards, the corresponding diffraction angles when the wavelength is changed can be obtained using:

$$\theta_m = \arcsin \left[\left(\frac{m\lambda}{d} - \sin \theta_i \right) \right] \tag{5.11}$$

By steering the wavelength from 1529 nm to 1630 nm at diffraction order, m = 15, we achieve a steered distance of 772 mm.

5.1.1 Channel bandwidth

The spectral response profile of a system has a major impact on the bandwidth of the overall system, next to the bandwidth of the receiver. The bandpass is determined at the Full Width Half Maximum (FWHM) of the normalized power or intensity curve.To measure the spectral bandwidth of the steering module we used the Optical Spectrum Analyzer (OSA) to capture the Amplified Spontaneous Emission (ASE) spectrum of an Erbium-Doped Fiber Amplifier (EDFA) whereby only a wavelength interval is captured by the coupling lens. The spectral bandwidth, $\Delta\lambda$, can be determined from the optical spectrum, and the bandwidth in frequency, $\Delta\nu$ can be obtained using:

$$\Delta\nu = \frac{c\Delta\lambda}{\lambda^2} \tag{5.12}$$

A spectral bandwidth measurement was carried out by transmitting ASE wideband signal originating from an EDFA toward an echelle grating (Thorlabs GE2550-0875) which has 79 grooves/mm and a blaze angle of 75°. The receiver was placed at 1 m distance and the received beam is coupled into the optical input port of an OSA. The measured spectral bandwidth, as shown in Fig. 5.3, is 0.17 nm at FWHM which by using Equation (5.12), we get the corresponding bandwidth of 21.27 Gigahertz (GHz) in frequency.

5.1.2 1D wavelength beam steering

A longer free-space transmission distance of 2.5 m, and data rates of up to 10 Gbps using the OOK-NRZ modulation format [112] has been performed. Error-free links beam-steered over a total wavelength range of 130 nm, with steering angle of 17.16°, have been achieved. The echelle grating of 79 grooves/mm with a blaze angle of 75° is used. However, the dependency on polarization is more evident as we work away from the blaze wavelength. The passive grating shows dependency on polarization at different wavelengths. Therefore, a polarization controller is needed to adjust the polarization of light before the beam hits the echelle grating. Note that different gratings have different polarization characteristics. The link performance, represented by the BER values versus the receiver sensitivity, is plotted in Fig. 5.4. The different links show a consistent overlap with the Back-to-Back (BtB) measurements at different data rates. The power penalties are within 1 dB with

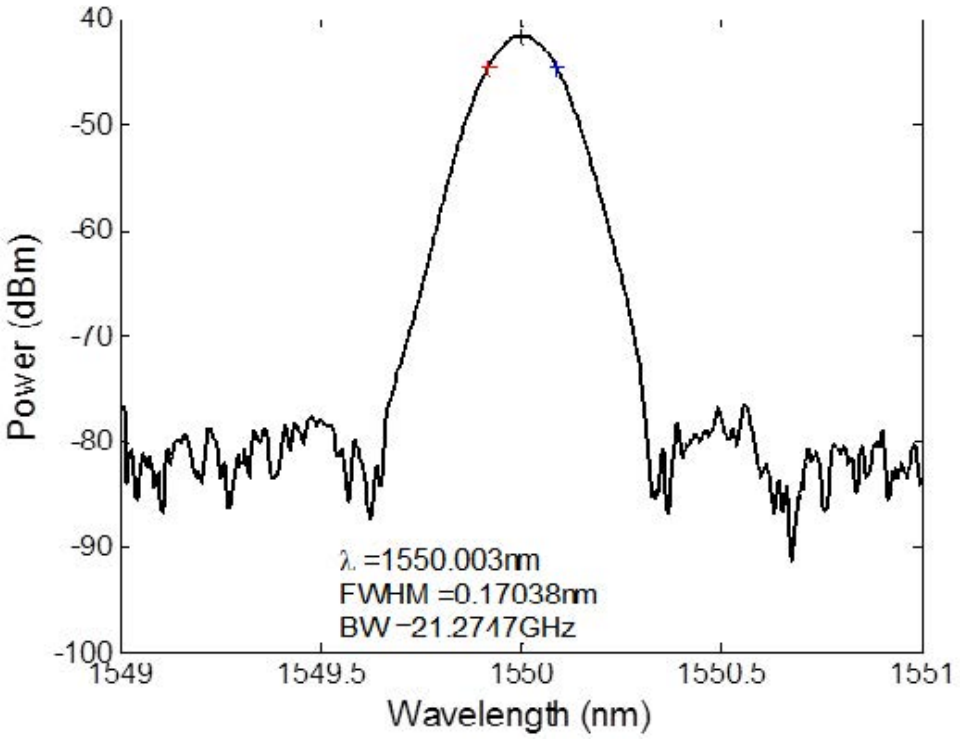

Figure 5.3: Spectral response curve of an echelle grating (Thorlabs GE2550-0875) which has 79 grooves/mm and a blaze angle of 75° used together with a triplet lens collimator from Thorlabs (TC18FC-1550) with a focal length of 18.36 mm, an opening aperture of 10 mm, and a full-angle divergence of 0.034°. The spectral response was measured using an optical spectrum analyzer with a resolution of 0.01 nm, at a transmission distance of 1 m.

reference to the BtB measurement. The BtB receiver sensitivity at BER of 1×10^{-9} is found to be at -17 dBm, -20.2 dBm, -20.6 dBm and -20.7 dBm for 10 Gbps, 5 Gbps, 2.5 Gbps and 1.25 Gbps, respectively. It can be observed from the results that the quality of the link stays as good as in BtB transmission and has negligible dispersion. The position where the Rx collimator is placed, is independent of distance as long as there is sufficient transmission power. This is because with the Thorlabs TC18FC-1550 collimator, the beam's full-angle divergence (0.034°) is small, resulting in a diverged beam size which is still smaller than the aperture of the Rx collimator at a distance away. Accordingly, the coupling efficiency is specified to be more than 90% for a separation distance, between Tx collimator and Rx collimator, of 2.5 m [113].

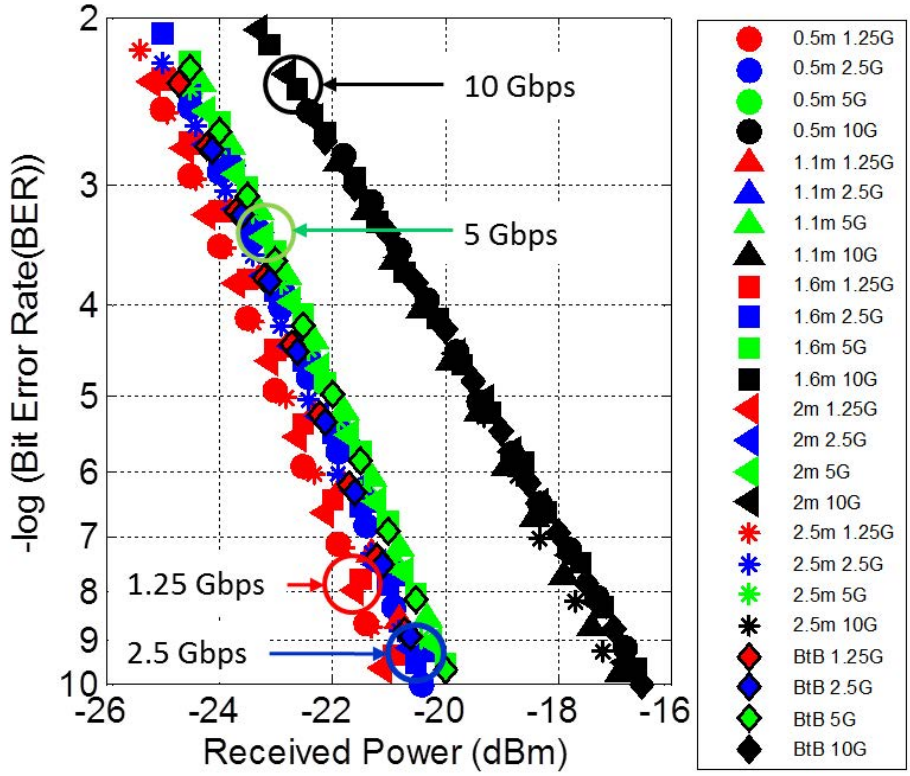

Figure 5.4: Link performance versus received power at 1.25 Gbps, 2.5 Gbps, 5 Gbps and 10 Gbps. The different colored notations refer to different data rates while the different symbol shape refer to different transmission length.

5.1.3 Capacity maximization using DMT modulation

After the positive performance evaluation of the OOK-NRZ data transmission using diffraction gratings, Discrete Multitone (DMT) modulation format is used to further maximize the capacity of the system which is bandwidth-limited to 10 GHz to limit the cost of components.

Fig. 5.5 shows a compact experimental setup for the performance measurement of multiple diffracted links for a distance of over 2.5 m using the DMT modulation format. The optical transmitter is a directly-modulated DFB laser with 10 GHz bandwidth. The experiment has successfully demonstrated a transmission of a freespace optical signal over more than 2.5 m, with an aggregate bit rate of 36.7 Gbps and 36.5 Gbps, at λ=1549.14 nm and λ=1550.14 nm, respectively. The averaged BER is $\leq 2 \times 10^{-3}$, which

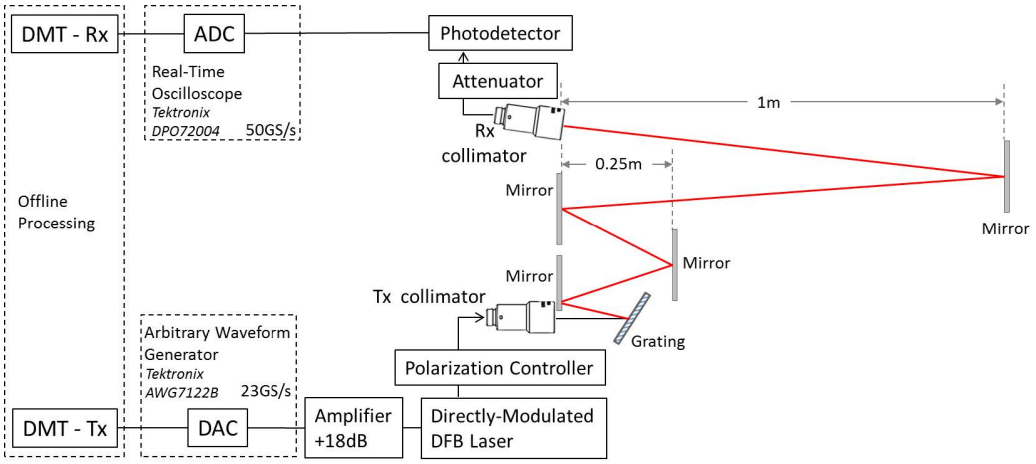

Figure 5.5: Compact experimental setup for diffracted link measurements with an effective distance of more than 2.5 m. Discrete Multitone (DMT), Digital-to-Analog Converter (DAC), Distributed Feedback (DFB), Transmitter (Tx), Receiver (Rx), Analog-to-Digital Converter (ADC).

by using standard 7% Forward Error Correction (FEC), will be reduced to BER $< 10^{-12}$. After the deduction of DMT transmission overhead (cyclic prefix, preambles and 7% FEC) the net transmission bit rates are 32.8 Gbps and 32.6 Gbps, respectively.

At a separation of $\Delta\lambda = 1$ nm between the wavelengths, the lateral distance difference (at the Rx plane) between both wavelengths is equal to 6.4 mm with angular difference of 0.1379°. Therefore, the first order diffraction link of $\lambda = 1549.14$ nm is positioned at 0.6495 m from the beam center at an angle of 14.564° and correspondingly, the first order diffraction link of $\lambda = 1550.14$nm is positioned at 0.6431 m from the beam center at an angle of 14.4261°. Fig. 5.6 presents the Signal-to-Noise Ratio (SNR), bit-loading and BER for the 512 subcarriers used in the DMT signal modulation, with a frequency range of up to 11.5 GHz, measured for both wavelengths. Up to 128-QAM has been utilized. It can be observed that not all subcarriers achieved a BER $\leq 2 \times 10^{-3}$ but the overall BER is still within the FEC limit for error-free transmission (note that in DMT transmission, the signal is not demodulated per subcarrier but as an entire frame). The constellation diagrams for up to 128-QAM are clearly distinguishable.

An infrared-based indoor OWC system employing a passive diffraction grating for beam steering has been demonstrated at a record capacity. The

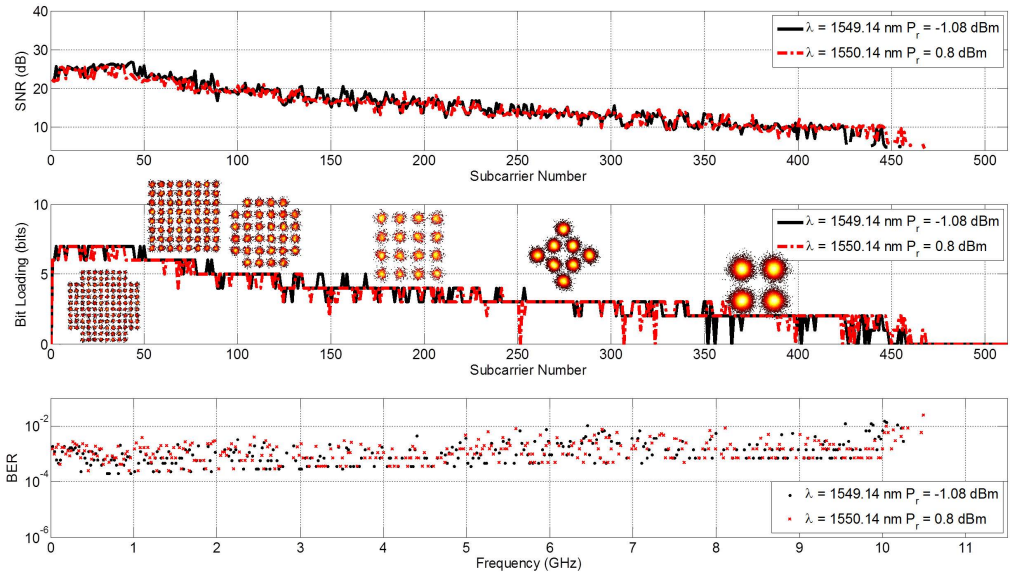

Figure 5.6: SNR, bit-loading and BER for each subcarrier for $\lambda = 1549.14$ nm and $\lambda = 1550{:}14$ nm.

system achieved an aggregate capacity of 36.7 Gbps, using spectrally efficient and robust DMT modulation, with over more than 2.5 m transmission distance. DMT modulation with bit- and power-loading algorithm was applied in the experiment to compensate for power fluctuations and to increase the frequency utilization efficiency simultaneously.

5.2 Beam diffraction for 2D beam steering

After the proof-of-principle evaluation for one-dimensional (1D) beam steering, we shall investigate the cascading of gratings to implement a two-dimensional (2D) passive beam-steering module in a bandwidth-limited optical wireless system [114]. No local control at the steering module is needed. In order to have a 2D area coverage and a scanning functionality as proposed in this work, two gratings have to be orthogonally cascaded to each other [85]. The idea is that the first grating should have a multiple times smaller Free Spectral Range (FSR) than the second grating.A cascade of a reflection grating and a transmission grating will be investigated. Figure 6.2 shows the 2D distribution of diffracted beams resulting from the module used. From Fig. 5.7, we can see 7 scan lines within an angular coverage of $12.15° \times 5.62°$

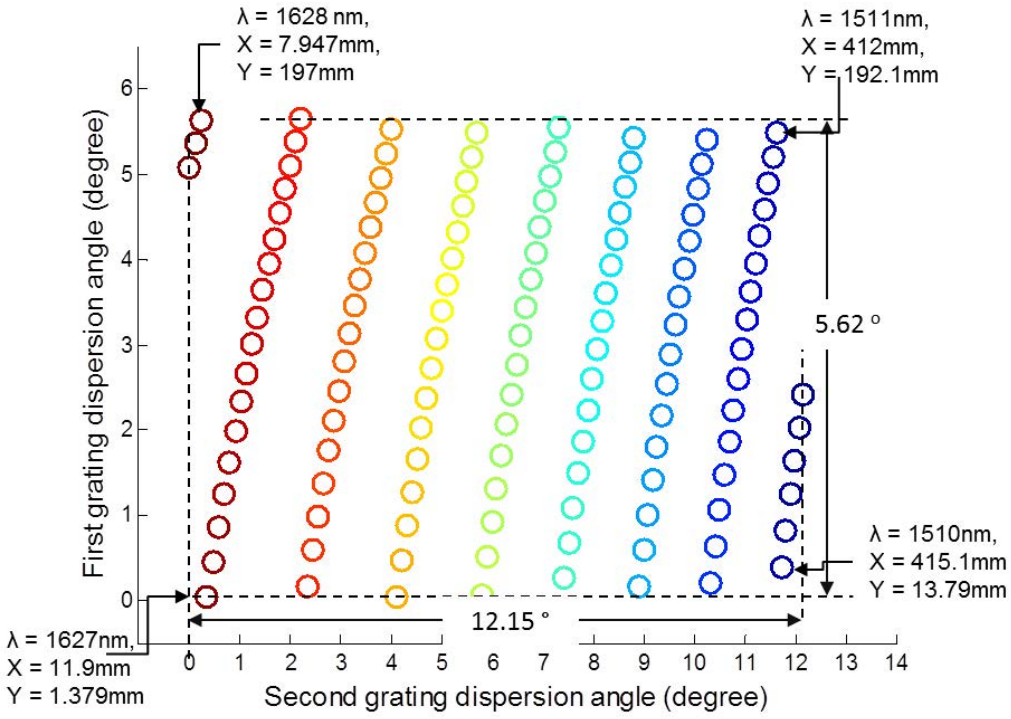

Figure 5.7: Resulting two-dimensional area scan using a combination of cascaded reflection grating (blaze angle 80.7° and 13.33 grooves/mm, mounted near-Littrow angle; product number Newport 53004BK06-182E) with a fused silica transmission grating of 1000 grooves/mm over a wavelength range between 1505 nm and 1630 nm mounted with incidence angle near 49.9° (product number Ibsen PING-sample-083). Lateral size of coverage is calculated for a distance of 2 m.

by wavelength tuning between 1511 nm and 1627 nm.

5.2.1 Optical power loss

Table 6.2 reports the optical power loss across wavelengths in the free-space systems for the cascade of a reflection grating and a transmission grating. The optical power loss is the power difference measured at the fiber level just before the Tx lens collimator and right after the Rx lens collimator.

Table 5.1: Table 6.2: Measured free-space loss at each wavelength for cascaded reflection and transmission gratings (Module 2)

Wavelength (nm)	1518	1534	1550	1566	1583	1600
Free-space los(dB)	5.95	4.87	5.47	5.05	4.79	6.15

The system proposed has a loss of only between 4.79 dB and 6.15 dB (33.2% and 24.3% power efficiency) between wavelengths 1518 nm and 1600 nm. The main power loss contributions are from the collective losses of the gratings, misalignment, the specified insertion loss of the collimators, and the connector losses between the fiber and the pigtailed collimator at transmitting and receiving ends.It has been carefully selected to minimize on power loss. The first grating is an echelle grating with an efficiency between 30−50%and the second grating is a transmission grating with efficiency approaching 90%.

5.2.2 Channel bandwidth

Tthe system's bandwidth will here be adressed. The spectral response profile of a system has a major impact on the bandwidth of the overall system, next to the bandwidth of the receiver. Therefore, the spectral response is measured in order to determine the bandwidth limitation that the steering modules impose on the free-space transmission channel.The method used for measurement is carried out by transmitting an Amplified Spontaneous Emission (ASE) wideband signal originating from an Erbium-Doped Fiber Amplifier (EDFA) and measuring the received beam's power with an Optical Spectrum Analyzer (OSA) at a resolution of 0.01 nm.

As observed in Fig. 5.8, an average recorded spectral bandwidth of 9.53 GHz is recorded for wavelengths between 1518 nm and 1600 nm. When DMT modulation is turned on, an average bandwidth of 9.55 GHz is measured. Thus, we see that modulation of the signal has a negligible effect on the spectral bandwidth. This means that spectral broadening is negligible with DMT modulation of approximately 10 GHz. Again, note that this is dependent on the optical spectrum broadening by the modulation; if it were bigger than the static optical bandwidth, then, we may expect a bigger impact. The insets, bordered by dashed-lines, show the spectral bandwidth for

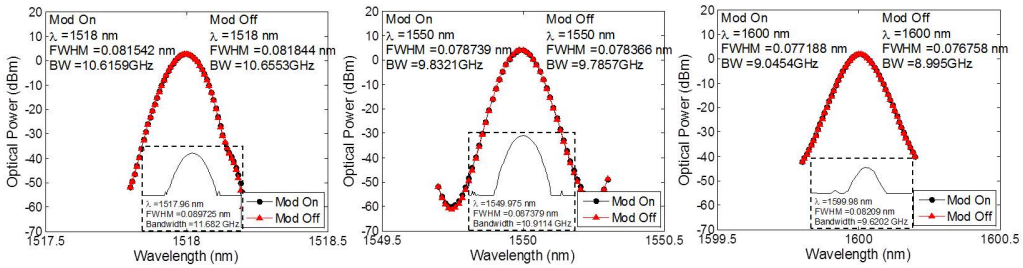

Figure 5.8: Spectral bandwidths at $\lambda = 1518$ nm, 1550 nm and 1600 nm at 2 m distance for cascaded reflection and transmission gratings.

non-modulated signals measured using the OSA which results in an average of 10.74 GHz. The difference of about 1.2 GHz may be attributed to the re-alignment of the system in the separate transmission measurement and spectral bandwidth measurement.

5.2.3 Beam profile

The beam profiles of the 2D-steered beams have been measured by using the alignment robotto displace the position of the receiving lens in order to map the optical power across the beam. At 2 m distance, the profiles naturally give a larger beam diameter than at the originating beam waist which is 3.33 mm in diameter at 12.91 mm in front of the collimator housing. The Full Width Half Maximum (FWHM) and $1/e^2$ (= reference point at the beam waist) can be obtained from the Gaussian profiles which are measured when the DMT modulation is turned on and turned off. This way, we can observe the effects of modulation on the dispersion and the size of the beam after transmission. The beam profiles of wavelengths 1518 nm, 1534 nm, 1550 nm, 1566 nm, 1583 nm, 1600 nm and 1618 nm, as shown in Fig. 5.9, are measured. On average, the beam width measured at FWHM is 2.41 mm and at $1/e^2$ is 4.13 mm. When DMT modulation is turned on, the beam width measured at FWHM is 2.44 mm and at $1/e^2$ is 4.13 mm. By comparing the results for static and modulated channels, negligible differences in the beam profiles are observed.

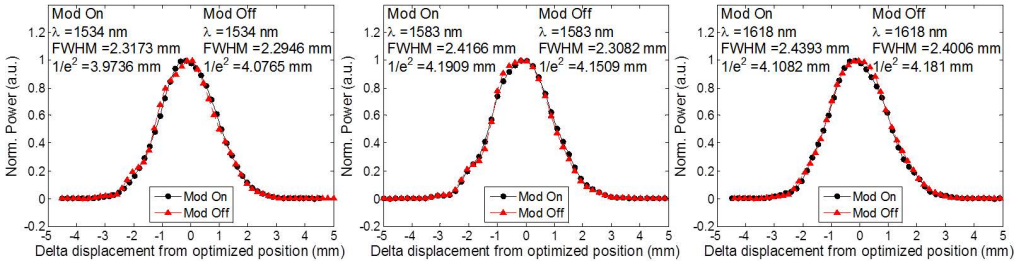

Figure 5.9: Beam profiles of channels measured at 2 m distance with λ = 1534 nm, 1583 nm and 1618 nm, for cascaded reflection and transmission gratings.

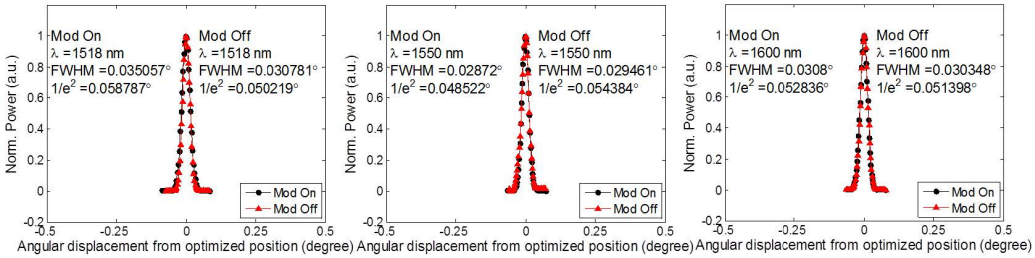

Figure 5.10: Measurement of the lens tilt tolerance at λ = 1518 nm, 1550 nm and 1600 nm at 2 m distance for cascaded reflection and transmission gratings.

5.2.4 Receiver full-field of view

In this section, we measure the extent of tilt for the collimators.In general, the small FFoV limits the receiver's acceptance angle and demands a tedious alignment.

The results are shown in Fig. 5.10. Of the seven measurements taken, the angles measured at FWHM are between 0.029° and and 0.031°, and at $1/e2$ the angles are between 0.050° and 0.054°. When DMT modulation is turned on, the angles measured at FWHM are between 0.029° and 0.035°, and at $1/e^2$ the angles are between 0.049° and 0.059°.

The measurements show that the steering system is very precise. Although these collimators have excellent light collimation efficiency, with a loss of $<$ 1 dB over 2 m, their reception angle is very small, thus, requiring tedious alignment at the receiving end. Therefore, it is vital to implement a small

form factor receiver with larger FFoV in order to ease channel establishment and reception in a practical scenario. This is one subject that needs to be developed further to ease the system's alignment and consequently, the ease of connection establishment.

5.2.5 Transmission: Cascaded reflection and transmission gratings

The performance of the 2D-steered system employing the cross-mounted reflection and transmission gratings is evaluated using OOK-NRZ (Subsection 6.8.1) signaling and the communication channels are further optimized using the spectrum-efficient DMT modulation format (subsection 6.8.2) which is widely employed in copper-based Digital Subscriber Line (DSL) user access networks for high speed transmission.

2 m free-space transmission with OOK-NRZ signaling

A laser beam with a wavelength of 1550 nm is employed as the optical carrier signal. An OOK-NRZ signal is generated using a pattern generator with a PRBS length of $2^{31} - 1$ bits. The modulated signal from the pattern generator is amplified with an EDFA up to at most 9 dBm. The signal is then transmitted to free space through a triplet lens collimator from Thorlabs (TC18FC-1550) with a focal length of 18.36 mm and a full-angle divergence of 0.034°. The $1/e^2$ beam diameter is 3.33 mm at the focal plane.The beam is illuminated onto the highly dispersive reflective echelle grating and then onto the fused silica transmission grating. Then, the beam is reflected on a mirror to be collected by an identical collimator after a free-space distance of 2 m. The collimated beam is directed into the receiver and thereby, the BER performance is computed. The eye-diagram is sampled on an Agilent sampling scope. BtB measurements are made by replacing the free-space link with a SMF of 1 m in length. The complete experiment is repeated by varying the data rate generated by the pattern generator. The optical power loss in free space is measured up to 6.15 dB as shown in Table 6.2. Using the energy-efficient and simple-to-implement OOK-NRZ modulation format, error-free transmission, i.e. an error-free channel at bit error rate, BER $\leq 1 \times 10^{-9}$, of up to 15 Gbps is obtained. Fig. 5.11 shows the BER performance measured between 6 Gbps up to 13 Gbps.

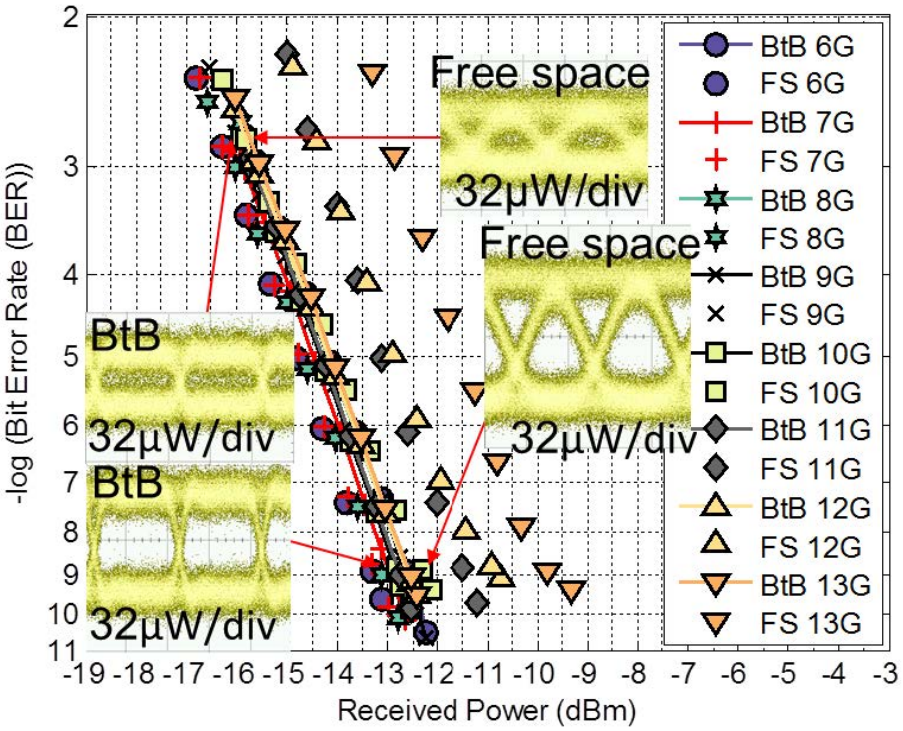

Figure 5.11: Link performance at OOK-NRZ between 6 Gbps and 13 Gbps transmissions with eye diagrams for 10 Gbps free space and BtB.

For transmission up to 10 Gbps, the free-space channels have at maximum a negligible 1 dB penalty from the BtB performance. The penalty increases to more than 1 dB at 11 Gbps and above. This shows that the free-space steering module has a bandwidth limitation of approximately 10-11 Gbps. The observed eye diagrams for 10 Gbps at BER = 1.61×10^{-3} and BER = 1.46×10^{-9} are shown in Fig. 5.11 in comparison to the BtB SMF performance at BER = 1.05×10^{-3} and BER = 1.47×10^{-9}. Further extending the measurements to the FEC limit (BER at 1×10^{-3}), up to 16 Gbps transmission is achieved, as shown in Fig. 5.12.

The corresponding eye-diagrams at 15 Gbps transmission with BER = 1.50×10^{-3} and at BER = 1.67×10^{-9} have distorted eyes although they are still open and clean. In addition, the spectrum of the transmitted signal through a SMF and through our free-space system is measured. Figures 5.13 and 5.14 show the spectrums for 10 Gbps and 15 Gbps signals, respectively,

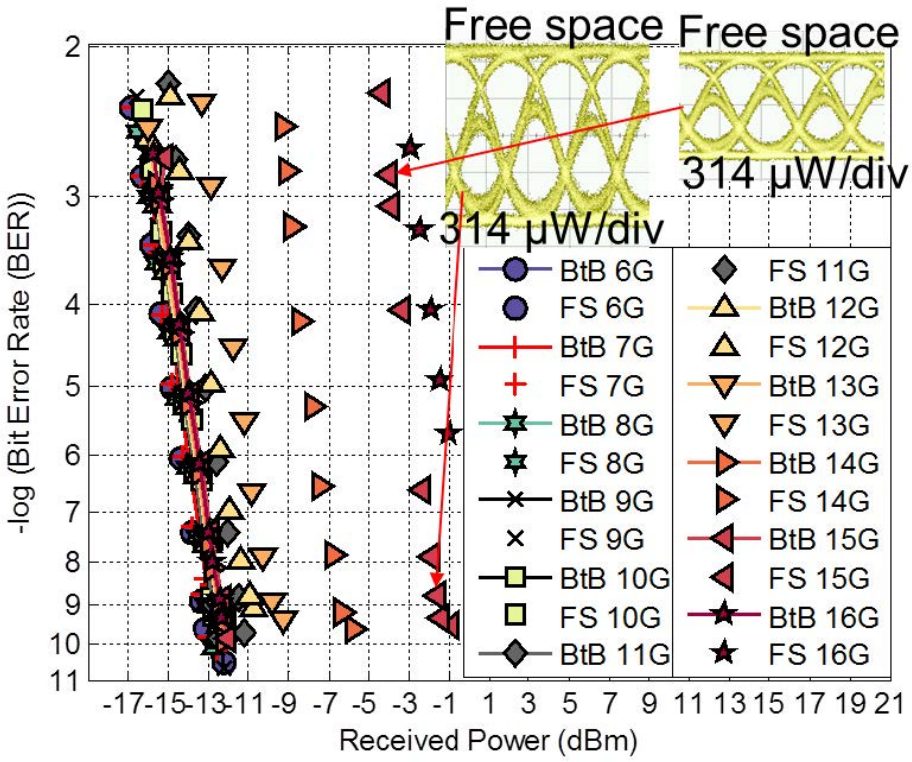

Figure 5.12: Link performance at OOK-NRZ between 6 Gbps and 16 Gbps transmissions with eye diagrams for 15 Gbps free space.

through SMF (measured after the EDFA) and free space (after the receiving collimator). The grating module in combination with the aperture of the transmitting and receiving lens coupler, behaves as a bandpass filter that allows the baseband spectrum. ASE noise from the EDFA is also significantly filtered.

2 m free-space transmission with DMT signaling

The data signal is generated using an AWG and modulated onto the optical carrier via a 10 GHz bandwidth MZM. The free-space beam is received with a 10 Gbps bandwidth photoreceiver and the signal is captured with a real-time scope and processed with Matlab to calculate the BER and signal constellations. The experiment is repeated for several wavelengths from different diffraction orders (scanning lines) of the steering module. These

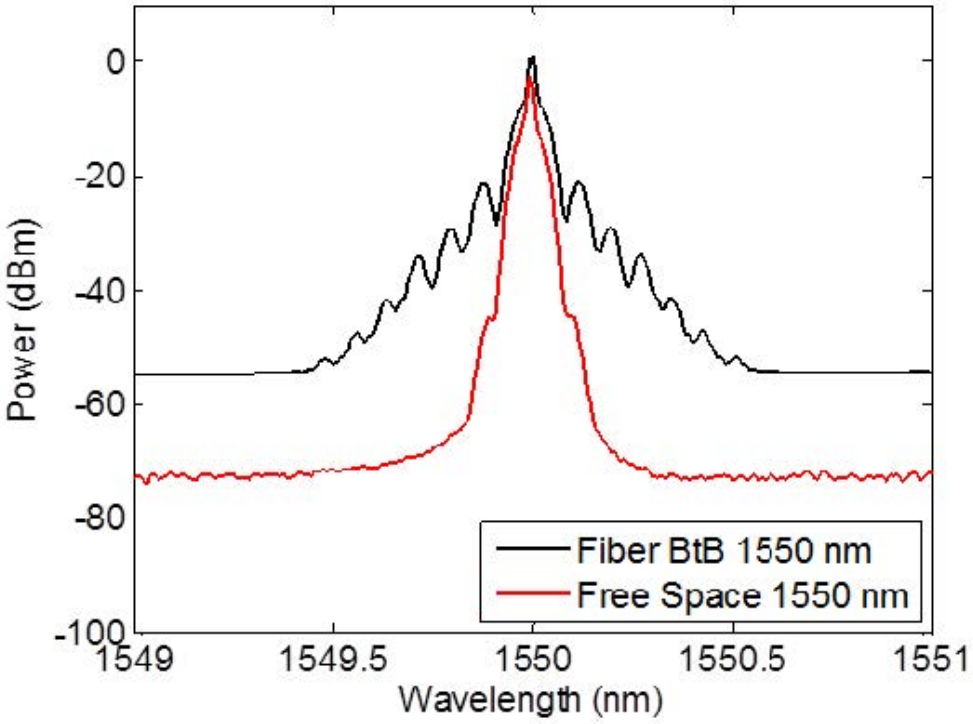

Figure 5.13: Transmission spectrum in SMF versus steered free-space channel at 10 Gbps. The peaks seen in the Fiber BtB repeats at approximately 10 GHz interval. Shaping of the spectrum by the free-space beam steering module can be clearly observed.

measurements are compared to the 2 m distance performance of a direct free-space link (without steering modules) as a BtB benchmark. Fig. 5.15 shows the performance of the DMT signals at 1518 nm, 1534 nm, 1550 nm, 1566 nm, 1583 nm, and 1600 nm.

These measurements are compared to a direct free-space link, which acts as the BtB measurement. The bitrates reported are measured at FEC-limit BER of 1×10^{-3} and with a received optical power of 0 dBm except at λ = 1600 m, at 0.5 dBm. In general, we see a consistent data rate penalty of about 5 Gbps between the free-space BtB and the steered channels. This is due to bandwidth limited performance of the beam-steered optical channel.Fig. 5.16 shows the channel performance with a DMT signal at different wavelengths.

We observe that for the direct free-space BtB channel, 9.95 GHz channel is bit-loaded corresponding to the SNR. For the 2D-steered free-space beams,

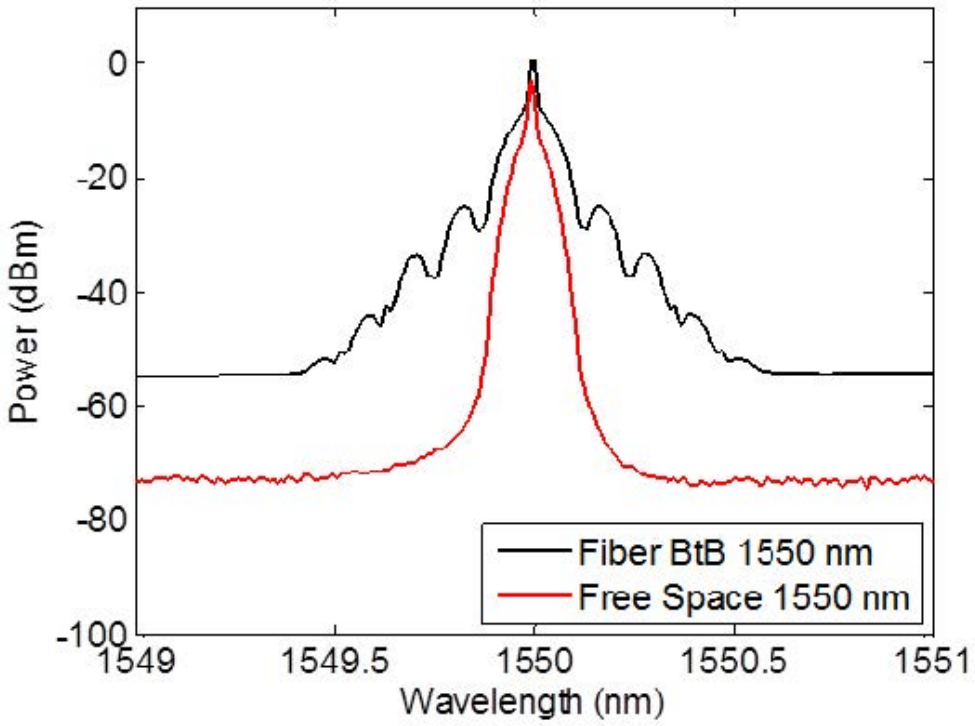

Figure 5.14: Transmission spectrum in SMF versus steered free-space channel at 15 Gbps. Shaping of the spectrum by the free-space beam steering module can be clearly observed.

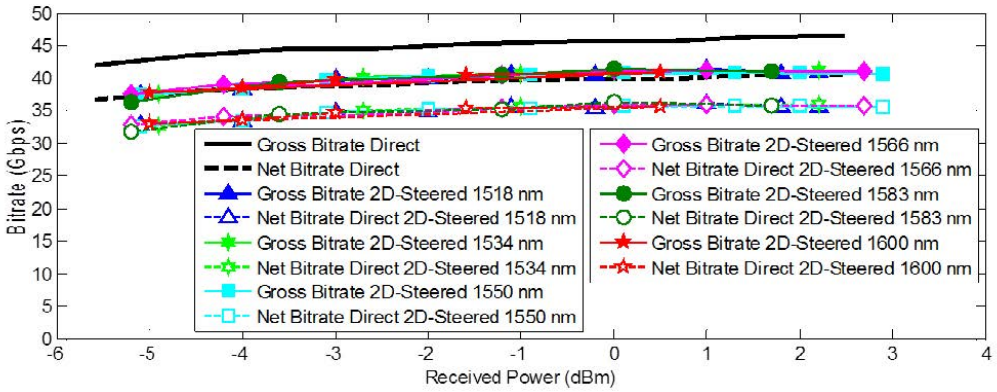

Figure 5.15: Performance of 2D beam-steered channels compared to free-space BtB channel, with DMT signaling.

transmission bits are only allocated in bandwidths of 8.625 GHz, 8.962 GHz, 8.67 GHz, 8.603 GHz, 8.647 GHz and 8.603 GHz for the above mentioned

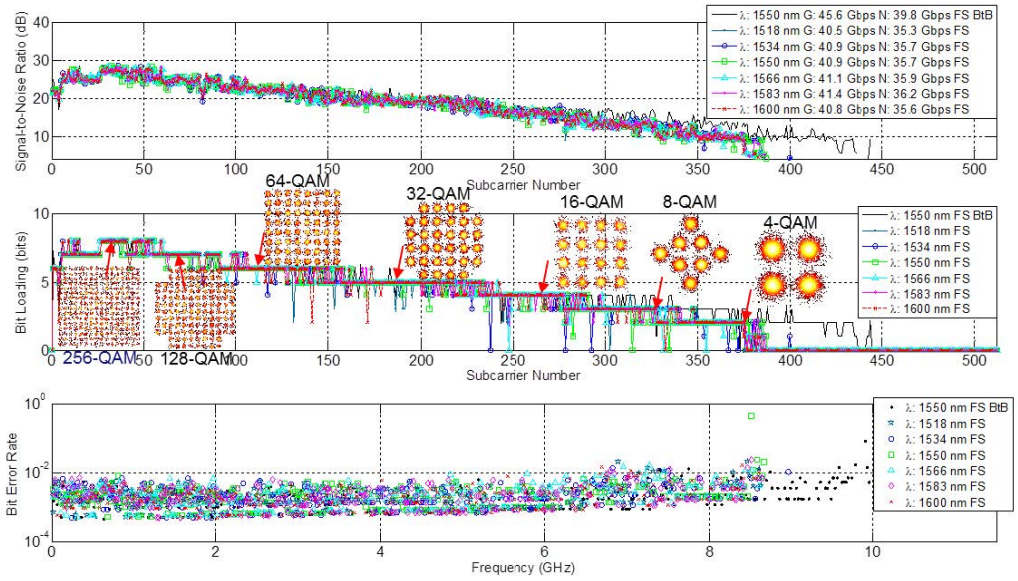

Figure 5.16: SNR, bit loading and BER of DMT signals at multiple wavelengths in a cascaded reflection and transmission gratings setup.

wavelengths respectively. The highest bitrate is achieved at $\lambda = 1583$ nm with a gross bitrate of 41.4 Gbps and a net bitrate (after the deduction of the cyclic prefix, preambles and 7% overhead for FEC coding) of 36.2 Gbps. For frequency carriers with sufficient SNR, a signal constellation up to 8 bits, equivalent to 256-QAM, is allocated.The measurements are repeated at different distances between the Pencil Radiating Antenna (PRA) and the receiver, and also with three different wavelengths. The optical channel performance has been consistent for measurements at different receiver-to-PRA distances, as shown in Fig. 5.17. We see that there is no correlation between the distance and the performance since the beam width up to about 4 mm is still within the opening aperture size of the collimator with negligible dispersion. Gross and net bitrates of up to 41.6 Gbps and 36.3 Gbps are achieved with BERs of less than 2×10^{-3} i.e. below the hard-decision FEC limit for near error-free performance.

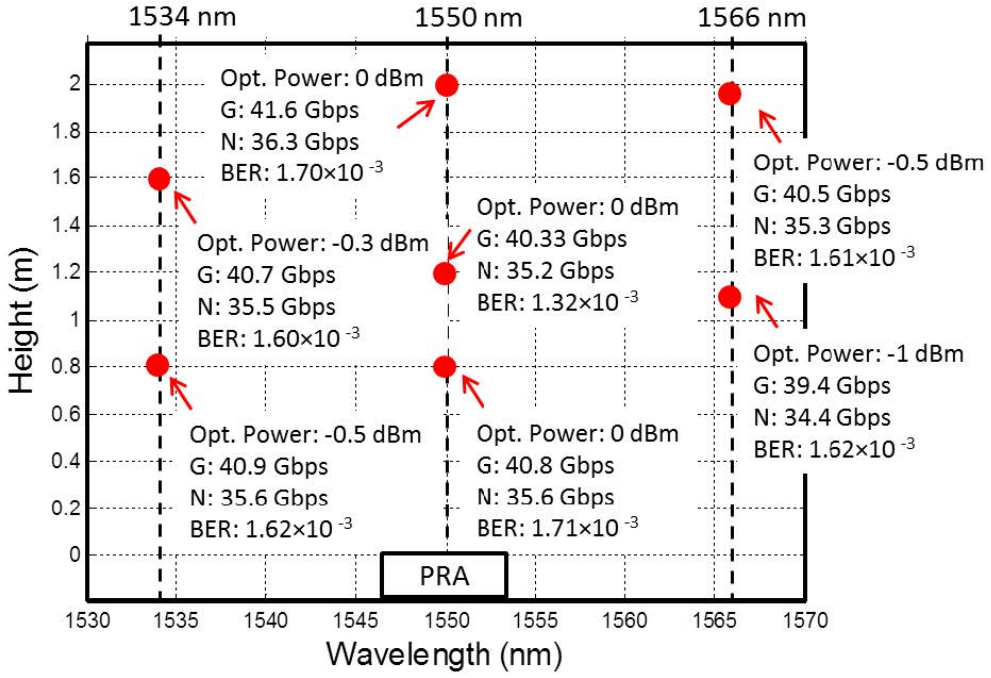

Figure 5.17: Measurements at different distances/height between devices and the PRA.

3 m free-space transmission with OOK-NRZ

A testbed, as depicted in Fig. 5.19, is constructed to evaluate beam-steering with wavelength tuning over 3 m distance. An OOK-NRZ signal is generated with a PRBS of length $2^{31} - 1$ bits. An MZM is used for data modulation onto a 12.5 dBm optical carrier signal. The MZM has a loss of approximately 7-8 dB. A 3.3 mm wide optical beam is then transmitted to free space through a triplet lens collimator from Thorlabs (TC18FC-1550) with a focal length of 18.36 mm and a full-angle divergence of 0.034°. The $1/e^2$ beam diameter is 3.33 mm at the focal plane. For further information on the lens collimator please refer to Section 4.1. The free-space beam impinges onto the pair of crossed reflection and transmission gratings. Silver-coated mirrors are used to extend the free space distance to over 3 m. At the receiving device, an identical lens collimator is used to collimate the propagated beam into an optical receiver. Finally, the electrical signal is analyzed by observing the eye-pattern on a sampling scope and the BER performance is evaluated by a BERT. Fig. 5.18 shows the BER performance for 10 Gbps OOK-NRZ signals.

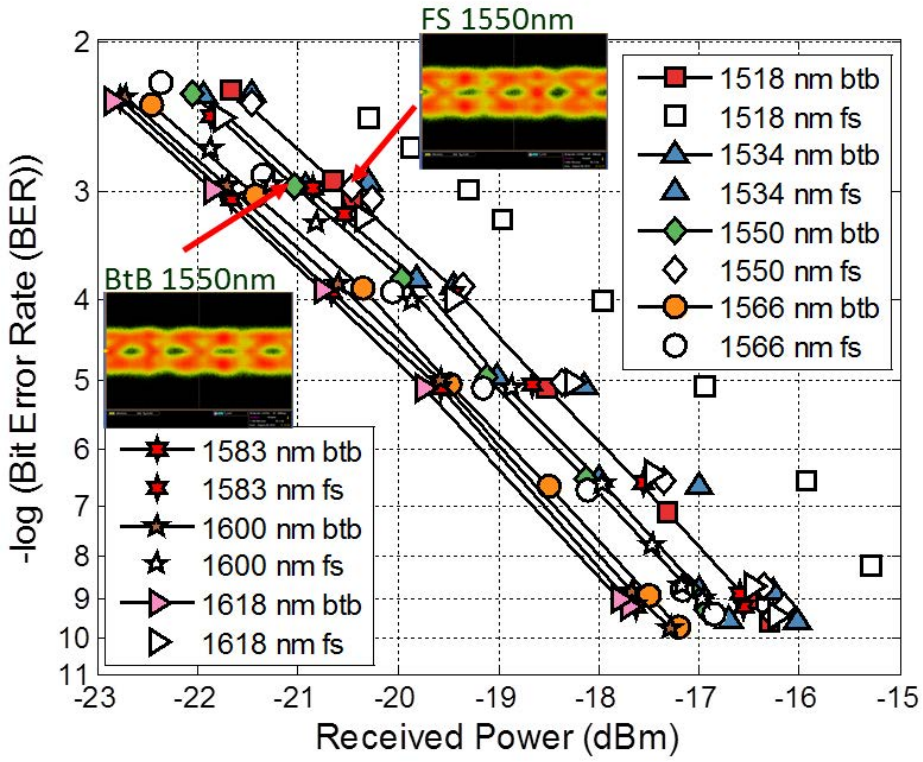

Figure 5.18: BER performance for OOK-NRZ transmission at 10 Gbps. Insets: eye-diagrams at BER = 1×10^{-3} for fiber BtB and steered free-space (fs) transmission at 1550 nm.

In general, steered free-space channels have ¡ 1 dB penalty from fiber BtB performance, which is an acceptable system penalty [115]. However, penalty of $1 - 2$ dB is seen for wavelengths 1583, 1618 nm and 1518 nm. The additional penalty is contributed by the optimization of the modulator each time the wavelength of transmission is changed, and the dispersion caused by slight wavelength dependence of the modulator as can be seen from the BtB measurements. Additionally, for wavelength 1518 nm and 1618 nm, the tunable laser provides a lower output power. This results in a lower SNR compared to the other channels.

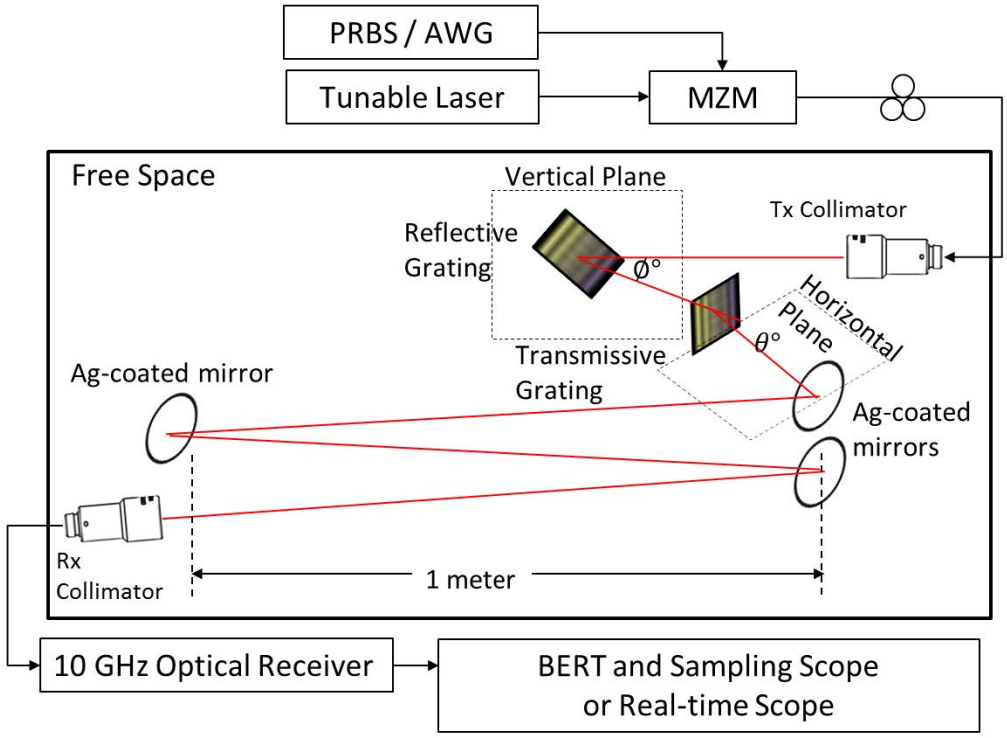

Figure 5.19: Testbed setup for free-space transmission with 2D optical beam steering over 3 m distance.

3 m free-space transmission with PAM transmission

For the evaluation of 4-PAM transmission, the testbed as shown in Fig. 5.19 is used. The data signal is generated from an AWG and evaluated using a real-time oscilloscope.

Extensive measurements have been carried out for two wavelengths, i.e. 1520 nm and 1550 nm. The target for error-free performance with hard decision FEC is BER $\leq 2 \times 10^{-3}$. Optical fiber BtB measurements were carried out to benchmark the performance of free-space links. Fig. 5.20 shows the BER performance measured at 12, 14, 15 and 16 Gigabaud (GBaud) for 1550 nm, and at 15 and 16 GBaud for 1520 nm. In Fig. 5.20(a) for 1550 nm, we observe power penalties of 0.63 dB (12 GBaud), 1 dB (14 GBaud), 1.93 dB (15 GBaud), and 2.07 dB (16 GBaud) while from Fig. 5.20(b) for 1520 nm, we observe power penalties of 2.46 dB (15 GBaud) and 1.21 dB (16 GBaud). The inconsistency seen in Fig. 5.20(b) is highly likely due to the imperfect

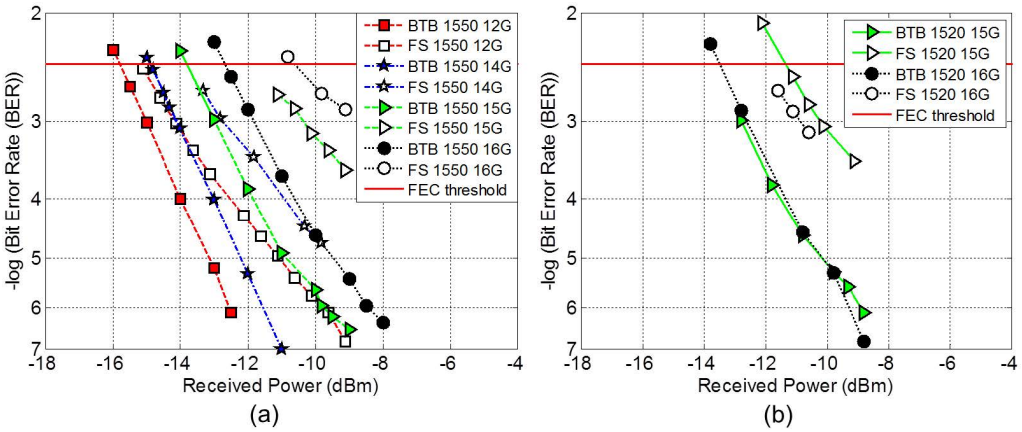

Figure 5.20: BER Performance: (a) 1550nm (12,14,15 & 16 GBaud); (b) 1520nm (15 & 16 GBaud); FS: Free space, BtB: Back-to-back.

adjustment and alignment of the link when changing over from BtB to free space reconfiguration. The measurements for Fig. 5.20(a) were completed for free space and BtB without reconfiguring the system in between. All the measured performances were below hard decision FEC threshold of BER $\leq 2 \times 10^{-3}$. Fig. 5.21 shows the observed eye-diagrams for BtB and free-space performances at 15 GBaud for both 1550 nm and 1520 nm. At BER $\leq 1 \times 10^{-3}$, the eye levels are still distinguishable with negligible eye-skew.

5.3 Chapter conclusion

In the first part of this chapter, a one dimensional beam steering concept was introduced. It was shown that the propagation distance, as long as the beams are fully captured by the opening aperture of the coupling lens, did not affect the channel performance, indicating that the free-space channel did not add noticeable dispersion. The link performance was basically limited by the available transmitted power, grating loss and receiver sensitivity. Transmission measurement of up to 2.5 m were also evaluated using OOK-NRZ and DMT signal formats, in which up to 10 Gbps and 36.7 Gbps were demonstrated, respectively.

In the second part of this chapter, a 2D beam steering established by an orthogonal cascade of a reflection and a transmission grating has been

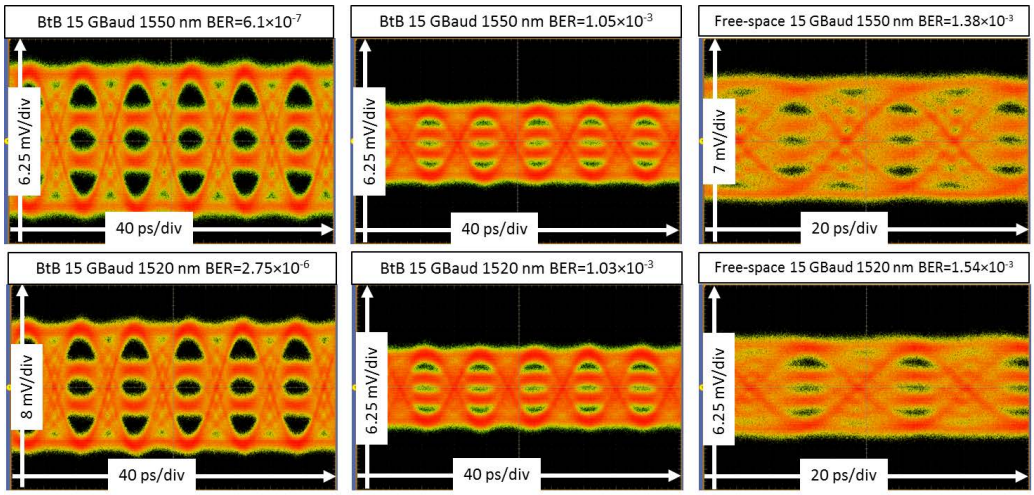

Figure 5.21: Eye-diagrams for top row: 1550 nm, and bottom row: 1520 nm; columns 1 and 2: Back-to-back ; column 3: Free space.

presented. This module has only up to 6.15 dB loss in the full steering range between 1518 nm to 1600 nm. The end-to-end link bandwidth is approximately 10 GHz. In the experimental demonstrations, a promising bitrate of 15 Gbps error-free channel is achieved using OOK-NRZ modulation format. In this experiment, we observed the ASE reduction in the free-space channel obtained by the optical filtering of the 2D steering modules which may help to improve SNR performance of the system as a bonus. Further, by employing the DMT modulation format in order to increase spectrum efficiency, up to a gross bitrate of 41.4 Gbps with a corresponding net bitrate of 36.2 Gbps at the hard decision FEC limit is achieved. The free-space transmission distance was further improved to 3 m distance and evaluated using OOK-NRZ signaling in which 10 Gbps was achieved with BER $\leq 1 \times 10^{-9}$, with wavelength tuning of up to seven wavelengths. With 4- PAM signaling, up to 32 Gbps at 16 GBaud was achieved with FEC-correctable transmission (BER $\leq 2 \times 10^{-3}$). For systems further than 3 m distance, we will have to take into account the beam size due to the divergence of the Gaussian beam. As long as the diverged beam has a diameter smaller than the size of the receiving collimator, lens receiver, photodetector surface, etc., we can expect to achieve a performance close to the reported results. However, when the diverged beam size becomes larger than the effective area of the receiver, the ratio between the effective receiving area and the diverged beam size at the

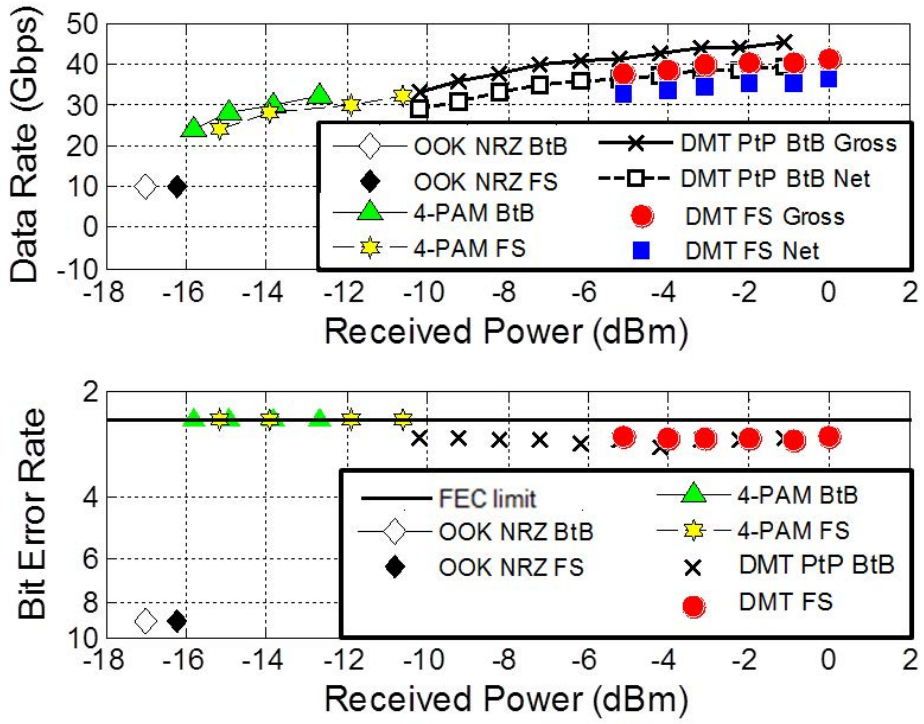

Figure 5.22: Summary of measured performances for OOK-NRZ, 4-PAM and DMT signals.

receiving plane has to be taken into account, as shown in [84].

In summary, by employing a 10 GHz bandwidth-limited system, 32 Gbps at -10.62 dBm was achieved using 4-PAM and 41.4 Gbps (net 36.2 Gbps) at 0 dBm was achieved with DMT, as shown in Fig. 5.22, both below the FEC limit. The results show that 4-PAM signaling can have at least the same channel performance as the more complex DMT signaling while being easier to realize in real-time circuitry and having less latency. The 4-PAM system shows interesting results for the realization of future high-capacity narrowbeam optical wireless systems without the need for further complex signal processing at the user side such as needed for DMT.

Chapter 6

Arrayed Waveguide Grating for 2D beam steering

An Arrayed Waveguide Grating (AWGr) will now be discussed, designed by Prof. A.M.J. Koonen and evaluated by Dr. A. M. Khalid [116]. This work has been introduced and reported in [116, 117]. In the second part of the chapter, an improvement of this technique will be presented and carefully discussed, as it is the way optical signal are currently being transferred in our setup.

6.1 High port count AWGr steering concept

This approach employs a simple 2D arrangement of the fiber outputs of an arrayed waveguide grating module. The advantages of this method are its construction simplicity, its potentially larger coverage area and that it is passive. The 2D fiber array design determines the coverage of the area while the AWGr provides the output ports which carry different wavelength channels to each of the ports of the 2D fiber array.

The principle is illustrated in Fig. 6.1(a). An optical lens with a focal length f, is placed in front of the 2D array of fibers. The fibers are displaced by an amount $\Delta x = x_n - x_{n-1}$. The spot size D_o, at the image plane of length L, is determined by using $D_o = 2f \tan \alpha$, with α being the half-angle divergence of the Gaussian beam out of the fiber. The distance between adjacent spots is determined using $\Delta b = \Delta x \frac{d}{f}$, where Δx is the pitch between the fibers in the array. The optimum configuration is when the spots are adja-

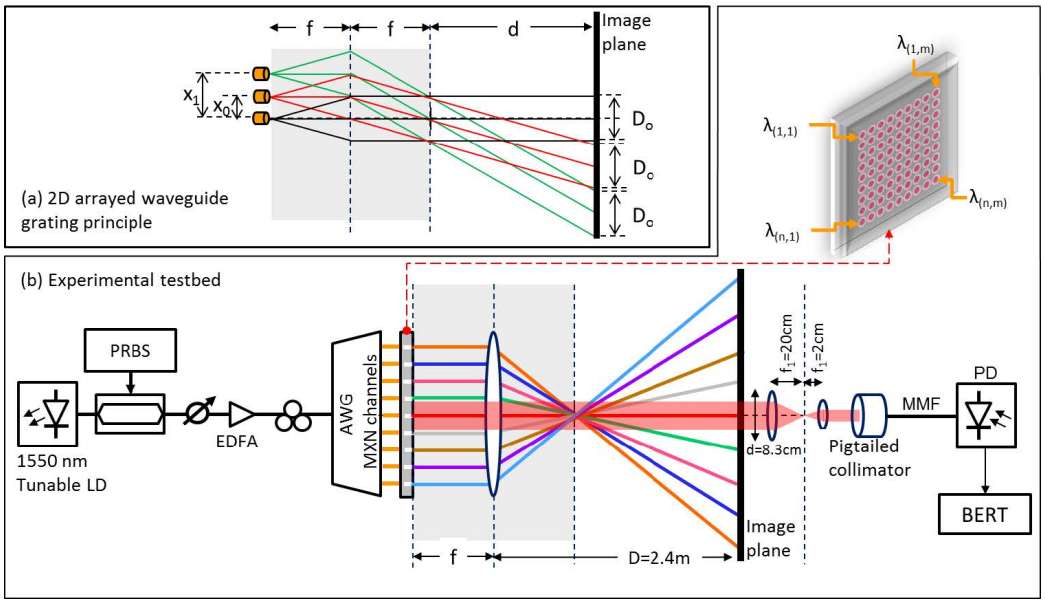

Figure 6.1: 2D arrayed waveguide grating technique; (a) Principle of operation;(b) Testbed setup for demonstration.

cent, so when $\Delta b = D_o$ with the corresponding pitch of $\Delta x = (2f^2 \tan\alpha)/d$. For an image plane of $L \times L$, m^2 spots with diameter D_o, with $m = L/Do$ are required. Finally the fiber pitch can be determined using:

$$\Delta x = \frac{L^2}{2dm^2 \tan\alpha} \tag{6.1}$$

and the focal length:

$$f = \frac{L}{2m \tan\alpha} \tag{6.2}$$

6.1.1 Experimental setup for 2D beam steering with AWGr

An experimental proof-of-concept setup is configured as shown in Fig. 6.1(b). The wavelength of the tunable laser is set to $\lambda = 1544.26$ nm and its optical power is -5 dBm. The optical carrier is modulated externally using an Mach-Zehnder Modulator (MZM). The Non-Return-to-Zero (NRZ)-On-Off-Keying (OOK) data signal is generated using Pseudo Random Binary

Sequence (PRBS) $2^{23}-1$ bits. The modulated optical signal is then amplified by using an Erbium-Doped Fiber Amplifier (EDFA) and fed into the input port of the arrayed waveguide grating. The transmitted optical power is 9.5 dBm, which is below the eye safety limit at $\lambda > 1.4$ μm. The Gemfire arrayed waveguide grating (product identification: 80ch AWG DMX LC/UPC) has 1×80 channels AWGr. Each channel is spaced at 50 Gigahertz (GHz) within wavelengths ranging from 1529.10 nm to 1569.80 nm. Using this 80-port arrayed waveguide grating, a $(9 \times 9) - 1$ 2D fiber array has been constructed. From the calculations for a room height of 2.5 m, the 9×9 2D fiber array pitch = 13 mm, spot size = 8.3 cm and the focal length of lens = 39.8 cm. This results in a coverage area of 0.75×0.75 m^2 and an angular coverage of $17° \times 17°$. The optical beams from the central output ports of the fiber array, i.e. ports 40 and 41 are launched into free space and are incident on the large lens with $f = 40$ cm and diameter, $D = 20$ cm). The 2D fiber array is positioned in the focal plane of the lens. The receiver is placed 2.4 m away from the lens. The size of the spot is de-magnified $10\times$ by a reverse telescope setup to a smaller beam before being coupled into the Multimode Fiber (MMF) which has a core diameter of 50 μm and a Numerical Aperture (NA) of 0.22. The optical signal is then transported to a 12 GHz PIN photo diode with Transimpedance Amplifier (TIA). The output is evaluated using a Bit Error Rate Tester (BERT).

6.1.2 Results and discussion

The results are shown in 9.2. The Bit Error Rate (BER) performances for HS-1 ($\lambda_{41} = 1544.26$ nm) and HS-2 ($\lambda_{41} = 1544.66$ nm) are measured at 2.4 m distance. A data rate of 10 Gbps is achieved near error-free BER of 1×10^{-9}. Approximately 1 dB penalty is observed with respect to a Single Mode Fiber (SMF) Back-to-Back (BtB) connection. The eye-diagrams at different received powers are also given.

Up to 10 Gbps was achieved using OOK-NRZ signaling, at BER $\leqslant 1 \times 10^{-9}$, with a sufficient beam size of 8.3 cm in a coverage area of 0.75×0.75 m^2. This straightforward approach is definitely advantageous in terms of simplicity. However, the demonstration was constructed using bulky arrays and lenses.In the next section the final PRA design will be carefully described, where the dimension of the lenses was significantly reduced.

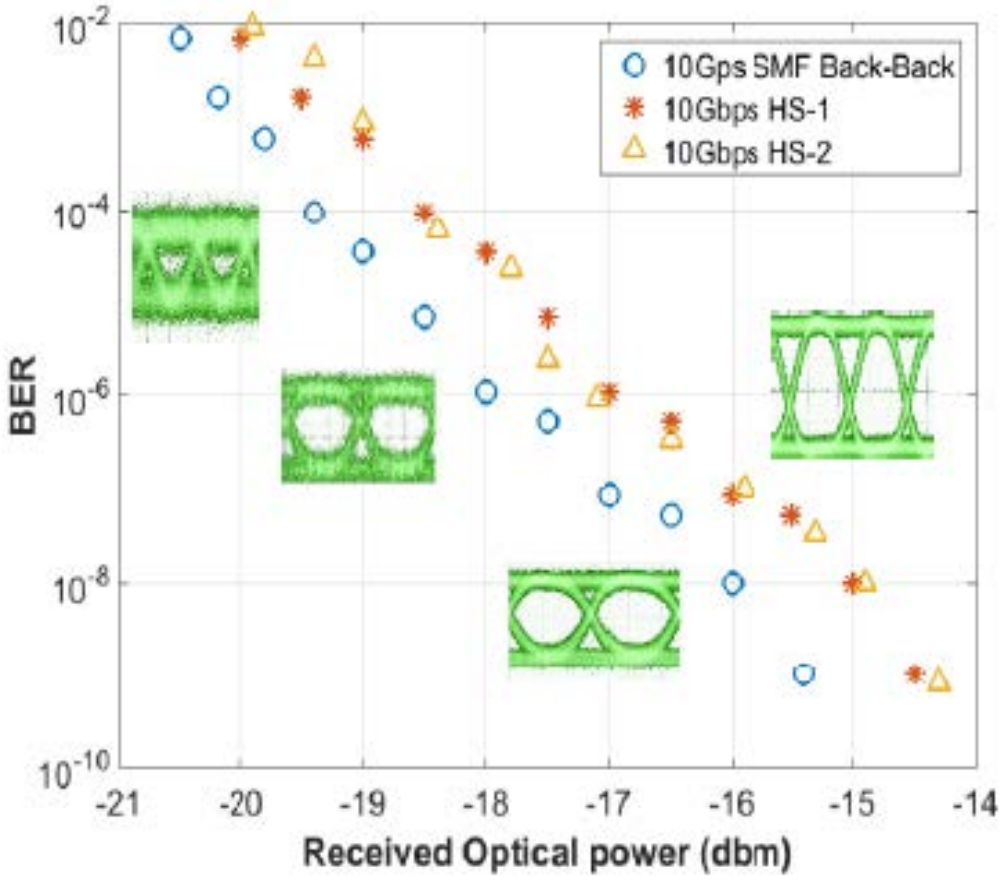

Figure 6.2: BER performance of HS-1 and HS-2 from ports 40 and 41 versus BtB SMF performance. Image taken from [116].

6.2 Beam Steering Module based on AWGr

The main idea introduced in this section consists in defocusing techniques in order to widen the FoV of the beam steering module, or significantly reduce the size of the lens used. The work reported in this section is largely taken from [118]. As an alternative approach which requires less alignment effort while using AWGR modules which are readily available commercially, we propose the beam steering module concept shown in Fig. 6.3 [119, 120].

The $N \cdot M$ output fibers of the AWGR are arranged in an $N \times M$ 2D fiber array, which is put in the object plane of a lens. The position of a fiber in the object plane determines in which 2D direction its corresponding beam is emitted after the lens. By putting the fiber array in the focal plane of the

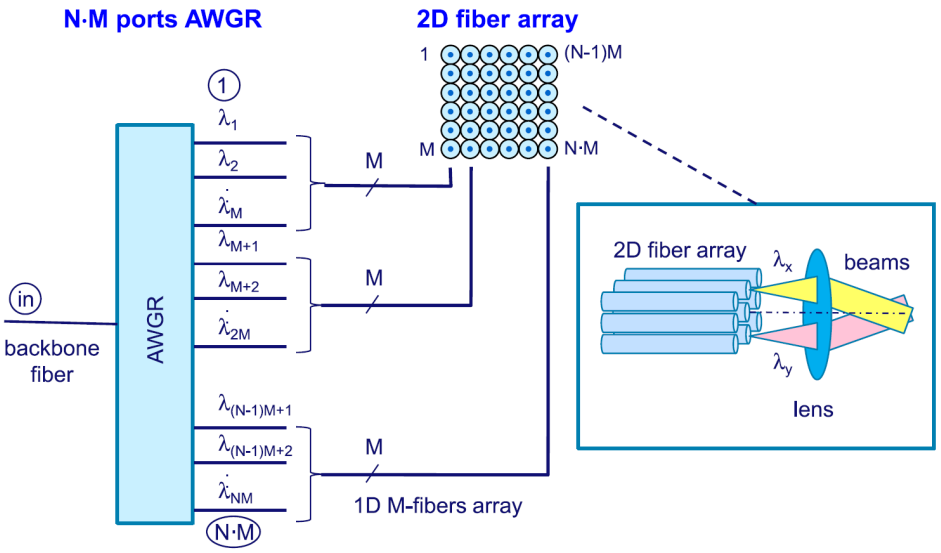

Figure 6.3: 2D steering of IR beams using a high port-count AWGR.

lens, collimated beams will be emitted with diameter $D_0 = 2f \tan(\alpha)$ where $\tan(\alpha) = \lambda/(\pi w_0)$ with mode field radius w_0 of the singlemode fiber. Each collimated beam creates a spot in the image plane with diameter $D_{spot} = D_0$. To cover a square image area of size $L \times L$ with no spacing between adjacent spots, $N = M$ and the number of AWGR ports needed is $N \times M = M^2 = (L/D_{spot})^2$. The spacing Δy of the fibers in the 2D array needs to be $\Delta y = L/[M \cdot (b/f - 1)]$ where $f = \pi w_0 L/(2\lambda \cdot M)$ is the lens focal length, and b is the distance between the image plane and the lens. E.g., for $D_{spot} = 3$ cm, $\lambda = 1.5$ μm, $m_0 = 4.5$ μm (so $\tan(\alpha) = 0.106$), $L = 1.5$m and room height b = 2.5 m, we need an array of $M \times M = 2500$ fibers with $\Delta y = 1.80$mm and $f = 14.1$ cm. For a given image area, a larger spot size D_{spot} will reduce the AWGR port count needed; but obviously also requires a larger aperture at the receiver in order to assure that enough power is detected to handle the large data rate. Commercially available AWGrs operating in C-band are typically offered with port counts up to 96. In previous experiments [119], we used an AWGR with 80 ports, so $M = 9$. To cover an area of only 0.75×0.75 m^2 using a spot size $D_{spot} = 8.3$ cm, a large condenser lens was needed with $f = 39.3$ cm and diameter $D_{lens} = 21$ cm, and fiber spacing $\Delta y = 15.5$ mm which yielded a 2D fiber array total size of 12.4×12.4 cm^2.

The size of such rather bulky setups can be reduced significantly by a defocusing approach: when putting the fiber array out of focus and closer

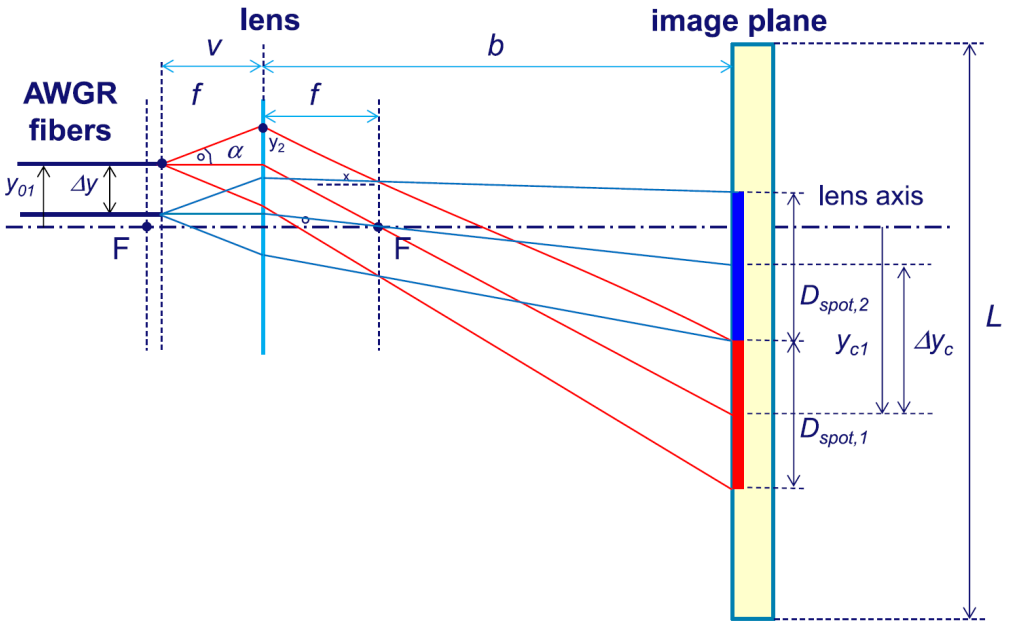

Figure 6.4: Reducing the beam steering module by defocusing the fiber array.

to the lens, the emitted beams are slightly diverging and the spot diameter D_{spot} increases. Conversely, for a given coverage area and a given acceptable spot diameter D_{spot}, defocusing results in a significantly smaller focal length and diameter of the lens, and smaller spacing between the fibers in the array, and thus to a significant reduction of the size of the beam steering module. The relative defocusing parameter p (with $0 \leq p < 1$) can be defined by $v = (1-p) \cdot f$ where the object distance between the array and the lens is given by v. In order to cover an $L \times L$ area at distance b_0 from the lens while having no spacing between the spots, from Fig. 6.4 using paraxial geometric optics it can be shown that the required lens focal length f, lens diameter D_{lens}, fiber spacing Δy, spot diameter D_{spot} as a function of distance b, and beam divergence dD_{spot}/db are:

$$f = \frac{1}{1-p}\left(\frac{L}{M \cdot 2\tan\alpha} - p \cdot b_0\right) \tag{6.3}$$

$$D_{\text{lens}} = (M-1)|\Delta y| + 2f(1-p)\tan\alpha \tag{6.4}$$

$$\Delta y = 2f\tan\alpha\left(\frac{f}{b_0 - f} + p\right) \tag{6.5}$$

$$= \frac{L}{M} \cdot \frac{L - pb_0M \cdot 2\tan\alpha}{-L + b_0M \cdot 2\tan\alpha} \tag{6.6}$$

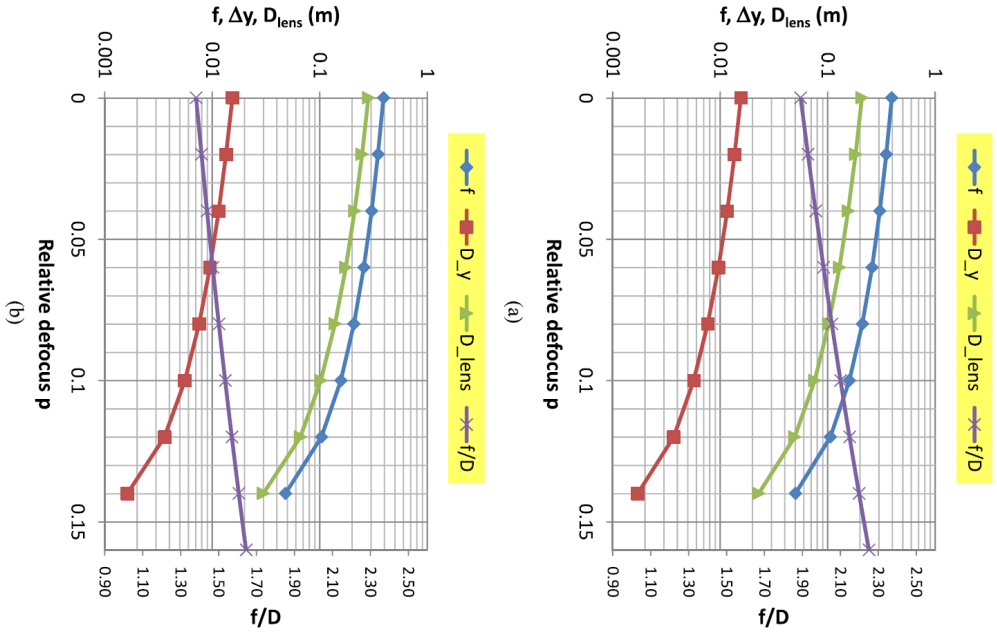

Figure 6.5: Reducing the module size by defocusing, when opting for a beam diameter Dsp ot = 8.3 cm and applying (a) AWGR with 81 ports (M = 9), or (b) AWGR with 196 ports (M = 14).

$$D_{\text{spot}}(b) = 2\tan\alpha \cdot \{f + p(b - f)\} \tag{6.7}$$

$$\frac{dD_{\text{spot}}(b)}{db} = 2p \cdot \tan\alpha \tag{6.8}$$

Fig. 6.5 illustrates the impact of the defocusing on the module?s size. As shown in Fig. 6.5(a), for an 81 ports AWGR and coverage area of 0.75 × 0.75 m^2 with room height b_0 = 2.5 m, no defocusing (so $p = 0$) yields a lens focal length f = 39.3 m , fiber spacing Δy = 15.5mm and lens diameter D_{lens} = 20.8 cm for a spot size D_{spot} = 8.3 cm (which was used in [119] and [121] to realize a beam supporting up to 35 Gbit/s OOK data transmission). However, using a defocusing of 12% (so $p = 0.12$), we find f = 10.5 cm, Δy = 3.67 mm, and D_{lens} = 4.90 cm only, while the spot size stays the same and hence the transmission capacity also. Clearly, defocusing can reduce the size of the beam steering module considerably without affecting the system?s performance. A larger defocusing also decreases the lens speed needed, so increases the f-number f/D: it increases from f/D = 1.83 for no defocusing ($p = 0$) to f/D = 2.15 for $p = 0.12$. Similarly, for an AWGR with a larger port count, the coverage area can be increased while the defocusing keeps the

module compact. As shown in Fig. 6.5(b): when adopting the same spot size $D_{spot} = 8.3$ cm, for a 196 ports AWGR ($M = 14$) at room height $b_0 = 2.5$ m, a $1.16 \times 1.16\text{m}^2$ area can be covered with a defocusing factor $p = 0.135$ yielding $f = 61.2$ mm, $\Delta y = 2.08$mm and $D_{lens} = 3.83$ cm. Experiments in our laboratory setup with 9.5 dBm transmitted beam power and at the receiver a Keplerian telescopic 10× beam compressor with an aperture diameter of 5cm have shown that a spot size $D_{spot} = 12.0$ cm allows a data transmission rate of more than 10 Gbit/s in OOK modulation format. For this spot size, with $M = 14$ and $b_0 = 2.5$ m an area of 1.68 × 1.68m2 (equivalent with an angular coverage of 18.6° × 18.6°) can be covered with $p = 0.21$ yielding $f = 51.2$ mm, $\Delta y = 2.51$ mm, and $D_{lens} = 4.12$ cm (implying an f/D = 1.24 number of the lens, which is readily available e.g., for camera lenses). Another advantage of the defocusing approach is a better fill factor of the covered area.

Fig. 6.6 shows how the beams from two neighboring fibers each diverge when defocusing is introduced and the distance b between the lens and the image plane increases. Without defocusing ($p = 0$) the beams are collimated and do not diverge. If the lens focal length f and fiber spacing Δy values have been set according to the equations given before for a given lens-to-image plane distance b_0 , the spots will exactly touch each other in the image plane where the distance b to the lens equals b_0 . E.g., for $b_0 = 250$ cm and spot size $D_{spot} = 12$ cm, this is shown in Fig. 6.6(a) for $p = 0$ where the beam?s divergence $dD_{spot}/db = 0$, and in Fig. 6.6(b) for $p = 0.21$ where $dD_{spot}/db = 0.0445$ (i.e., a divergence halfangle of 1.28 deg.).

Fig. 6.7 shows how the spots are covering the image plane; herein the e^{-2} intensity contours of the Gaussian spot footprints are shown. The spots exactly touch each other when $b = b_0$, as shown in Fig. 6.7(a). When the image plane is moved to a larger distance from the lens (so when $b > b_0$), the spacing between the spot centers Δy_c increases, in fact:

$$\Delta y_c = \Delta y \cdot (b/f - 1) \tag{6.9}$$

Without defocusing (i.e., $p = 0$), the spot diameter D_{spot} stays constant and becomes smaller than the spot spacing Δy_c, hence the fill factor decreases when b increases [see Fig. 6.7(b)]. For $b < b_0$, overlap between the spots occurs [see Fig. 6.7(c)].

Fig. 6.8 shows how the spot diameter, the spacing between the spots, and the fill factor (i.e., the summation of the footprint areas of all spots divided

by the total coverage area) evolve for a hexagonal stacking of the fibers in the 2D array when the distance b of the image plane to the lens is increased, both for the collimated-beams case ($p = 0$) and the defocused case ($p = 0.21$). The design assumptions for this were a spot diameter $D_{spot} = 12$ cm at room height $b_0 = 2.5$ m, and $M = 196$ ports. Clearly by means of defocusing the dependency of the fill factor on the distance b to the lens is reduced.

6.3 Chapter conlcusion

In the first part of this chapter, an AWGr steering concept is presented. Based on a high port-count arrayed waveguide grating router with its output fibers arranged in a 2D array and a high-speed lens, individual wavelength-controlled 2D steering of narrow infrared beams can be realized. Thus many ultra-high capacity wireless links for high-bandwidth wireless services can be created. Capacities up to 35 Gbit/s NRZ-OOK and 112 Gbit/s 4-PAM per beam with a reach beyond 2.5 m have been shown. With an 80-ports C-band AWGr, a total wireless system throughput beyond 8.9 Tbit/s can be achieved. By extension to a 192 ports (= 96 + 48 + 48) 3-elements composite AWGr operating in C- and L-band, throughput volumes beyond 21 Tbit/s become feasible. The second part of the chapter showed how, by applying a defocusing technique, the size of the passive beam steering module is decreased considerably without affecting the system?s performance.

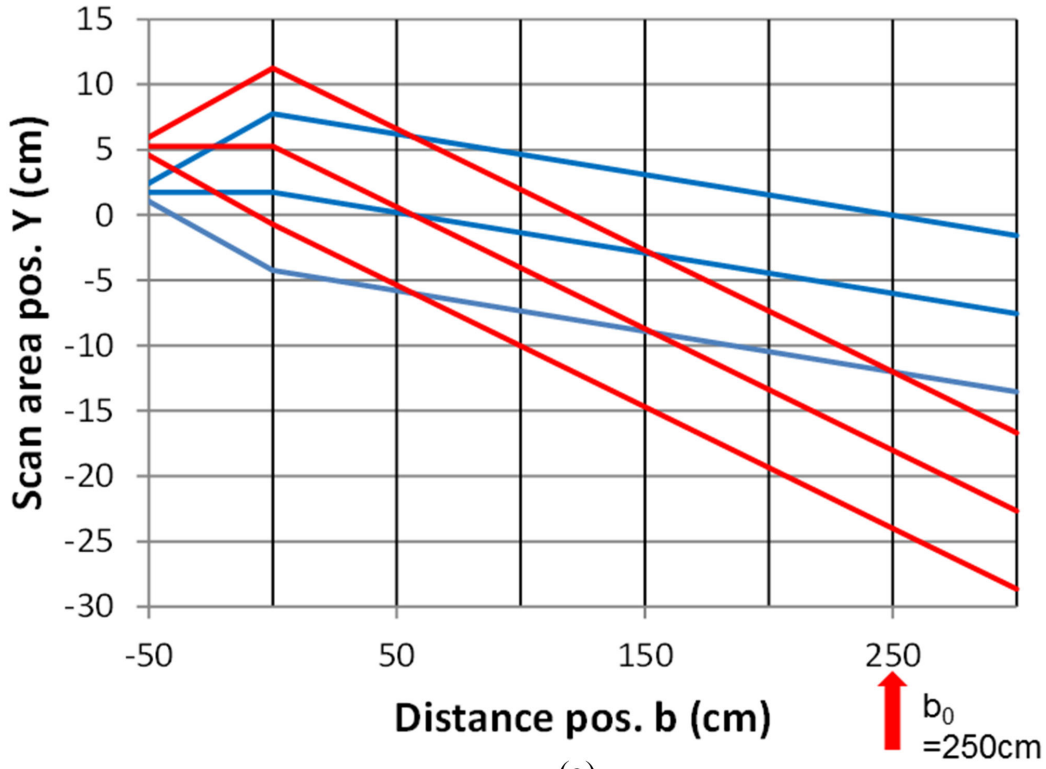

(a)

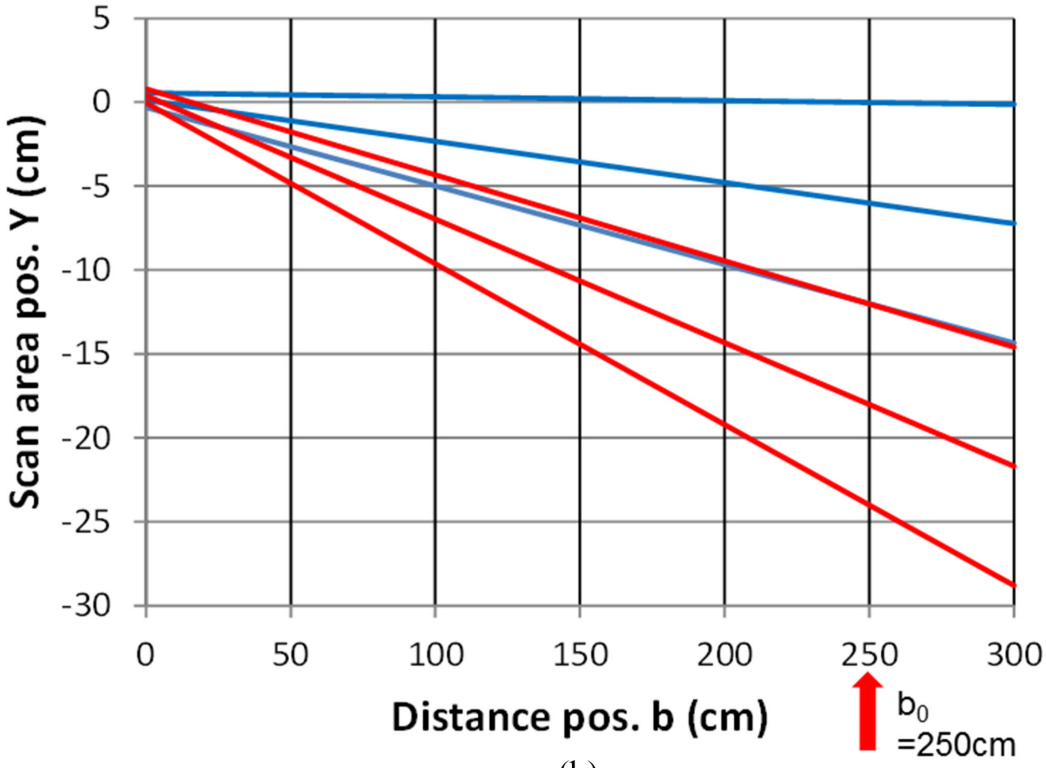

(b)

Figure 6.6: Impact of defocusing on the beam profiles (a) without defocusing (p = 0) and (b) with defocusing p = 0.21.

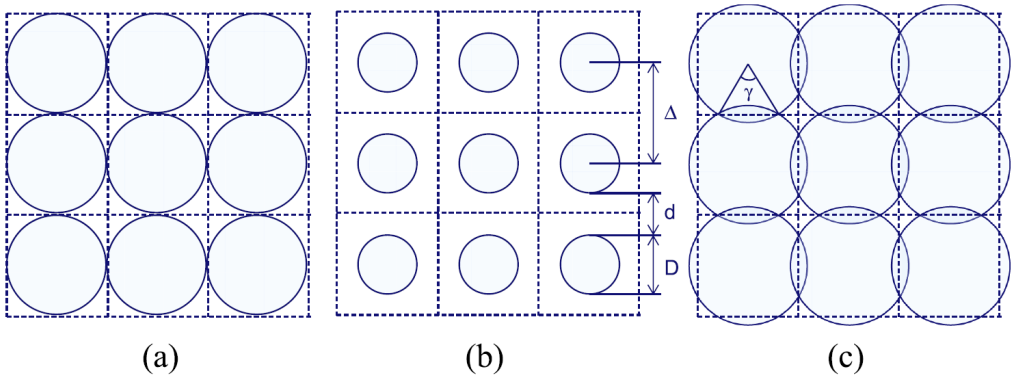

Figure 6.7: Filling the image area by the beam spots. (a) No spacing between spots ($D = \Delta$). (b) Spacing between spots ($D \leq \Delta$). (c) Overlap between spots ($D > \Delta$).

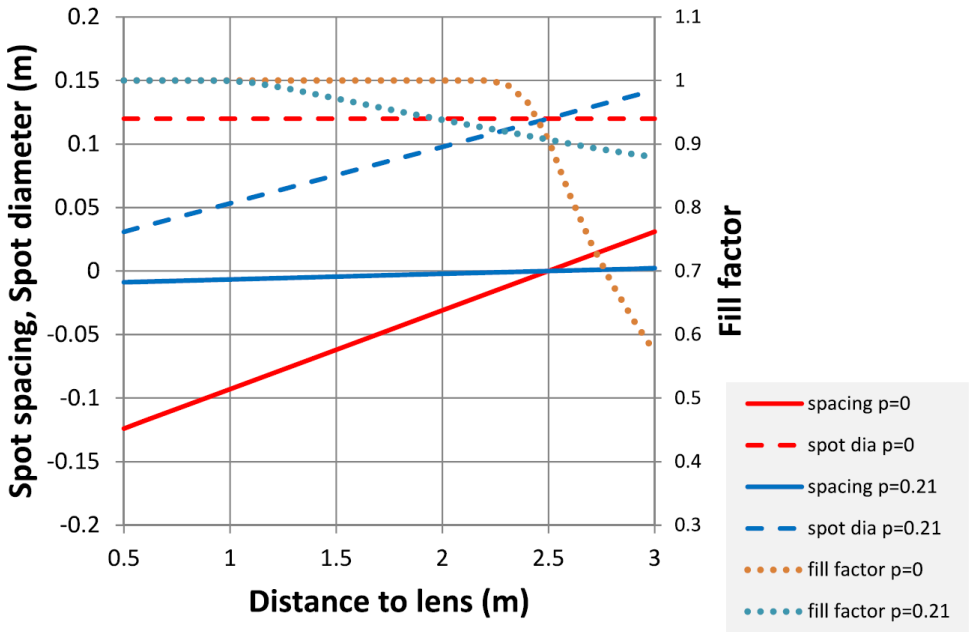

Figure 6.8: Improving the area fill factor by defocusing.

Chapter 7

Localization

The extremely high performance possible thanks to the BS-ILC can only be achieved with high directivity of the antenna, that is, small beam size, and ultimately, small footprint. This means that the system needs to know the exact location of user devices with respect to the light antennas. There are a variety of localization techniques developed over the years that employed radio [122] and light signals [123]. All these works have resulted in accuracies in the order of tens of centimeters, require relatively high power, slow localization for multiple targets and, not less importantly, complex structures. Furthermore, radio based localization are susceptible to EMI. An interesting approach was proposed exploiting a camera-based localization technique [124] where LEDs for user tagging were used leading to a localization accuracy of several millimeters. The high accuracy was obtained using 12 infrared LEDs encircling the detector, required 100 images for processing, and the use of an infrared camera. All this leads to high power consumption, long processing time, and high costs [125]. In this chapter, the problem of localization will be carefully addressed. Because the setup used for communications is slightly different than the one used for localization, a brief description of the new setup is given at the beginning of this chapter. Considerations on the accuracy and latency of localization will be finally discussed.

7.1 Setup Description

The setup that has been used to evaluate the camera based localization consists of:

- a pc, that plays the role of the CCC, that decides where there are devices and so where to turn on an optical beam. The pc communicates to an arduino through a COM port

- an arduino device, responsible for converting the protocol used by the pc, which is Universal Asynchronous Receiver-Transmitter (UART), to a protocol compatible with the tunable laser, in our case Inter Integrated Circuit (I^2C), because the pc does not support natively the protocol I^2C via USB.

- the tunable laser, which receives the signal from the arduino device and turns on one wavelength at a time. The output power of the tunable laser is about 0.16 mW, approximately equal to -8 dBm, from the well known formula

$$P[dB] = 10\log_{10}(P[W]) \tag{7.1}$$

  or, similarly:

$$P[dBm] = 10\log_{10}(P[mW]) \tag{7.2}$$

- the fiber that comes out of the tunable laser then goes through an amplifier, in order to have the maximum optical power transmitted by the antenna in compliance with the safety regulations. As discussed in the first chapter, the maximum possible transmit power P_{TX} is 10 dBm, but, because 6 dB are lost in the antenna itself, the output power of the amplifier is 16 dBm.

- the fiber from the amplifier goes to the antenna, that spreads the optical beams depending on the wavelength used. Please see Chapter 6 for information on the antenna used. The serving area of the antenna is placed on a table, perpendicular to the orientation of the antenna itself.

- the optical wireless signal finally illuminates a photo diode, that acts as a detector. The photo diode has an output that goes directly to an oscilloscope. From the oscilloscope it's clear to see where and when there is a received signal, or power.

The system above described is the one used for localization and is shown in Fig. 7.1. The final system, for communication, is more complicated. In the above system, in fact, no signal is modulated, only a carrier is sent, at a frequency set by the tunable laser as decided in the pc (CCC). In order

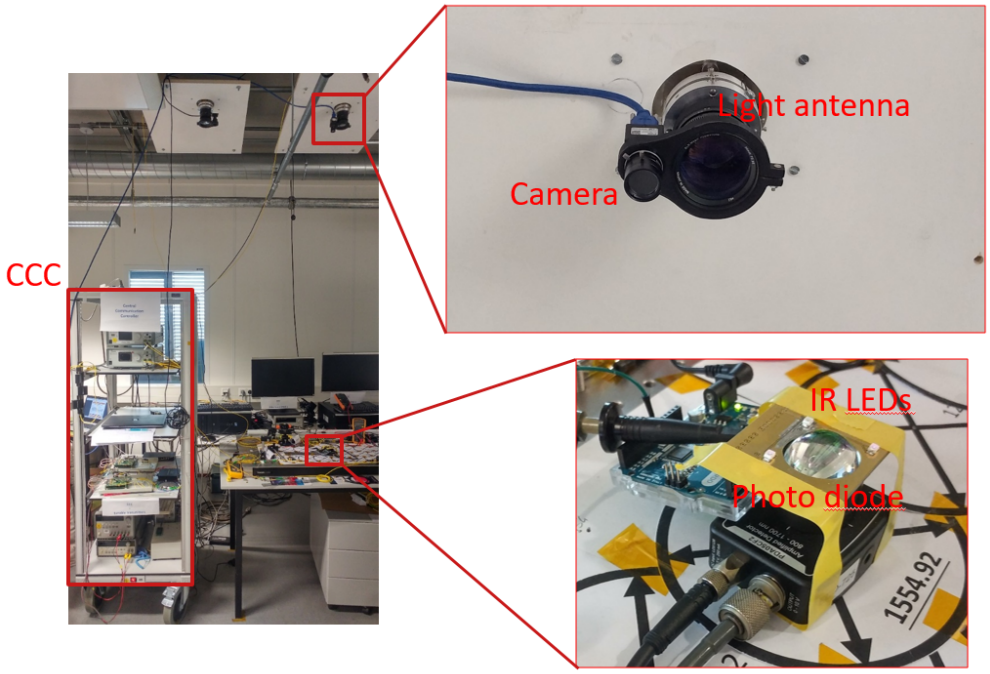

Figure 7.1: Picture of laboratory setup.

for the device to receive information, a modulated signal around that carrier needs to be sent. This is why, for each device, another pc is responsible for deciding which signal is needed, then, it gets converted to optical signaland sent to the tunable laser. The tunable laser is an SFP+ module, so it has two optical ports. One, as described, is the output that goes to the amplifier, and the other one is the input signal that the device wants to receive. The other input of the tunable laser, that comes from the CCC, is electric and sets only the wavelength to be used. The modulation happens here, in case of a transmitted signal is present.

However, for the sake of this project, a transmitted signal is not needed, a carrier is enough to understand if the localization technique is working properly. Because the unmodulated carrier is generated inside the tunable laser, the PC that is responsible for sending the required signal (information) to the device is turned off.

At the receiver side, for the same reason, a photo diode is enough, which converts the optical beam to an electric signal sent to the oscilloscope, that tells us when there is power received. A collimator that conveys the optical

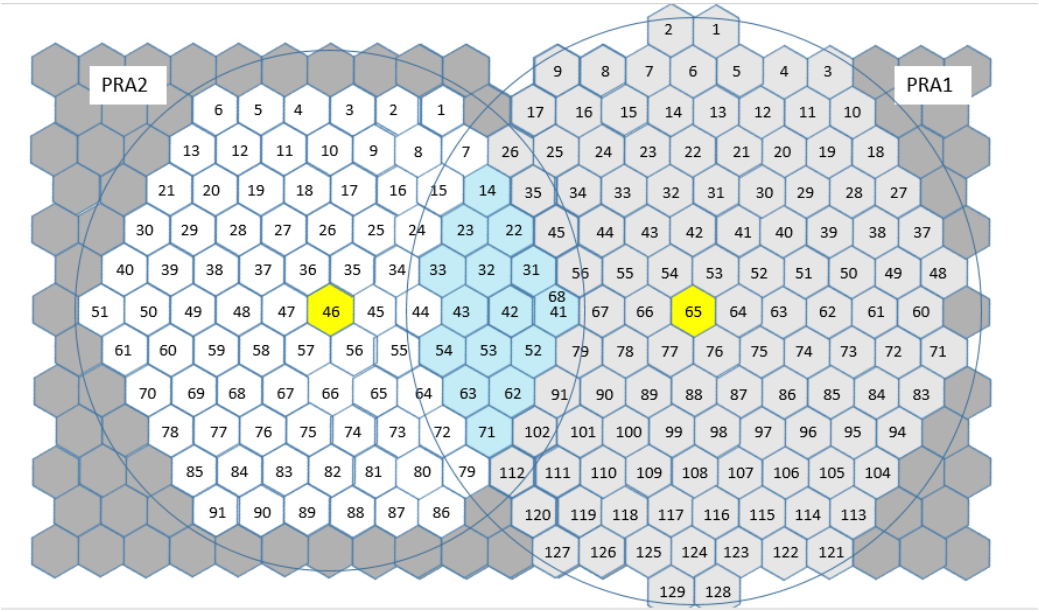

Figure 7.2: Scheme of serving cells of the two PRAs.

beam inside a fiber, necessary to emulate a device that then transforms and demodulates a signal, is not necessary here and would cause other problems, due to today's technology, mostly a much smaller receiving angle (higher directivity) than the photo diode. The problem of the too high directivity has already been addressed in the previous chapters.

The overall system is more complex, having 2 tunable lasers, an optical switch, and 2 antennas (PRAs), each with its own serving area, composed by 86 and 128 cells, of which 15 cells overlap. The scheme of the serving cells is shown in shown in Fig. 7.2. This way, each tunable laser can be used to serve users in any antenna, and researches are possible in case of antenna handover, so in those cases in which a user is moving from the serving area of one antenna to the other one, with the possibility of being served by 2 antennas at the same time when the device is in the 15 overlapping cells.

In Fig. 7.2, the serving areas of the twe antennas are shown, and the overlapping cells are highlighted. The antenna that is being used for transmission is the PRA1, while the camera is placed right next to PRA2. This is not a problem, in fact the FoV of the camera is so wide, that it is including both the FoV of the 2 PRAs. However, not the whole serving area of PRA1 is usable. In fact, due to the narrowness of the receiving angle of the photo diode, only cells close to 65 are usable. All the experiments performed are

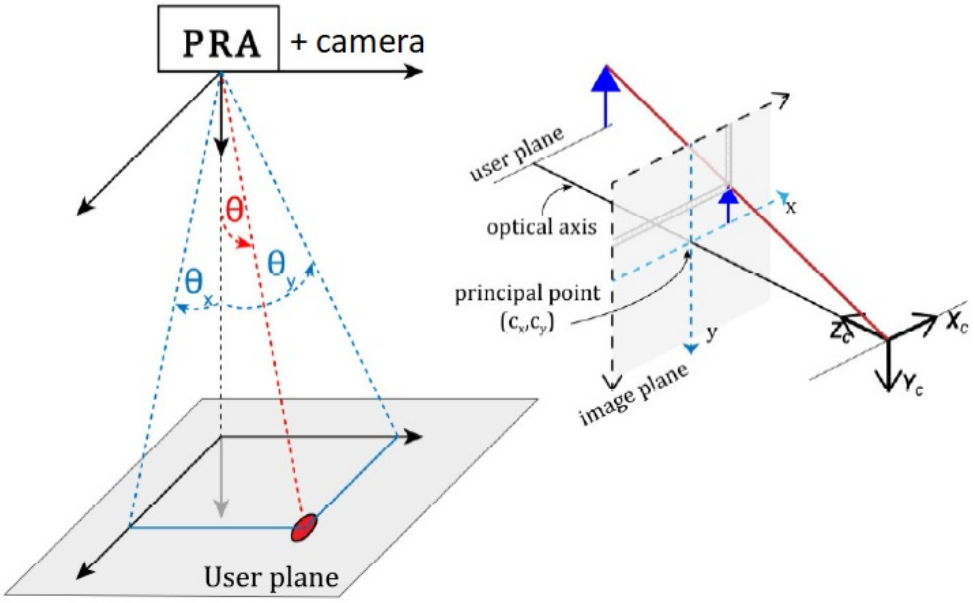

Figure 7.3: Steering angle from PRA and camera to user. On the right, camera pin hole model

made with the photo diode placed in these positions because it's the only way it can receive power.

7.2 Camera Based Localization

The system setup described earlier does not take into account the camera's position and functionalities. That's because the system is actually independent on the localization technique used. The CCC understands where the device is located, and so turns on one specific wavelength, that illuminates a certain area (cell) in the surface of the table. If the localization technique were different, nothing would change in the system described earlier.

The camera based localization has the advantage of low cost with respect to other localization techniques, and offers a much better accuracy. Power consumption is kept low in particular at the dongle side, that is the most critical aspect. The camera position is not necessarily important, as long as a 3D localization is performed. In order to keep complexity as low as possible, and save unnecessary expensive installations and tuning needs, a 2D localization is sufficient as long as the camera is oriented in the same

direction of the antenna, and is placed very close to it. In this way, both the antenna and the camera are seeing the same thing, the area to serve, and possibly the camera can have a much wider Field of view. The distorsion that necessarily happens at the edge of the camera field of view, happens outside of the serving area of the antenna, so no distorsion is present in the whole antenna serving area.

By connecting the camera to the CCC, a conversion from the position to the wavelength can happen in the CCC itself, and this function can happen fast enough to provide signal where it is needed within the smallest delay possible, in the order of milliseconds. This is the idea behind this localization technique, that will be carefully described in the following.

7.3 System design and experiments

The camera that is used in the first experiments is a cheap camera, it costs around 60 euros, and not many information can be found about it. It can work at HD resolution (1280x720) at 120 frames per second (fps), FullHD resolution (1920x1080) at 60 fps, or lower resolution (640x360) at 240 fps. In practice, these numbers have proven to be optimistic, about 20% lower frame rates are to be expected during the experiments.This camera receives waves in the visible spectrum, as well as in a portion of the infrared spectrum, until about 990 nm, equivalent to a frequency of $\sim$ 303 THz. A filter is placed in front of the lens of the camera, in order to receive only in the IR band. This way, the camera sees nothing unless there is an IR LED, that uses a frequency higher than 303THz, turned on in its Field of View. The IR LEDs used in this case are using a wavelength of 950 nm.

The device on the table, which is the photo diode in this case, is equipped with another arduino, responsible for turning on 3 of these IR LEDs, placed around the lens on the photo diode itself. The number of IR LEDs is irrelevant in this stage, and will be discussed later, the important thing is that the camera is able to detect the exact position of the center of the lens of the photo diode, in order to have the most accurate localization. The accuracy depends on the resolution of the camera, on its FoV (which depends on the zoom eventually applied), on the distance between the camera and the device surface (table). In order to detect the position of the center of the lens, at least 2 IR LEDs are needed, placed simmetrically around the lens.

A new camera, with a cost of about 250 euros, has been purchased and will

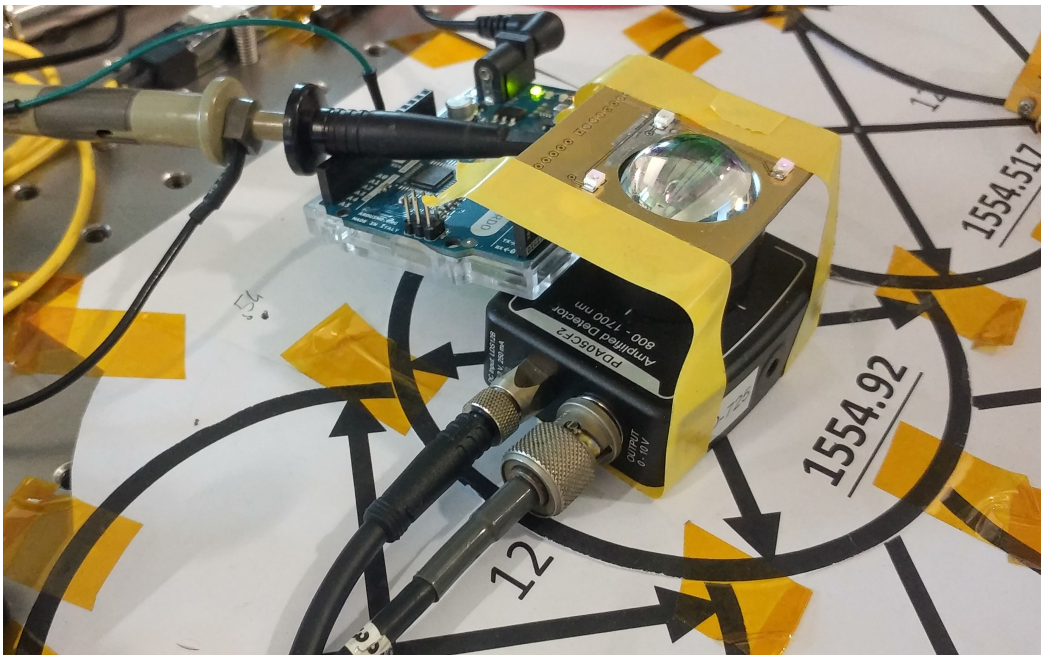

Figure 7.4: Detail of the photo diode and the arduino controlling the IR LEDs placed around the lens.

be later installed and tested. Results will be then compared.

7.4 Hardware Limits

No expected results can be set without knowing what are the hardware limits. In this section, a few experiments are reported to understand where improvements could happen, and where the limits are set by other equipments, and, finally, to understand if it makes sense to use a different camera for our purpose.

As mentioned earlier, the whole final localization technique will consist in a device that turns on some IR LEDs, a camera that senses them, a pc that converts the information from each frame into information on a position, and then sends a signal to the tunable laser to turn on one specific wavelength. Every process introduces a delay, that has to be known in advance in order to provide a strong and reliable localization.

First experiment

The first experiment aims to understand if the tunable laser introduces a delay on its own, from the moment it receives the command to turn on one specific wavelength. The arduino that sends commands to the tunable laser is reprogrammed, to turn on and off periodically the tunable laser, with a period of 20ms and duty cycle = 0.5, with a wavelength corresponding to cell 65.

As mentioned earlier, cell 65 is used because it's the image center of the antenna.The main advantage is that the optical beam travels in a direction perpendicular to the surface of the table, and so, the photo diode, that has the lens parallel to the table, receives the highest possible power. This happens because the photo diode has a small receiving angle, in the order of a few degrees, despite it being much wider than a collimator (collimators require days of manual tuning to be directed exactly in direction of the optical beam, because their FoV is too low, about 0.034°). This would not be a problem if we had a wide angle receiver. Please refer to Chapter 4 for more information regarding wide angle receivers. Cell 65 and its adjacent cells are the only ones that could be used for all our tests. It's important to note, however, that this limit is due to the photo diode itself, while the whole localization process works without problems in the whole serving area.

Results of this test can be seen in Fig. 7.5, where we see in the oscilloscope the power received by the photo diode. The period is still of course 20 ms, but the duty cycle is lower. That happens because the tunable laser turns off the wavelength as soon as it received the command to do so, but ~ 5 ms are required to turn it on.

Second experiment

The delay introduced by the tunable laser itself is now known. The delay introduced by the CCC is evaluated in a similar way, still connecting only the photo diode to the oscilloscope, but setting the arduino back to its original scope (convertin protocols) and setting the duty cycle via software in the CCC. In this way, also the delay eventually introduced by the arduino for the conversion is empirically measured. The software used in the CCC to control the tunable laser (to send commands to the arduino and then to the tunable laser) is LabView. The same results have been shown, indicating a

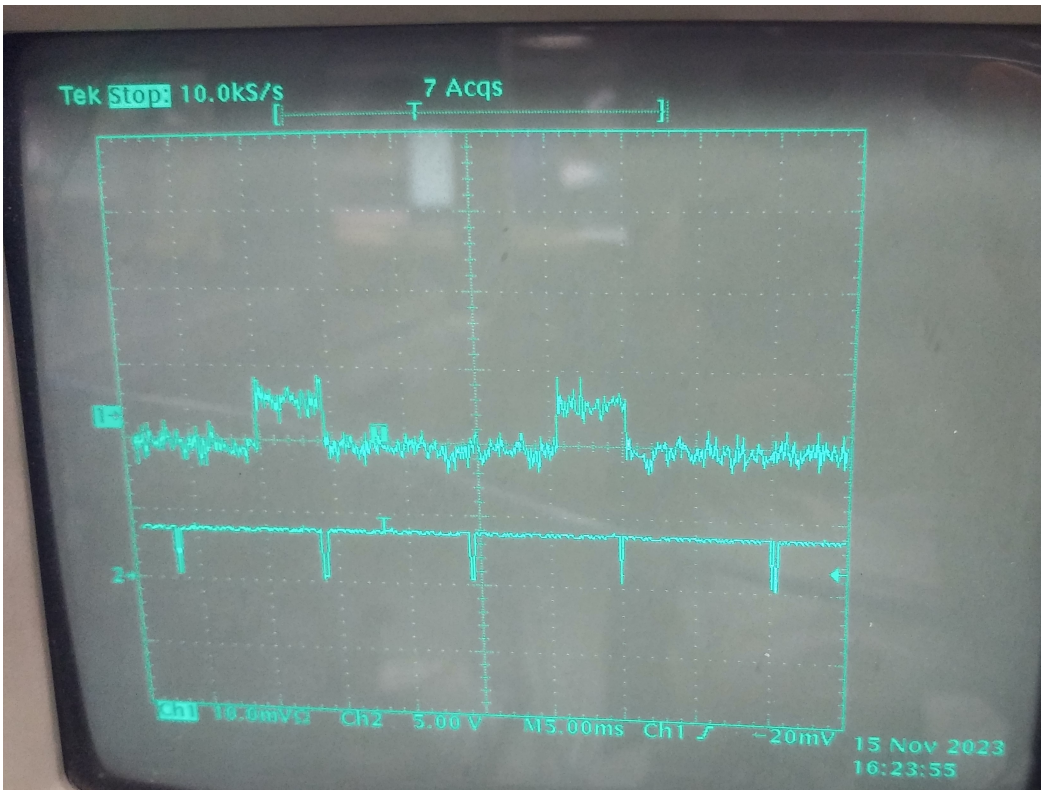

Figure 7.5: Output of oscilloscope. Channel 1: received signal from photo diode. Channel 2: commands sent to the tunable laser.

delay introduced by both operations in labview and arduino much smaller than the 5 ms introduced by the tunable laser. This is a good result because we don't have to worry about the delay introduced by these devices, as long as the tunable laser does not change. There is also room to improve the quality of the tunable laser, leaving all the rest untouched, to improve the overall performance of the system.

Third experiment

In this experiment the delay of the image processing has been evaluated. The 2 IR LEDs placed around the lens of the photo diode are blinking with period = 2s. The camera is recording and sending every frame to the pc. Because the camera has an IR filter in front of it, the camera records completely black frames for 1 second, black frames with 2 illuminated regions (the 2 IR LEDs) for another second, periodically.

Figure 7.6: Frame of the IR LEDs on, with infrared filter applied to the camera. Only 2 IR LEDs of the user device are turned on in this case.

In the PC, image processing is implemented in LabView, in which every pixel for every frame is analyzed. As recorder by the camera, every pixel is defined by 3 colors (red, green, blue) and by its position in the frame. The position consists in the coordinates of the pixel in the frame. The pixel illuminated by the IR LEDs have a very high red value, but relatively small green and blue values. For this reason, only the green value has been analyzed and compared to a threshold.

Another possibility for the image processing is converting every frame into gray-scale, and thresholding the white. Both cases have been analyzed, similar results have been obtained.

The 2 regions of illuminated pixels are then found. The program in LabView calculates the position (pixel coordinates) of the midpoint of the two regions, that corresponds to the center of the lens of the photo diode. In this early stage, no conversion from pixel coordinates to wavelength to be used in the laser is necessary, only the overall image processing delay is evaluated.

2 HD frames are saved in the pc, one for each state of this case: IR LEDs on and off. The Labview program is performing the image processing as described, on one of the 2 images saved, in loop, for 100 times, then the

same thing happens for the other image. A total of 200 images have been processed, and the time needed for it was about 460 milliseconds, as this is the period of the signal seen by the photo diode, as shown in the oscilloscope. This means, without a deep knowledge on the standard deviation, that every frame requires ~ 2.3 ms to be processed.

Improvements could be made, but as long as the tunable laser introduces a higher delay, image processing is considered to be fast enough.

7.5 Cell coordinates

As previously mentioned, the serving area of each antenna is divided in cells, and the camera needs to know the position of the center of each cell in order to turn on the (only) cell that can serve the user device. For the camera, positions are coordinates of pixel, that is why the camera has to be well fixed to the antenna. For the tunable laser, cells are only wavelength to be turned on. The pc is receiving information from the camera and sending commands to the laser whenever a change in wavelength has to be performed. From image processing the pc knows the position, in pixel coordinates, of the user device. Cell centers have been measured and reported in Table 7.1, and are to be compared with Fig. 7.2 of the tessellation of the table.

The camera has a field of view independent of the FoV of the antenna. In our case, the camera has a much larger FoV, and is installed close to another antenna. That is why the coordinates of each cell center, the cell 65 in particular, are not centered in the camera FoV, but rather translated on one side.

It is clear how well the camera has been aligned, the coordinates of the cell centers are very consistent.

The next step consists in measuring the distance between cell centers, both in the real world and as seen by the camera, to verify if the camera does not introduce distorsion, especially considering the device is not moving around the center of the FoV of the camera itself.

In the X direction the following measurements have been performed, by setting the camera to HD resolution. This resolution, in fact, has proved to be accurate enough for the localization process, and the frame rate is of major concern, so a higher resolution would bring more downsides than benefits.

The distance between cells 77 and 75 is measured to be 9.9 cm, and is 45 pixels in the camera. The distance between cells 54 and 53 is measured

Table 7.1: Cell centers coordinates

Cell number	(X , Y)
65	(249 , 357)
66	(292 , 358)
64	(205 , 358)
62	(120 , 357)
54	(268 , 399)
76	(225 , 313)
53	(223 , 398)
77	(270 , 312)
51	(140 , 397)
73	(100 , 312)
87	(205 , 270)
88	(250 , 270)
79	(296 , 270)

to be 9.9 cm, and is 45 pixels in the camera. The distance between cells 65 and 66 is measured to be 9.7 cm, and is 43 pixels in the camera. The distance between cells 77 and 73 is measured to be 40.0 cm, and is 170 pixels in the camera. (on average, $9.9/40 \cdot 170 = 42$). These results show acceptable consistency, but, as expected, a little distorsion as the device moves towards the edge of the camera FoV. Slightly different results have been seen in the Y direction: The distance between cells 65 and 88 is measured to be 17.1 cm, and is 87 pixels in the camera. The distance between cells 66 and 89 is measured to be 16.7 cm, and is 88 pixels in the camera. The relation between pixel dimension and distance is different in the Y direction, in fact: $88/45 \cdot 9.9 = 19.36$ cm, not $\sim$17.0 cm. This is due to a different focal length in the X and Y direction, inside the camera.

This is not a surprise. In fact, by measuring the exact dimension of the field of view of the camera, in the table plane, it's clear that the ratio between the two dimensions is not precisely proportional to 1280/720, that is the resolution of the camera used in this case. Instead, the dimension of the FoV takes into consideration also the different focal lengths.

It's interesting to note that, from a geometrical point of view, the dis-

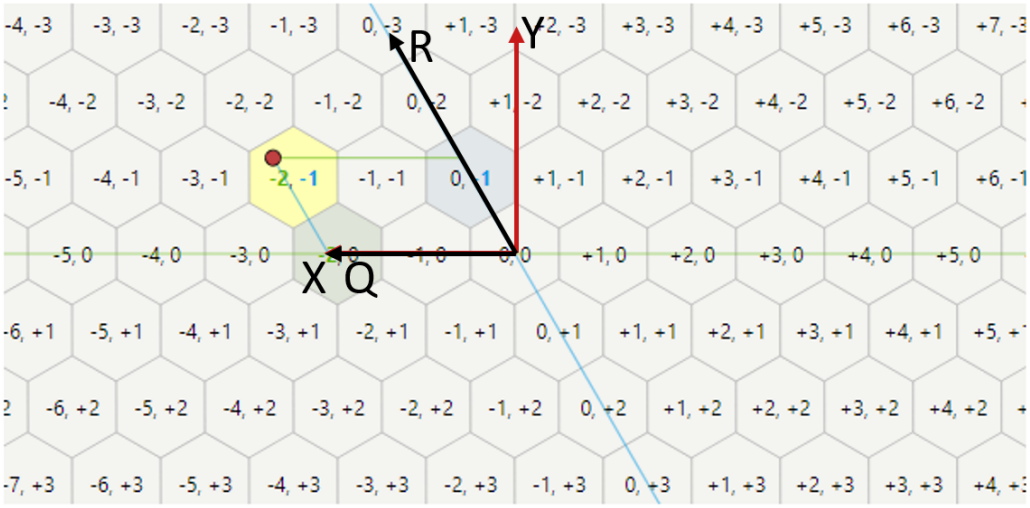

$$\begin{bmatrix} x \\ y \end{bmatrix} = size \times \begin{bmatrix} \sqrt{3} & \sqrt{3}/2 \\ 0 & 3/2 \end{bmatrix} \times \begin{bmatrix} q \\ r \end{bmatrix}$$

Figure 7.7: Graph of the change of reference system. Coordinates Q and X coincide, while R and Y do not.

tances in cm measured are correct, it's only the relation with the distance in pixels in the camera that is changing. In fact $\sqrt{3} \cdot R = 9.9$ cm $\Rightarrow 3R = 17.1$ cm approximately.

It's important to note also, that the accuracy of the system is in the order of millimeters. If 9.9 cm are equivalent to ∼45 pixels, then ∼2.2 mm per pixel are projected on the table. The accuracy is really high because the camera is working in HD an has a relatively small FoV.

As shown in image LABEL, the tessellation of a plane in hexagons is the best option for the PRA antenna, but it's not feasible to be compared with X and Y coordinates directly. If that were the case, more calculations would have ot take place for every frame process to determine the serving cell. For this purpose, a new reference system has been set in order to minimize as much as possible the complexity of the processing, and so reduce the processing time. The new reference system is (Q,R), not (X,Y) anymore, as shown in Fig. 7.7

Because the R direction takes into account both focal distances in X and Y

directions of the camera, different distances in pixel have to be set between 2 adjacent cell centers in the 2 directions.

Distance between 2 adjacent cell centers in the Q direction = 9.9 cm = 45 pixels in the camera. Distance between 2 adjacent cell centers in the R direction = 9.9 cm = 49 pixels in the camera.

7.6 Chapter conclusion

In this chapter, the localization setup has been presented. The main challenges regarding the conversion between the camera images and the information sent to the tunable laser have been discussed. The camera based localization proved to be very accurate at the HD resolution. Another advantage brought by this technique is the use of IR LEDs at the receiver, because they are small, light, cheap and their power consumption is lower than the equipment needed for other localization technique. To improve power consumption even more, rules could be set on the duty cycle of the LEDs at receiver side, that may not need to have always-on LEDs while not moving. In the next chapter, a deeper look regarding the delay introduced by the whole localization process will be addressed.

Chapter 8

Device Position Prediction

In this chapter, the delay problem is carefully analyzed and possible solutions are reported, highlighting advantages and disadvantages for each of them.

8.1 Camera Delay

While making experiments with the hardware available, a delay of about 100 ms has been proven to come from the camera itself. While performing image processing in loop on the same saved image, in fact, only the processing time for each frame has been measured, not the delay coming from the camera. In an ideal case, as soon as the camera captures a frame, it sends it to the PC, to be elaborated. Whatever the frame rate of the camera, as soon as a new frame is received by the PC, the pc processes it and sends a command to the tunable laser, as long as the processing time is lower than the frame time (which has been proven to be the case in all the experiments performed). Unfortunately, a delay of $\sim$ 100 ms has been measured between the moment the camera captures a frame, and the moment that frame is received by the PC. Changes in cables, camera and PCs have been performed to confirm that. Every setting of the camera has been deeply analyzed, for example the type of video compression used by the camera (mjpg is to be favorite because in this case every frame is a jpg image, independent on all the other frames, that is better for latency reasons).

A possible solution may be lowering the resolution of the camera. This way, the processing time for each frame has been proven to be $\sim$0.5 ms

(against ∼2.3 ms for the HD resolution), but most importantly, the latency introduced by the camera is lowered to ∼30 ms, much lower than the HD case (∼100 ms). However, the same FoV at a lower resolution implies a lower accuracy, which has been proven to be acceptable for localization only, but not for identification.Latency is always to be expected when using a camera, but in this case the latency is about 10 frame times long, whereas it should be ~ 3 frame times long in a cheap camera and ~ 1 frame time long in modern, more expensive cameras. Whether or not a new camera solves the problem, while working with these high delays, relying on prediction algorithms is a must. These algorithms will be discussed in the next sections.

8.2 Prediction algorithm

Because of the intrinsic delays of image recording and processing, in order to serve the user device at the actual position, a prediction algorithm must be developed. However, the complexity of it is hardly dependent on the amount of prediction time needed. In other words, lowering the overall delay means lowering the prediction time, and this would affect positively the simplicity of the prediction algorithm.

Another aspect to be kept in mind, is that the prediction algorithm must be run every time there are new information on the user device position, that is, every frame time, in order to keep the actual position up to date. Because the frame time is low, in the order of milliseconds, and the computational power in the CCC is limited due to cost, dimension and cooling reasons, the complexity of the prediction algorithm cannot exceed a certain limit. On average, the processing time for an HD frame is 2.3 ms, that is still lower than the frame time (at HD, frame rate is $\leq$ 120fps $\iff$ frame time $\geq$ 8.3 ms). This means that the prediction algorithm can never take place in more than 6 ms, and more stringent time constraints must be respected in order to be sure never to loose any frame.

The first and simplest attempt of prediction algorithm, in this case, consists in assuming uniform linear motion of the user device, for the whole period of time to be predicted. In this way, only two positions, and relative time instants, have to be evaluated for each iteration, not necessarily belonging to adjacent frames. Of course, every time one acceleration will be present, either because of linear accelerated motion, or because the trajectory is not linear, an error on the predicted image will occur. This method, therefore,

works better the more accelerations are low, and in a device that is moving on a table, this may be the case. For obvious reasons, the frame rate of the camera is of major importance in this case.

$$v_{est} = \frac{\sum_{i=1}^{n-1} \alpha_v^i \cdot v_i}{\sum_{i=1}^{n-1} \alpha_v^i} \tag{8.1}$$

$$a_{est} = \frac{\sum_{i=1}^{n-2} \alpha_a^i \cdot a_i}{\sum_{i=1}^{n-2} \alpha_a^i} \tag{8.2}$$

$$x_{est} = x_{n-1} + v_{est} \cdot \Delta t + \frac{1}{2} \cdot a_{est} \cdot \Delta t^2 \tag{8.3}$$

Equations (8.1), (8.2) and (8.3) show a general behavior of the prediction algorithm. These calculations are performed for both the directions Q and R. x_{est} is the estimated future position. Even if it looks like the equation of a uniformly accelerated motion, v_{est} and a_{est} are not the measured speed and acceleration. They are values of speed and acceleration used for the algorithm to predict the future position in the best way, taking into consideration a bigger history than only 2 or 3 old frames. There is a window of n values of old recorded positions. For each two adjacent values, a speed v_i averaged on the time difference between the values, is considered. A speed coefficient α_v weighs the importance of each measured speed v_i. The speed coefficient is lower than one, and is raised to i power, so that the last measured speed has a bigger impact on the estimated speed and so, finally, on the estimated position, in order to give less importance to older information. The denominator normalized the quantity obtained. Similar considerations can be made for the acceleration. Every coefficient used in this formula are to be set properly for obtaining the best prediction algorithm. Considerations on these coefficients will follow.

When the lowest resolution is used, the frame rate is ∼250 fps, that corresponds to a frame time of ∼4 ms. The position detection accuracy depends on the resolution of the camera. An error in the position detection is intrinsic of this process. This means that even a standing device, may appear moving in time, from one pixel coordinates to another, in different processed frames. A prediction algorithm that relies only on these information will amplify the error when predicting the future position, because the measured speed of the device may differ from the real one, due to a mistake of the read position coordinates of one of (or both) the 2 frames analyzed.

The more time pass between 2 analyzed frames, the more this error will

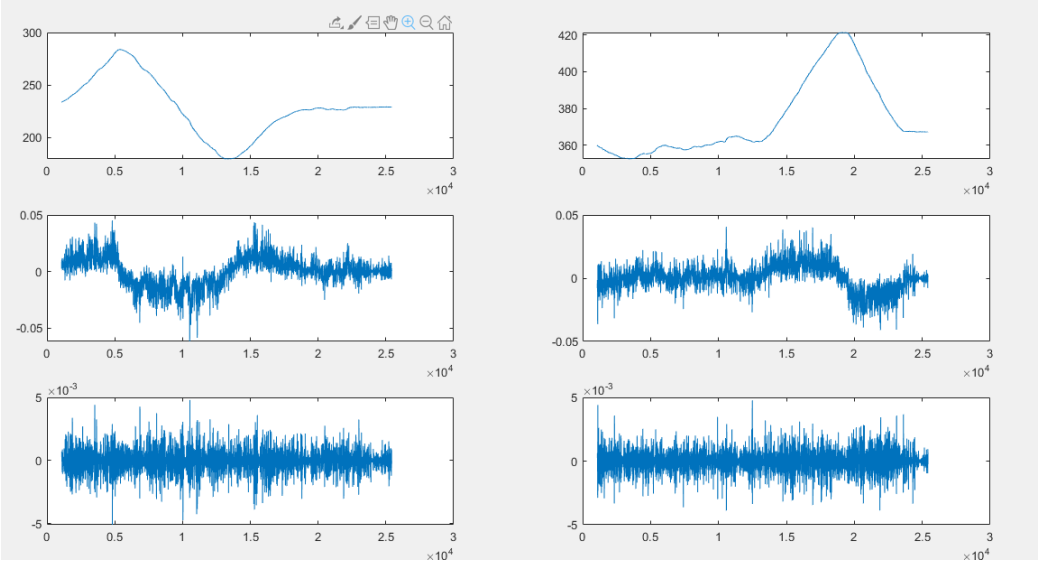

Figure 8.1: On the left column, from top to bottom, the graphs of position, speed, and acceleration with respect to time in the Q direction. On the right column, the same graphs in the R direction. The noise coming from derivation is clearly visible.

fade away, but the more acceleration will affect negatively the assumption of uniform linear motion. A trade-off must be found, between waiting more time between analyzing 2 frames (so predicted speed will be closer to reality, but acceleration changes more the results) and waiting less time (predicted speed may differ, but acceleration is less influencing). That is, how much acceleration can affect our system. In the range of accelerations that the user device can have (that must be measured), what is the best scenario. In other words, how much our prediction algorithm, along with its assumptions, is far from reality.

More complex algorithms have been implemented and studied. Without the assumption of uniform and linear motion, accelerations must be studied. When taking into consideration a bigger history of the user positions, for example 3, the acceleration can be measured. The increasing complexity of the mentioned algorithm is not the only downside: a longer history of tracked positions is, by definition, older information about the user device position. The prediction algorithm assumes that the acceleration will be constant for the whole prediction time. Even if the acceleration could be highly precisely measured (that requires a higher frame rate and a higher

space resolution), the variation in time of the acceleration has to happen more slowly than the time needed to measure the acceleration itself, plus the predicted time. When four or more past positions are analyzed, even the evolution in time (derivatives) of the accelerations can be evaluated, but the problem of assuming one value (for example the derivation with respect to time of the acceleration) constant for the whole predicted time is still present.

A flexible prediction algorithm has been made, taking into consideration all the above mentioned aspects. Coefficients can be changed in order to have a bigger history, give more importance to acceleration or speed, and many other aspects can be changed. As expected, different algorithms work better in different situations, or in different time intervals. The best overall algorithm has been evaluated nonetheless. A few aspects of the prediction algorithm are now discussed.

8.3 Space resolution

The space resolution turned out to be a bigger problem than expected. As shown in LAST picture, fluctuations on the speed are extremely high even if the position plot seems easily derivable. These fluctuations are amplified even more in the acceleration graph. That is because the derivative is intrinsic noisy process, so a second derivative is noise upon noise.

A longer history needed to be taken into account to filter out the noisy data on localization, even if that implies dealing with older information, and so, relying more on the prediction algorithm itself.

The delay that is coming from the camera is by far the highest delay that the prediction algorithm has to counter effect. Because this delay is much higher than a frame time, about 10 times higher, an error in the speed estimation may be dangerous in the position prediction.

8.4 100 ms

The prediction algorithm cannot predict 100 ms when samples are 10 ms far from each other, if movements change faster than 100 ms. Movements change when accelerations last, and if they last less than 100 ms, no prediction can consider it.

Both the noise coming from the derivation and the fact that accelerations

can last shorter than the predicted time, sometimes even less than a single frame time, are the two major reasons for which the prediction algorithm relies more on the speed than the acceleration. This way, some overshoot is to be expected when accelerations take place, but good estimations are performed during uniform linear motions. Slightly more importance is given to the last read frame in order to make the overshoot last as short as possible.

Fig. 8.2 shows clearly the overshoot that comes from the prediction algorithm. The more the algorithm counteracts the delay of the overall process, the more overshoot is present in the predicted position in case of acceleration. Because the speeds reached by the user devices are usually low, in the order of a few m/s, and considering there is overlapping between cells, the algorithm can in some cases lower the prediction time, in order to have less overshoot. Trade-offs need to be established even in this case. It all depends strongly on the the kind of movement that the algorithm needs to predict, so possible movements of devices on a table have been carefully analyzed, and ranges of speeds and accelerations have been measured.

8.5 Cell handover

Independently on the accuracy of the prediction algorithm, when the CCC assumes that a device has moved to a different cell of the serving area (not necessarily of the same PRA), cell handover must be performed in order to keep the connection up. Because each tunable laser can turn on only one wavelength at a time, if one tunable laser is associated to each device, cell handover can be performed simply by turning off the old serving cell and turning on the new one, serving the updated position of the user device.

If the hypothesis of one laser per user is denied, another possibility to perform cell handover, is to turn on 2 adjacent cells at the same time. The idea is similar to the Soft Handover of the 3G cellular network, but with a substantial difference: the difference in wavelength between two cells is about 0.5 nm, so there is no device able to distinguish the signal coming from two different cells.From a coverage point of view, if we analyze only the received power, this is possible and easy to implement, but measurements need to be done. Unfortunately, in this setup these measurements couldn't be performed, because the only other tunable laser used, is connected to an adjacent antenna, with its own serving area, divided in cells. As mentioned in the setup description, there are overlapping cells belonging to different

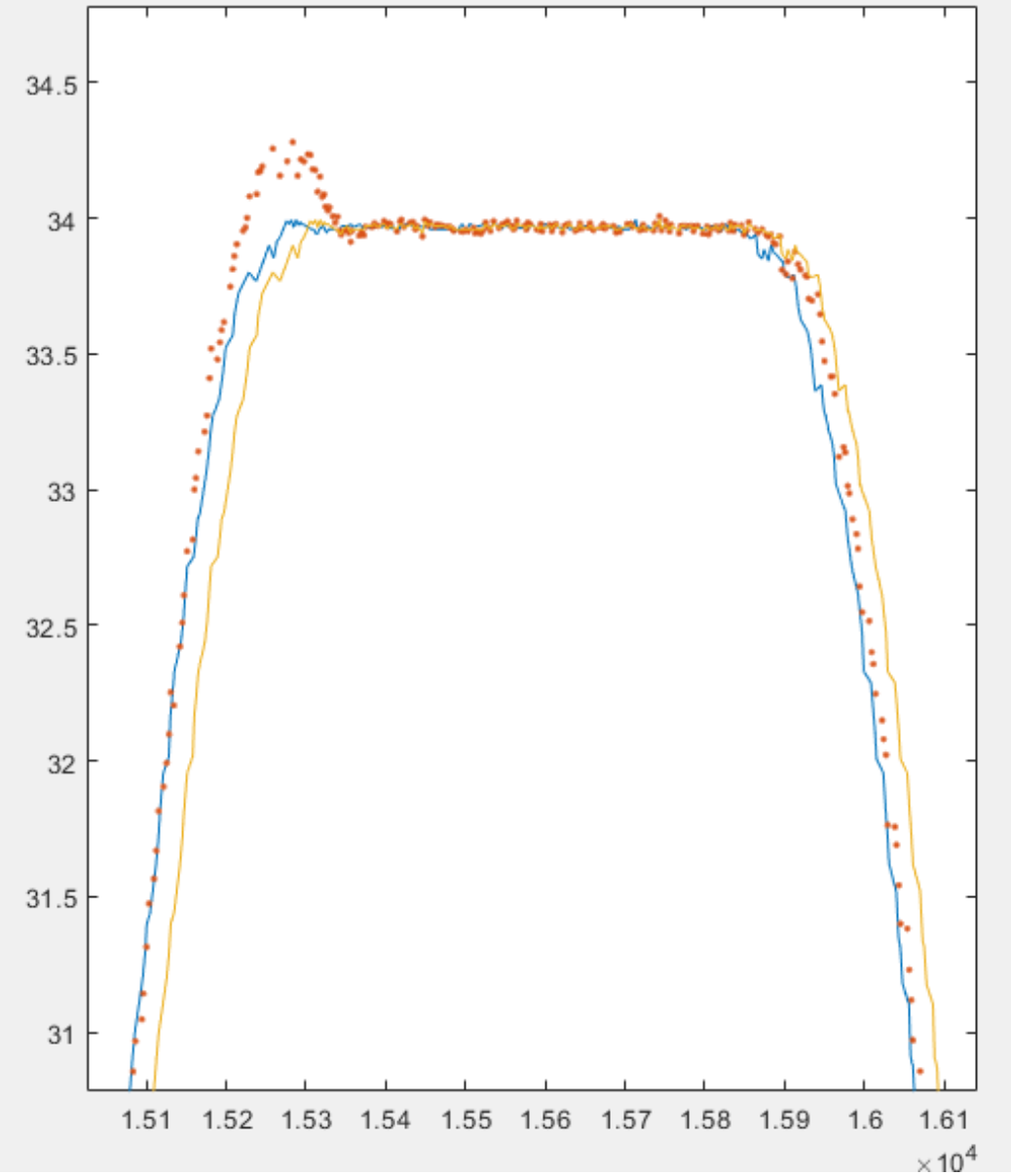

Figure 8.2: Detail of the output of the prediction algorithm. In the ordinate axis, the position in cm in Q direction, in the abscissa the time in ms. The yellow line shows the old information on the position, available to the CCC, the blue line shows the actual position, the orange dots show the predicted position. Particle of the overshoot when acceleration is present.

antennas, but they are at the edge of their serving area, and even the photo

diode is too directive to receive power in those positions. Furthermore, controlling interference coming from not only adjacent cells, but cells that belong to different antennas, may be even more difficult. Even if it were possible, it's important to underline that tunable lasers and modulators are expensive equipments. If more than one tunable laser has to be associated to each user device, the cost of the overall system may be really high.

In a flexible setup, and if no destructive interference is present in overlapping portions of cells, more than one tunable laser could be associated to one user device, when less than the maximum number of devices is present in the overall serving area. One algorithm could calculate the probability for each (adjacent) cell to be the next serving cell, and turn on the cell with highest probability of being the next elected serving cell.

Another problem to be addressed in this case is the limit on the transmit power, so if two cells at once are turned on for the same user, they are both transmitting at half power, so during a handover between two cells, even lower received power would be experienced by the receiver (not only because it is approaching the cell edge, but also because each cell has lower transmit power), but a never 0 received power could happen. Even more oscillations will come from multiple users served by the same PRA.

8.6 Chapter conclusion

The problem of the delay has been analyzed in all its aspects. A possible solution to counteract this effect has been presented, as a prediction algorithm. The main advantage of this approach is the flexibility of this algorithm, that can be easily changed in different scenarios, for example when a different camera is used. Different filters can be implemented to perform the best decision depending on the environment. However, because the delay is higher than the usual duration of accelerations in our scenario, the prediction algorithm can in some cases result in even worse performance than no prediction at all. A trade-off between all the possible applications has been proposed, and remains open to possible improvements in case the delay is made lower.

Conclusions

The radio frequency spectrum is becoming overcrowded thanks to the widely used wireless devices, and the Internet of Things will make things even worse. Traffic generated indoor is already higher than outdoor. Optical Wireless Communication (OWC) is seen as a complementary solution to this problem, implementable easily in indoor environments. Optical wireless can benefit from inherent wide bandwidth, immunity against electromagnetic interference, unregulated bandwidth. The technique presented in the first chapters of this thesis consists in a method to direct narrow infrared beams to different devices in a room, individually, simultaneously and dynamically. Beam steering modules, called Pencil Radiating Antenna (PRA)s, are used, bridging the gap between end-users and the fiber infrastructure. This will bring high speed, low latency communication to end user devices, as long as the Line of Sight (LOS) condition is preserved. The drawbacks of this system are in fact carefully analyzed to understand where future studies will need to focus most of their attention, in order to make the system ready for commercialization. Other than the LOS condition, another important aspect is the cost of the proposed system, high at present days. The dimension of devices is also a major concern. The out of focus idea was able to reduce the dimension of the PRA for the same coverage area, which is good, but the dimension of the user device is still a problem. Dimensions, cost, weight, are all reasons for which, before these devices will be ready for commercial roll-out, they need to be implemented in Photonic Integrated Circuit (PIC)s. Once this transition will take place, the only concern left will be the possibility to have a wide angle receiver.

Infrared narrow beams are directed only where user devices are located, so localization is a major aspect in this system. Camera based localization is deeply studied as it proved to be a fast, reliable, cheap and easy to implement form of localization, and it is the main focus of this thesis. The idea behind it

is to equip each user device with infrared LEDs, working for example at the wavelength of 940 nm, around the lens of the receiver. The camera, placed close to the PRA, will detect the presence of these LEDs, invisible to human eye, and when they will be inside the serving area of the PRA itself they will be served by this last one. As discussed in the last chapters, the main problems behind this technique arise from the camera used, that needs to be cheap but fast enough for this purpose. For standing devices, this technique proved to be excellent. For nomadic users, while moving, the connection was dropped a few times, especially corresponding to cell borders. This happened because of a high delay in the communication between the camera and the PC that performs image processing, to determine the position of the user device. A possible solution has been discussed and performed well for all our testings.

Finally, narrow beam free-space transmission is still a young technology, and many aspects need to be addressed before it can be widely used by users. Functional, small form factor, low-cost, and efficient mobile modules are necessary for a practical implementation. This thesis presented a well promising technique for the localization, while considering costs, flexibility and ease of installation, for a future in which Optical Wireless Communication will coexist with radio based communications, to provide ultra high capacities in indoor environment

Bibliography

[1] F. Gomez-Agis, S. P. van de Heide, C. M. Okonkwo, E. Tangdiongga, and A. M. J. Koonen, "112 Gbit/s transmission in a 2D beam steering AWG-based optical wireless communication system", in *Proc. 43rd Eur. Conf. Opt. Commun.*, Gothenburg, Sweden, 2017.

[2] 2019. [Online]. Available: https://www.cisco.com/c/en/us/solutions/internet-of-things/future-of-iot.html

[3] M. Ayyash, H. Elgala, A. Khreishah, V. Jungnickel, T. Little, S. Shao, M. Rahaim, D. Schulz, J. Hilt, and R. Freund, "Coexistence of WiFi and LiFi toward 5G: concepts, opportunities, and challenges", *IEEE Communications Magazine*, vol. 54, no. 2, 2016.

[4] U. D. of Commerce, "United states frequency allocations". Available: https://upload.wikimedia.org/wikipedia/commons/5/5d/United_States_Frequency_Allocations_Chart_2003_-_The_Radio_Spectrum.pdf

[5] L. Yang, "60GHz: opportunity for gigabit WPAN and WLAN convergence", *ACM SIGCOMM Computer Communication Review*, vol. 39, no. 1, 2008.

[6] D. Su, "ISSCC 2013: Wireless trends". Available: http://www.maltiel-consulting.com/ISSCC-2013-Wirelessl-Trends.html

[7] M. Reardon, "Wireless spectrum: What it is, and why you should care", 2012. Available: http://www.cnet.com/news/wireless-spectrum-what-it-is-and-why-you-should-care%20/

[8] T. McCall and M. Mahoney, "Spectrum of issues." Available: http://visual.ly/spectrum-issues

[9] V. Chandrasekhar, J. G. Andrews, and A. Gatherer, "Femtocell networks: a survey", *IEEE Communications Magazine*, vol. 46, no. 9, 2008.

[10] D. Chambers, "What's the difference between picocells and femtocells?" Available: https://www.thinksmallcell.com/FAQs/whats-the-difference-between-picocells-and-femtocells.html

[11] S. Dimatteo, P. Hui, B. Han, and V. O. Li, "Cellular traffic offloading through WiFi networks", in *2011 IEEE Eighth International Conference on Mobile Ad-Hoc and Sensor Systems*. IEEE, 2011

[12] Cisco, "Cisco visual networking index: Global mobile data traffic forecast update, 20152020 white paper", 2016. Available: http://www.cisco.com/c/en/us/solutions/collateral/service-provider/visual-networking-index-vni/mobile-white-paper-c11-520862.html

[13] Aptilo Networks, "Mobile data offloading", 2016. Available: https://www.aptilo.com/mobile-data-offloading/wifi-offload-3g-4g

[14] J. M. Kahn and J. R. Barry, "Wireless infrared communications", in *Proceedings of the IEEE*, vol. 85, no. 2. IEEE, 1997

[15] ANSI, "American national standard for safe use of lasers ANSI z136.1", *American National Standards Institute*, Inc., 2007.

[16] IEC, "International standard IEC 60825-1.2 2001-8", *International Electrotechnical Commission*, Geneva, 2001.

[17] K. Cui, G. Chen, Q. He, and Z. Xu, "Indoor optical wireless communication by ultraviolet and visible light", in *SPIE Optical Engineering+ Applications*. International Society for Optics and Photonics, 2009.

[18] A. G. Bell, "On the production and reproduction of sound by light", *American Journal of Science*, no. 118, 1880.

[19] M. Groth, "Photophones revisted", in *Amateur Radio magazine*. Wireless Institute of Australia, Melbourne, 1987, vol. 55. Available: http://www.bluehaze.com.au/modlight/GrothArticle1.htm

[20] T. H. Maiman, "Stimulated optical radiation in ruby", Nature, no. 187, August 1960.

[21] N. Zheludev, "The life and times of the LED - a 100-year history", *Nature Photonics*, vol. 1, no. 4, 2007.

[22] N. Holonyak Jr and S. Bevacqua, "Coherent (visible) light emission from Ga(As1??xPx) junctions", *Applied Physics Letters*, vol. 1, no. 4, 1962.

[23] D. M. Forin, A. Teixeira, B. Geiger, E. Leitgeb, F. Nadeem, G. Incerti, G. T. Beleffi, L. Costa, and P. D. B. Andre, *Free space optical technologies*. INTECH Open Access Publisher, 2010.

[24] A. K. Majumdar and J. C. Ricklin, *Free-space laser communications: principles and advances*. Springer Science & Business Media, 2010, vol. 2.

[25] S. Das, H. Henniger, B. Epple, C. I. Moore, W. Rabinovich, R. Sova, and D. Young, "Requirements and challenges for tactical free-space lasercomm", in *Military Communications Conference, 2008. MIL-COM 2008*. IEEE. IEEE, 2008.

[26] Y. J. Gawdi et al., "Underwater free space optics", 2006.

[27] M. Toyoshima, "Trends in satellite communications and the role of optical free-space communications [invited]", *Journal of Optical Networking*, vol. 4, no. 6, 2005.

[28] J. C. Juarez, A. Dwivedi, A. R. Hammons, S. D. Jones, V. Weerackody, and R. A. Nichols, "Free-space optical communications for next-generation military networks", *IEEE Communications Magazine*, vol. 44, no. 11, November 2006.

[29] T. Yoshizawa, *Handbook of optical metrology: Principles and Applications*. CRC Press, 2015.

[30] D. C. OBrien, M. Katz, P. Wang, K. Kalliojarvi, S. Arnon, M. Matsumoto, R. Green, and S. Jivkova, "Short-range optical wireless communications", in *Wireless world research forum*, 2005.

[31] D. O'Brien and M. Katz, "Optical wireless communications within fourth-generation wireless systems [invited]", *Journal of optical networking*, vol. 4, no. 6, 2005.

[32] H. Elgala, R. Mesleh, and H. Haas, "Indoor optical wireless communication: potential and state-of-the-art", *IEEE Communications Magazine*, vol. 49, no. 9, 2011.

[33] D. Wisely and I. Neild, "A 100 Mbit/s tracked optical wireless telepoint", in *Personal, Indoor and Mobile Radio Communications, 1997. Waves of the Year 2000. PIMRC'97., The 8th IEEE International Symposium on*, vol. 3. IEEE, 1997.

[34] D. R. Wisely, "A 1 Gbit/s optical wireless tracked architecture for ATM delivery", in *Optical Free Space Communication Links, IEEE Colloquium on*. IET, 1996.

[35] D. C. O'Brien, G. E. Faulkner, K. Jim, E. B. Zyambo, D. J. Edwards, M. Whitehead, P. N. Stavrinou, G. Parry, J. Bellon, M. J. Sibley et al., "High-speed integrated optical wireless transceivers for in-building optical LANs", in *Information Technologies 2000*. International Society for Optics and Photonics, 2001.

[36] V. Jungnickel, A. Forck, T. Haustein, U. Kruger, V. Pohl, and C. Von Helmolt, "Electronic tracking for wireless infrared communications", *IEEE Transactions on Wireless Communications*, vol. 2, no. 5, 2003.

[37] T.-S. Chu and M. Gans, "High speed infrared local wireless communication", *IEEE Communications Magazine*, vol. 25, no. 8, 1987.

[38] A. M. Street, P. N. Stavrinou, D. C. O'Brien, and D. J. Edwards, "Indoor optical wireless systems: a review", *Optical and Quantum Electronics*, vol. 29, no. 3, 1997.

[39] Navigant Consulting Inc., "Energy savings potential of solid state lighting in general illumination applications." Available: http://apps1.eere.energy.gov/buildings/publications/pdfs/ssl/ssl_energy-savings-report_jan-2012.pdf

[40] E. T. Won, D. Shin, D. Jung, Y. Oh, T. Bae, H.-C. Kwon, C. Cho, J. Son, D. O'Brien, T.-G. Kang, and T. Matsumura, "Visible light communication tutorial." Available: http://www.ieee802.org/802_tutorials/2008-03/15-08-0114-02-0000-VLC_Tutorial_MCO_Samsung-VLCC-Oxford_2008-03-17.pdf

[41] H. Le Minh, Z. Ghassemlooy, D. O'Brien, and G. Faulkner, "Indoor gigabit optical wireless communications: challenges and possibilities", in *2010 12th International Conference on Transparent Optical Networks*. National Institute of Telecommunications, June 2010.

[42] Y. Wang, N. Chi, Y. Wang, L. Tao, and J. Shi, "Network architecture of a high-speed visible light communication local area network", *IEEE Photonics Technology Letters*, vol. 27, no. 2, Jan 2015.

[43] PureLiFi^{TM}, "Purelifi", 2016. Available: http://purelifi.com/

[44] H. Haas, L. Yin, Y. Wang, and C. Chen, "What is LiFi?" Journal of Lightwave Technology, vol. 34, no. 6, 2016.

[45] S. Rajagopal, R. D. Roberts, and S.-K. Lim, "IEEE 802.15. 7 visible light communication: modulation schemes and dimming support", *IEEE Communications Magazine*, vol. 50, no. 3, 2012.

[46] A. Sewaiwar, S. V. Tiwari, Y. H. Chung, and C. J. Ahn, "Color cell based bidirectional VLC with user mobility", in *2016 IEEE International Conference on Communications Workshops (ICC)*, May 2016.

[47] J. Voke, "Radiation effects on the eye", *Part 3b-Ocular effects of ultraviolet radiation. Optometry Today*, 1999.

[48] D. J. Heatley, D. R. Wisely, I. Neild, and P. Cochrane, "Optical wireless: the story so far", *IEEE Communications Magazine*, vol. 36, no. 12, 1998.

[49] P. P. Smyth, D. Wood, S. Ritchie, and S. Cassidy, "Optical wireless: New enabling transmitter technologies", in Communications, 1993. ICC '93 Geneva. Technical Program, Conference Record, *IEEE International Conference on*, vol. 1, May 1993.

[50] Cisco, "Fiber types in gigabit optical communications", Cisco Systems, Inc., Tech. Rep. C11-463661-00, 2008.

[51] 2019. [Online]. Available: https://www.ftthcouncil.eu/documents/FTTH%20Council%20Europe%20-%20Panorama%20at%20September%202018.pdf

[52] A. Burger, "Total FTTH subscribers surpass 100 million, one billion subs on the horizon." Available: https://www.benton.org/headlines/report-total-ftth-subscribers-surpass-100-million-one-billion-broadband-nsubs-horizon

[53] K. Schulmeister, R. Gilber, F. Edthofer, B. Seiser, and G. Vees, "Comparison of different beam diameter definitions to characterize thermal damage of the eye", in *Lasers and Applications in Science and Engineering. International Society for Optics and Photonics*, 2006.

[54] Wikipedia, "Laser safety", 2016. Available: https://en.wikipedia.org/wiki/Laser safety

[55] P. F. McManamon, T. A. Dorschner, D. L. Corkum, L. J. Friedman, D. S. Hobbs, M. Holz, S. Liberman, H. Q. Nguyen, D. P. Resler, R. C. Sharp et al., "Optical phased array technology", *Proceedings of the IEEE*, vol. 84, no. 2, 1996.

[56] J. D. Zook, "Light beam deflector performance: a comparative analysis", *Applied Optics*, vol. 13, no. 4, 1974.

[57] D. J. Pines, D. B. Hakala, and R. Malueg, "Lightweight high performance dual-axis gimbal for space applications", in SPIE's 1995 Symposium on OE/Aerospace Sensing and Dual Use Photonics. International Society for Optics and Photonics, 1995.

[58] T. G. Sandwich and D. Backup, "Lightweight mirror structures for mechanical beam steering", Lincoln Laboratory Journal, vol. 1, no. 2, 1988.

[59] L. Zhou, J. M. Kahn, and K. S. Pister, "Scanning micromirrors fabricated by an SOI/SOI wafer-bonding process", Journal of Microelectromechanical Systems, vol. 15, no. 1, 2006.

[60] J. Sun, S. Guo, L. Wu, L. Liu, S.-W. Choe, B. S. Sorg, and H. Xie, "3D in vivo optical coherence tomography based on a low-voltage, large-scan-range 2D MEMS mirror", Optics Express, vol. 18, no. 12, 2010.

[61] D. M. Burns, V. M. Bright, S. C. Gustafson, and E. A. Watson, "Optical beam steering using surface micromachined gratings and optical phased arrays", in *Optical Science, Engineering and Instrumentation'97*. International Society for Optics and Photonics, 1997.

[62] R. M. Matic, "Blazed phase liquid crystal beam steering", in *OE/LASE'94. International Society for Optics and Photonics*, 1994.

[63] S. Khan and N. Riza, "Demonstration of 3-dimensional wide angle laser beam scanner using liquid crystals", *Optics Express*, vol. 12, no. 5, 2004.

[64] J. Sun, R. A. Ramsey, Y. Chen, and S.-T. Wu, "Submillisecond response sheared polymer network liquid crystals for display applications", *Journal of Display Technology*, vol. 8, no. 2, 2012.

[65] K. Nakamura, J. Miyazu, Y. Sasaki, T. Imai, M. Sasaura, and K. Fujiura, "Space-charge-controlled electro-optic effect: Optical beam deflection by electro-optic effect and space-charge-controlled electrical conduction", *Journal of Applied Physics*, vol. 104, no. 1, 2008.

[66] T. Smith and A. Korpel, "Measurement of light-sound interaction efficiencies in solids", *IEEE Journal of Quantum Electronics*, vol. 1, no. 6, 1965.

[67] E. Spencer, P. Lenzo, and K. Nassau, "Optical interactions with elastic waves in lithium niobate", IEEE Journal of Quantum Electronics, vol. 2, no. 3, 1966.

[68] E. Gordon, "A review of acoustooptical deflection and modulation devices", Applied Optics, vol. 5, no. 10, pp. 1966.

[69] I. Chang, "Acoustooptic devices and applications", IEEE Transactions on Sonics and Ultrasonics, vol. 23, no. 1, 1976.

[70] F. Mugele and J.-C. Baret, "Electrowetting: from basics to applications", *Journal of Physics: Condensed Matter*, vol. 17, no. 28, 2005.

[71] N. R. Smith, D. C. Abeysinghe, J. W. Haus, and J. Heikenfeld, "Agile wide-angle beam steering with electrowetting microprisms", *Optics Express*, vol. 14, no. 14, 2006.

[72] L. Enloe, J. Murphy, and C. Rubinstein, "Hologram transmission via television", *Bell System Technical Journal*, vol. 45, no. 2, 1966.

[73] D. Gabor, "Holography, 1948-1971", *Proceedings of the IEEE*, vol. 60, no. 6, June 1972.

[74] J. P. Huignard, A.-M. Roy, and C. Slezak, "Electro-optical deflection apparatus using holographic grating", Sep. 1976.

[75] M. K. Smit and C. Van Dam, "Phasar-based wdm-devices: Principles, design and applications", *IEEE Journal of selected topics in quantum electronics*, vol. 2, no. 2, 1996.

[76] X. J. Leijtens, B. Kuhlow, and M. K. Smit, "Arrayed waveguide gratings", in *Wavelength Filters in Fibre Optics*. Springer, 2006.

[77] S. O. Kasap, *Optoelectronics & Photonics: Principles & Practices: International Edition*. Pearson Higher Ed, 2001.

[78] M. K. Giles, R. Hughes, and J. Thompson, "Angular dispersion of diffraction gratings used for tuning organic dye lasers", *Applied Optics*, vol. 12, no. 2, 1973.

[79] A. Balakrishnan, S. Bidnyk, and M. Pearson, "Double diffraction grating with at passband output", US Patent 7,149,387, Dec., 2006.

[80] C. A. Palmer and E. G. Loewen, Diffraction grating handbook. Newport Corporation Springfield, Ohio, USA, 2005.

[81] M. Born and E. Wolf, *Principles of optics: electromagnetic theory of propagation, interference and diffraction of light*. CUP Archive, 2000.

[82] M. Shirasaki, "Large angular dispersion by a virtually imaged phased array and its application to a wavelength demultiplexer", *Optics Letters*, vol. 21, no. 5, 1996.

[83] M. Shirasaki, "Virtually imaged phased array", *Fujitsu Scientific & Technical Journal*, vol. 35, no. 1, 1999.

[84] T. Koonen, J. Oh, K. Mekonnen, Z. Cao, and E. Tangdiongga, "Ultra-high capacity indoor optical wireless communication using 2D-steered pencil beams", *Journal of Lightwave Technology*, vol. 34, no. 20, Oct 2016.

[85] A. M. J. Koonen, C. W. Oh, and E. Tangdiongga, "Reconfigurable free-space optical indoor network using multiple pencil beam steering", in *19th Optoelectronics and Communications Conference (OECC) and the*

39th Australian Conference on Optical Fibre Technology (ACOFT). Engineers Australia, 2014.

[86] A. M. J. Koonen, P. G. Baltus, and A. Liotta, "Two-dimensional optical beam steering module", US Patent 9,246,589, Jan., 2016, US Patent 9,246,589.

[87] A. M. J. Koonen, J. Oh, K. Mekonnen, and E. Tangdiongga, "Ultra-high capacity indoor optical wireless communication using steered pencil beams", in *Microwave Photonics (MWP), 2015 International Topical Meeting on*. IEEE, 2015.

[88] T. Koonen, J. Oh, A. Khalid, K. Mekonnen, M. T. Vega, Z. Cao, and E. Tangdiongga, "2D beam-steered high-capacity optical wireless communication", in *Photonics Society Summer Topical Meeting Series (SUM), 2016 IEEE*. IEEE, 2016.

[89] T. Koonen, J. Oh, K. Mekonnen, Z. Cao, and E. Tangdiongga, "Ultra-high capacity indoor optical wireless communication using 2D-steered pencil beams", *Journal of Lightwave Technology*, vol. 34, no. 20, Oct 2016.

[90] C. W. Oh, "Free-Space Transmission with Passive Two-Dimensional Beam Steering for Indoor Optical Wireless Networks", 2017.

[91] J. Lee, "Discrete multitone modulation for short-range optical communications", Ph.D. thesis, Eindhoven University of Technology, 2009.

[92] K. D. Langer, Visible Light Communication. Cambridge: Cambridge University Press. Cambridge Books Online, February 2015, ch. DMT modulation for VLC.

[93] H. Kogelnik and T. Li, "Laser beams and resonators", *Applied Optics*, vol. 5, no. 10, 1966.

[94] J. Alda, "Laser and gaussian beam propagation and transformation", *Encyclopedia of Optical Engineering*, vol. 2013, 2003.

[95] A. Ryer and V. Light, "Light measurement handbook", 1997.

[96] K. T. McDonald, "Intensity, brightness andetendue of an aperture lamp", 2013.

[97] H. Zhu and P. Blackborow, "Etendue and optical throughput calculations", 2011. Available: http://www.energetiq.com/TechLibrary/Technical_Notes/Etendue%20and%20Optical%20Throughput%20Calculations%20-%20Feb%202011.pdf

[98] R. Baets and G. Roelkens, "Fotonica Photonics", Universiteit Gent, (syllabus 2010-2011), 2015.

[99] A. Nicia, "Lens coupling in fiber-optic devices: efficiency limits", Applied optics, vol. 20, no. 18, 1981.

[100] Thorlabs, "Single mode fiber 980 to 1600 nm", 2017. Available: https://www.thorlabs.com/newgrouppage9.cfm?objectgroup_id=949

[101] Thorlabs, "Graded-index multimode fibers", 2017. Available: https://www.thorlabs.com/newgrouppage9.cfm?objectgroup_id=358

[102] Thorlabs, "Step-index multimode fiber, 0.50 na", 2017. Available: https://www.thorlabs.com/newgrouppage9.cfm?objectgroup_id=362

[103] New Focus, "12-GHz amplified free-space photoreceivers." Available: http://assets.newport.com/webDocuments-EN/images/15173.PDF

[104] G. Keiser, *Optical fiber communications*. Wiley Online Library, 2000.

[105] J. Carruther and J. M. Kahn, "Angle diversity for nondirected wireless infrared communication", *IEEE Transactions on Communications*, vol. 48, no. 6, 2000.

[106] G. W. Marsh and J. M. Kahn, "50-Mb/s diffuse infrared free-space link using on-off keying with decision-feedback equalization", *IEEE Photonics Technology Letters*, vol. 6, no. 10, 1994.

[107] J. R. Barry and J. M. Kahn, "Link design for nondirected wireless infrared communications", *Applied Optics*, vol. 34, no. 19, 1995.

[108] D. V. Hahn, D. M. Brown, N. W. Rolander, J. E. Sluz, and R. Venkat, "Fiber optic bundle array wide field-of-view optical receiver for free space optical communications", *Optics Letters*, vol. 35, no. 21, 2010.

[109] K. Wang, A. Nirmalathas, C. Lim, and E. Skafidas, "High-speed duplex optical wireless communication system for indoor personal area networks", *Optics Express*, vol. 18, no. 24, 2010.

[110] A. Gomez, K. Shi, C. Quintana, M. Sato, G. Faulkner, B. C. Thomsen, and D. O'Brien, "Beyond 100-Gb/s indoor wide field-of-view optical wireless communications", *IEEE Photonics Technology Letters*, vol. 27, no. 4, 2015.

[111] C. W. Oh, F. M. Huijskens, Z. Cao, E. Tangdiongga, and A. M. J. Koonen, "Toward multi-Gbps indoor optical wireless multicasting system employing passive diffractive optics", *Optics Letters*, vol. 39, no. 9, 2014.

[112] C. W. Oh, E. Tangdiongga, and A. M. J. Koonen, "Steerable pencil beams for multi-Gbps indoor optical wireless communication", *Optics Letters*, vol. 39, no. 18, 2014.

[113] Thorlabs, "Triplet fiber optic collimators/couplers." Available: https://www.thorlabs.de/newgrouppage9.cfm?objectgroup_id=5124 &pn=TC18FC-1550#7057

[114] C. W. Oh, Z. Cao, E. Tangdiongga, and A. M. J. Koonen, "Free-space transmission with passive 2D beam steering for multi-gigabit-persecond per-beam indoor optical wireless networks", *Optics Express*, vol. 24, no. 17, 2016.

[115] Y.-L. Yu, S.-K. Liaw, E. Skaljo, H. L. Minh, and Z. Ghassemlooy, "Bidirectional wavelength reconfigurable module based on tunable fiber bragg grating and remote pump amplifier", *Fiber and Integrated Optics*, vol. 33, no. 5-6, 2014.

[116] A. M. Khalid, A. M. J. Koonen, C. W. Oh, Z. Cao, K. A. Mekonnen, and E. Tangdiongga, "10 Gbps indoor optical wireless communication employing 2D passive beam steering based on arrayed waveguide gratings", in *Photonics Society Summer Topical Meeting Series (SUM)*, 2016 IEEE. IEEE, 2016.

[117] T. Koonen, J. Oh, A. Khalid, K. A. Mekonnen, M. T. Vega, Z. Cao, and E. Tangdiongga, "2D beam-steered high-capacity optical wireless

communication", in *IEEE Photonics Society Summer Topical Meeting Series (SUM)*,26-30 September, NewPort Beach, California, USA, 2016, paper TuC2.2.

[118] A. M. J. Koonen, F. Gomez-Agis, F. Huijskens, K. A. Mekonnen, Z. Cao, and E. Tangdiongga, "High-Capacity Optical Wireless Communication Using Two-Dimensional IR Beam Steering", *IEEE/OSA J. Lightw. Technol.*, vol. 36, no. 19, Oct. 2018.

[119] A. M. Khalid et al., "10 Gbps indoor optical wireless communication employing 2D passive beam steering based on arrayed waveguide gratings", in *Proc. IEEE Photon. Soc. Summer TopicalMeet. Series*, Newport Beach, CA, USA, Jul. 2016, Paper TuC2.3.

[120] A. M. J. Koonen et al., "High-capacity optical wireless communication using AWGrouter for 2-dimensional IR beam steering", in *Proc. Int. Conf. OptoElectron. Commun.*, Singapore, Jul./Aug. 2017, Paper 1-4K-3.

[121] A. M. Khalid et al., "Bi-directional 35-Gbit/s 2D beam steered optical wireless downlink and 5-Gbit/s localized 60-GHz communication uplink for hybrid indoor wireless systems", in *Proc. Int. Conf. Opt. Fiber Commun.*, Los Angeles, CA, USA, Mar. 2017, Paper Th1E.6.

[122] A. Yassin et al., "Recent advances in indoor localization: A survey on theoretical approaches and applications", *IEEE Commun. Surv. Tutor.*, vol. 19, no. 2, 2016.

[123] Y. Zhuang et al., "A survey of positioning systems using visible LED lights", *IEEE Commun. Surv. Tutor.*, vol. 20, no. 3, 2018.

[124] A. Gomez, K. Shi, C. Quintana, G. Faulkner, B. C. Thomsen, and D. O'Brien, "A 50 Gb/s transparent indoor optical wireless communications link with an integrated localization and tracking system", *J. Light. Technol.*, vol. 34, no. 10, 2016.

[125] N. Q. Pham, K. A. Mekonnen, E. Tangdiongga, A. Mefleh, and A. M. J. Koonen, "Accurate Indoor Localization for Beam-Steered OWC System Using Optical Camera", in *Proc. 45th Eur. Conf. Opt. Commun.*, Dublin, Ireland, 2019.

Acknowledgements

I would like to take this opportunity to thank everyone who accompanied me through this journey. I'm not talking only about this master thesis, because to me, this paper is way more than that, it sets the end of the student life that I had so far. I don't know if I will start a new degree in the university, but I know that the feeling of being a student will not be the same.

I never thought I would say that, because I do not have a past of a perfect student, especially from high school, but I want to thank the university, for five years rich of emotions, from classes, exams, to the two final graduations. Thanks to the university I had the great chance to study and live abroad, three times, during my three astonishingly beautiful Erasmus. I had never imagined I would feel so connected to people so different from me, coming from different cultures. This is now, by far, the experience that make me feel European the most. I learned to be open minded as I never thought possible. It's been a privilege to be a part of the Erasmus program.

My sincere gratitudes to my Supervisor Prof. Tartarini, for giving me the opportunity of making this thesis abroad in Eindhoven and for being always available and nice to me. The nicest thing is to come back to Italy and talk to my supervisor as much about practical aspects of my thesis as personal aspects of this great experience abroad. I need to thank my co-supervisor in the TU/e as well, for showing me the details of my work and for making this exchange possible.

My heartfelt greetings to my friends from the ninth floor, in the Flux building of the TU/e, for bringing laughs and happiness to a study environment, and for the long coffee breaks. Thanks to Mercedes, for the coffees you offered me in every break, and for the times we talked, it's been a pleasure to meet you and help you in any way I could. In the end, I'm the linux guy for a reason.

Deepest thanks to Quan, not only for being a great PhD student that showed me the passion behind his work, but for the great time spent talking, in the eighth floor, looking at the flatness of The Netherlands outside the glass wall. I can't thank you enough for all the coffees you offered me. I will never forget your almost-one-year-old son trying to talk during my final presentation.

I can't say enough beautiful things to the company I met in this last Erasmus. They have been close friends in every moment and made this exchange a magic experience. Our Dinners group was the best invention we could make. When this Erasmus was over, it broke my heart to let you all go. Eindhoven felt empty without you. I have some breathtaking memories like Simon going away from Gemini and Isma biking away in our last night, and many more, that I'm happy nobody will ever take from me. It's been a pleasure to meet you all, I wish you only the best.

Among them, there is also one person that is coming to visit me for my graduation and whom I hope to see many more times in the future, who made me feel home since the first days of being abroad, who biked and walked a lot with me and with whom I traveled in many places in The Netherlands. Thank you Anne.

I want to thank my host family, for helping me in the hard task of finding a place to stay in Eindhoven, but way more than that, for being a great and happy family. I was not expecting to get so attached to you. The sound of the piano from the ground floor, the dinners we had together, the trip to Vlieland, the life your house gets when your family and friends are there. I deeply appreciated your generous hospitality.

Finally, I'm glad to thank my family, that is about to get bigger, for the love and support throughout my whole life.